



HAL
open science

Scintillation properties of II-VI semiconductor nanocrystal heterostructures

Zhu Meng

► **To cite this version:**

Zhu Meng. Scintillation properties of II-VI semiconductor nanocrystal heterostructures. Physics [physics]. Université de Lyon, 2021. English. NNT : 2021LYSE1093 . tel-03647605

HAL Id: tel-03647605

<https://theses.hal.science/tel-03647605>

Submitted on 20 Apr 2022

HAL is a multi-disciplinary open access archive for the deposit and dissemination of scientific research documents, whether they are published or not. The documents may come from teaching and research institutions in France or abroad, or from public or private research centers.

L'archive ouverte pluridisciplinaire **HAL**, est destinée au dépôt et à la diffusion de documents scientifiques de niveau recherche, publiés ou non, émanant des établissements d'enseignement et de recherche français ou étrangers, des laboratoires publics ou privés.



N°d'ordre NNT : 2021LYSE1093

THESE de DOCTORAT DE L'UNIVERSITE DE LYON

opérée au sein de
l'Université Claude Bernard Lyon 1

Ecole Doctorale N° ED52
Physique et Astrophysique de Lyon (PHAST)

Spécialité de doctorat :
Discipline : Physique

Soutenue publiquement le 28/05/2021, par :
Zhu MENG

Propriétés de scintillation d'hétérostructures nanocristaux semiconductrices II-VI

Devant le jury composé de :

Franck LEPINE
Audrey POTDEVIN
Martin NIKL
Frédéric LEROUGE
Anna VEDDA
Christophe DUJARDIN
Benoit MAHLER
Sandrine ITHURRIA

Directeur de Recherche, Univ Lyon 1
Maître de Conférences, Univ Clermont - Auvergne
Chercheur, Institute of Physics, Academy of Sciences
Maître de Conférences, ENS Lyon
Professeure, Univ Milan
Professeur, Univ Lyon 1
Chargé de recherches, CNRS
Maître de Conférences, ESPCI

Président
Rapporteure
Rapporteur
Examinateur
Examinatrice
Directeur de thèse
Co-directeur de thèse
Invitée

Contents

Contents	1
List of figures	5
List of tables	12
List of abbreviations	13
Chapter 1	15
Introduction	15
1.1 Aim of the thesis	16
1.2 Organization of the thesis	17
Chapter 2	19
Scientific background	19
2.1 Colloid semiconductor nanocrystals	19
2.1.1 Quantum confinement effect.....	19
2.1.2 Surface effect.....	22
2.2 Heterostructural nanocrystals	23
2.3 Excited state dynamics under photoexcitation	25
2.3.1 Hot carriers relaxation	26
2.3.2 Exciton recombination.....	27
2.3.3 Auger recombination	28
2.3.4 Multiexcitons recombination.....	29
2.3.4.1 Biexciton	30
2.3.4.2 Triexciton	31
2.3.4.3 Carrier multiplication	33
2.4 Scintillation process and scintillator	34
2.4.1 Scintillation process	34
2.4.2 Nanocrystals scintillator	38
2.5 Spherical quantum wells and nanoplatelets	41
2.5.1 Spherical quantum wells introduction.....	41
2.5.2 Nanoplatelets introduction	43

Chapter 3	47
Colloidal Synthesis and Characterization of Spherical Quantum Wells and Nanoplatelets.....	47
3.1 Synthesis theory and setup	47
3.1.1 Nanocrystals nucleation and growth	47
3.1.1.1 Gibbs -Thompson theory	47
3.1.1.2 Lamer burst nucleation theory.....	49
3.1.1.3 Nanocrystals synthesis setup and method	50
3.1.2 Core/shell structure synthesis	51
3.2 Optical and structural characterization techniques	51
3.2.1 Absorption spectrum.....	52
3.2.2 Photoluminescence spectrum	52
3.2.3 Photoluminescence excitation spectrum	53
3.2.4 Quantum yield measurement.....	54
3.2.5 Transmission electron microscopy	56
3.3 Spherical quantum wells synthesis and characterization.....	56
3.3.1 Synthesis	57
3.3.1.1 Chemical materials	57
3.3.1.2 Preparation of precursors	57
3.3.1.3 Synthesis protocol	58
3.3.2 Characterization	60
3.3.2.1 Absorption and photoluminescence spectra	61
3.3.2.2 Photoluminescence excitation spectroscopy	64
3.3.2.3 Structural characterization	65
3.4 Colloidal Synthesis and Characterization of Heterostructural Nanoplatelets	66
3.4.1 Chemical materials	66
3.4.2 CdSe nanoplatelets	66
3.4.3 Core/crown CdSe/CdS.....	68
3.4.4 Hot-injection alloyed core/shell CdSe/CdZnS.....	71
3.4.5 Hot-injection core/crown/shell CdSe/CdS/CdZnS	74
3.5 Conclusion	76
Chapter 4	79
Scintillation properties of spherical quantum wells under X-rays excitation.....	79
4.1 Experimental setups.....	79
4.1.1 Radioluminescence setup.....	79

4.1.2 Time-resolved measurements	80
4.1.2.1 Decay curve measurement	80
4.1.2.2 Time-resolved emission spectrum	82
4.2 Possible mechanism in nanocrystals and simulation	83
4.2.1 Possible scintillation process in nanocrystals	83
4.2.2 Simulation the scintillation process in nanocrystals	84
4.3 Steady state radioluminescence	87
4.4 Photoexcitation	89
4.4.1 Photoluminescence decay curve measurement	89
4.4.2 Time-resolved photoluminescence spectrum	95
4.5 X-rays excitation	99
4.5.1 Time-resolved radioluminescence spectrum	100
4.5.2 Radioluminescence decay curve measurement	102
4.6 Conclusion	105
Chapter 5	107
Scintillation properties of hererostructural II-VI nanoplatelets under X-rays excitation	107
5.1 Sample preparation and stability	107
5.2 Core/crown CdSe/CdS nanoplatelets	109
5.2.1 Steady state radioluminescence	109
5.2.2 Time-resolved measurements	111
5.3 Core/shell CdSe/CdZnS nanoplatelets	113
5.3.1 Steady state radioluminescence	113
5.3.2 Time-resolved measurements	115
5.4 Core/crown/shell CdSe/CdS/CdZnS nanoplatelets	123
5.4.1 Steady state radioluminescence	123
5.3.2 Time-resolved measurements	125
5.5 Conclusion	129
Chapter 6	131
Conclusion	131
Annexe1: Estimation of absorption cross section of spherical quantum wells	135
Annexe2: Solution sample under optical parametric oscillation laser	137
A2.1 Spherical quantum wells solution sample	137
A2.2 Heterostructural nanoplatelets solution sample	138
A2.2.1 Core/crown CdSe/CdS	138

A2.2.2 Core/shell CdSe/CdZnS 139

Annexe3: The influence of the applied voltage on PL spectra in nanoplatelets141

References.....143

List of figures

- Figure 2.1 Schematic representation of quantum confinement effect: a bulk semiconductor with continue energy band and a fixed energy gap $E_{g,bulk}$, while NCs possess discrete energy levels and the band gap energy increases with decreasing size. . 20
- Figure 2.2 (a) Theoretical calculation on size dependence of the electron and hole energy levels in a CdSe quantum dots(QDs). (b) The comparison between theoretical and experimental data for several of the lowest transitions. 21
- Figure 2.3 Schematic diagram of the density of states as a function of dimensionality. Bulk materials(3D) without quantum confinement effects in three dimensions; 2D refers to quantum wells with quantum confinement effects in only one dimension;1D refers to rod-shaped or wire-shaped nanocrystals restricted in two dimensions; 0D mainly refers to quantum dots confined in three dimensions. 22
- Figure 2.4 Schematic representation of the energy level alignment and charge carrier localization in type I, quasi-type II and type II core/shell hetero-structural NCs, respectively. 25
- Figure 2.5 Schematic representation of possible relaxation and recombination processes in NCs after photoexcitation. (1) exciton is generated by absorption of a photon with energy $\hbar\omega \geq E_g$ or more photons are absorbed to form a multiexcitons state. (2)The hot exciton may relax to band edge by cooling process. (3)If $\hbar\omega \geq 2E_g$, two or more excitons can be created through carrier multiplication(or multiple exciton generation, MEG) . (4)Multiexcitons will recombine radiatively to emit photon or non-radiatively via Auger recombination. (5) Eventually, the exciton recombines, relaxing the NCs back to the ground state. 26
- Figure 2.6 Schemes showing the difference between Auger recombination process in direct gap bulk (left) and NCs (right) semiconductors. ΔE and Δp present the change of energy and momentum, respectively. E_c and E_v are the edge of conduction and valence bands. Compared to bulk material, the requirement of momentum conservation is largely relaxed in NCs and Auger recombination occurs efficiently for band edge carriers. 29
- Figure 2.7 Schematic diagram of the exciton and exciton Coulomb interaction in nanocrystals: (a) attractive force, (b) repulsive force. 31
- Figure 2.8 Schematic diagram of the different radiative recombination pathways for triexciton in CdSe quantum dots. (a) The triexciton can decay by S-S electron-hole recombination, leading to an excited biexciton, following by the thermal process, (b) or by P-P recombination, leading to a ground-state biexciton, (c) or via the nominally

forbidden $1P_e-1S_h$, also followed by a thermal process. Finally, each of these three pathways can bring the system to the ground-state biexciton.	32
Figure 2.9 Schematic diagram of the carrier multiplication process. (a) Absorbing a photon with energy $<2E_g$, the electron dissipate the energy as heat. (b) After the absorption of a single high-energy photon ($>2E_g$), two excitons can be created through the Coulomb interaction in carrier multiplication process.	33
Figure 2.10 Schematic representation of X-rays tube	34
Figure 2.11 A simplified schematic representation of scintillation detector.	35
Figure 2.12 Schematic representation of scintillation mechanism in bulk inorganic scintillators. High energy photons absorbed can generate hot charge carriers, followed by thermalization to form a great amount of excitons and subsequent transport to traps involved intermediate states or luminescence centers, where radiative recombination occurs.....	38
Figure 2.13 (a) Schematic illustration of spherical quantum wells; (b) Quasi type II energy band alignment of spherical quantum wells.....	42
Figure 2.14 (a) Absorption and photoluminescence spectra of different shell thickness SQWs (r: CdS core; l: CdSe well; h: CdS shell), (b) The evolution of ensemble PL decay dynamics with shell thickness (inset: single-exciton radiative recombination lifetime; R is the total size).	42
Figure 2.15 Absorption and photoluminescence spectra of CdSe colloidal NPLs with different vertical thicknesses.	44
Figure 2.16 (a) Schematic illustration of core/crown, core/shell and core/crown/shell heterostructures. (b) Absorption and photoluminescence spectra of CdSe/CdS core/crown, CdSe/CdZnS core/shell and CdSe/CdS/CdZnS core/crown/shell NPLs, all of which are synthesized at our laboratories.	46
Figure 3.1 Red curve is the total Gibbs free energy as a function of the nuclei radius. ΔG_c is the homogeneous nucleation energy barrier, and r_c is the critical radius. The bulk term ΔG_1 that scales with r^3 is plotted in green. The interfacial energy ΔG_2 is the blue curve that is proportional to surface area.....	48
Figure 3.2 Schematic illustration of the nucleation and subsequent growth process.	49
Figure 3.3 Schematic of three neck flask apparatus for nanocrystals synthesis.	50
Figure 3.4 Evolution of the absorption spectra with increasing size of CdS/CdSe quantum dots, which are synthesized in our laboratory.	52
Figure 3.5 Evolution of the photoluminescence spectrum with increasing size of CdS/CdSe quantum dots, which are synthesized in our laboratory.	53
Figure 3.6 Comparison between ABS and PLE spectra. (a) without secondary nucleation and (b) with secondary nucleation. (c) taken at different emission wavelengths (the	

maximum of the emission, lower energy side and the higher energy side of the emission peak).	54
Figure 3.7 Schematic representation of absolute method with integrating sphere. Left: substrate spectrum measurement, right: sample spectrum measurement.	55
Figure 3.8 TEM images of nanoparticles at different magnifications: A.20000X, B.120000X, C.300000X.	56
Figure 3.9. The protocol of spherical quantum wells synthesis	58
Figure 3.10 Absorption spectra of CdS seeds in hexane	61
Figure 3.11 (a)Absorption spectrum of CdS/CdSe in hexane: variety color curves represent different aliquots taken during size growing, showing a red shift; (b)TEM image of CdS/CdSe at 400000X magnification, inset is the histogram of size distribution of ~100 particles.	62
Figure 3.12 Absorption(left) and photoluminescence(right) spectra of CdS/CdSe and different sized spherical quantum wells: 15nm, 20nm, 25nm 30nm, 35nm, 40nm.	63
Figure 3.13 Image of different size SQWs from 15nm to 40nm dispersed in hexane with the same concentration under white light and UV light excitation.	63
Figure 3.14 Comparison between ABS and PLE spectra. (a) CdS/CdSe and the same sample with additional ligands; (b) spherical quantum wells(30nm in diameter).	64
Figure 3.15 Transmission electron microscopy (TEM) images of different size SQWs at magnification 30000X, insets are histograms of size distribution.	65
Figure 3.16 Absorption and normalized photoluminescence spectra of 4ML nanoplatelets. The excitation photon wavelength is 350nm.	67
Figure 3.17 TEM images of 4ML CdSe NPLs.	68
Figure 3.18 (a)Absorption spectra of CdSe/CdS core/crown NPLs with the crown increasing, (b) photoluminescence spectra of C/C NPLs synthesized by three methods with different crown size, comparing with core 4ML NPLs.	70
Figure 3.19 TEM images of core/crown NPLs synthesized by three different approaches, (a) anisotropic growth solution, (b) S-ODE, (c) TOPS. (d) PLE of core/crown NPLs(approach 3) at different emission wavelengths (as shown in inset).	71
Figure 3.20 Absorption and photoluminescence spectra evolution of three core/shell CdSe/CdZnS NPLs with the increasing shell thickness.	72
Figure 3.21 Photoluminescence excitation spectra of core/shell CdSe/CdZnS NPLs with different thickness shell measured at different emission wavelengths.	73
Figure 3.22 TEM images of different thickness core/shell CdSe/CdZnS NPLs. (a) and (b) are core/shell_s, the arrow shows the vertical thickness is around 3.5nm, (c) and (d) are core/shell_m and core/shell_l, respectively.	74

Figure 3.23 (a)Absorption and photoluminescence spectra comparison of core/shell (black dash line) and core/crown/shell NPLs (red solid line). (b)PLE of C/C/S NPLs with different thickness shell measured at different emission wave lengths.	75
Figure 3.24 TEM image of core/crown/shell CdSe/CdS/CdZnS NPLs.....	76
Figure 4.1 Schematic representation of radioluminescence and photoluminescence setup.	80
Figure 4.2 Schematic representation of photoluminescence decay curve measurement setup.....	81
Figure 4.3 Schematic representation of time resolved emission spectrum setup under X-rays excitation	82
Figure 4.4 Schematic representation of the multiexcitons formation process in nanocrystals (a) Absorbing three low energy photons simultaneously by intense pulsed excitation, (b) Simplified energy relaxation process by X-rays excitation (only three electron and hole pairs are shown).	84
Figure 4.5 Schematic energy band diagram and density of state function of the SQWs. .	84
Figure 4.6 (a)Energy loss function restricted to 0-25 eV for CdS and CdSe. (b)Distribution of the number of scatterings for a 30keV primary electron for various particle sizes.	85
Figure 4.7 Simulation of evolution of excitations in NCs. (a) calculated time evolution of the population of neutral excitations (1, 2, 3 ... electron-hole pairs) for a 25nm SQWs considering an initial situation with a single secondary electron hole pair. Dashed curves corresponds to the simulation without considering radiative recombination. (b) and (c) Same simulation with initial situation with 2, 3 secondary electron hole pairs. For the simulation, radiative recombination considers a radiative decay time: $\tau_X=50\text{ns}$, $\tau_{BX}=12.5\text{ns}$, $\tau_{TX}=5.6\text{ns}$. Excitation source: 20keV photons.	86
Figure 4.8 Photoluminescence spectra comparison of solution samples (black line) and film samples (blue line).	87
Figure 4.9 Steady-state PL and RL spectra of a series of drop-cast SQWs (15nm, 25nm, 30nm, 40nm). Excitation source: 405nm light emitting diode(black line) and X-rays illumination at a voltage of 35 kV (red line).	88
Figure 4.10 Emission intensity evolution with different X-rays illumination time of 15nm and 40nm SQWs. The X-ray images were recorded at a voltage of 35 kV. The accumulation time is 400s.	89
Figure 4.11 (a) PL decays of ensemble CdS/CdSe/CdS SQWs with varying shell thicknesses under low intensity excitation without focusing and wavelength filter. (b) Single exciton recombination lifetime for varying sized SQWs.	90
Figure 4.12 Decay dynamics measured at three different energy position of a drop-cast 15nm diameter SQWs. (a) $\langle N \rangle \sim 0.003$, (b) $\langle N \rangle \sim 4$. Black curve in (b) is the instrument response function (IRF).	91

- Figure 4.13 The PL decay curves of 15nm diameter SQWs under various excitation powers are normalized at 60ns to match the single exciton tail, highlighting the fast multiexcitons component at early time. 92
- Figure 4.14 (a) Multiexcitons dynamics in 15nm SQWs obtained by subtracting the scaled single exciton contribution from high power decay ($\langle N \rangle \sim 4$), it can be fitted with two exponentials by 0.72ns and 3.14ns. (b) Power dependent integral PL intensity of fast component (red square) and slow component (purple square). Slow component shows a single exciton signature and the fast component follows an approximately quadratic dependence on power. 93
- Figure 4.15 The PL decay curves of 25nm(a) and 40nm(b) diameter SQWs under various excitation powers are normalized at 100ns and 250ns to match the single exciton tail, compared to that of 15nm SQWs, the multiexcitons components are longer lived. 94
- Figure 4.16 Comparison of time gated spectra corresponding to different time intervals of 15nm SQWs. (a) 9.3nW, (b) 35.78 μ W. 96
- Figure 4.17 (a) Normalized time-resolved PL spectra in first 800ps as a function of power for drop-cast 15nm SQWs. The excitation wavelength is 405nm. (b) Absorption (red), and absorption second derivative (black) spectra of 15nm SQWs. The arrows mark the $1S_e-1S_h \rightarrow 1.96\text{eV}$ and $1P_e-1P_h \rightarrow 2.16\text{eV}$ transitions. 97
- Figure 4.18 (a, c) Comparison of spectra corresponding to different time intervals of 25nm and 40nm SQWs at power 35.78 μ W. (b) The energy shift of different peak with respect to single exciton peak for 15nm, 25nm and 40nm SQWs. (d) Delayed emission at the late time of 40nm SQWs. 98
- Figure 4.19 Integrated total photons under low (black line) and high (red line) power excitation of 15nm, 25nm and 40nm SQWs. 99
- Figure 4.20 Decay dynamics measured at different energy of 15nm sample. Excitation source: X-rays illumination at a voltage of 30 kV. 100
- Figure 4.21 Comparison of time gated spectra corresponding to different time intervals of 15nm, 25nm and 40nm SQWs under X-rays excitation. Excitation source: X-rays illumination at a voltage of 30 kV. 101
- Figure 4.22 Comparison of time gated spectra at 0-2ns interval for 15nm, 25nm and 40nm SQWs under X-rays excitation with high intense photoexcitation. Excitation source: X-rays illumination at a voltage of 30 kV and the laser power is 35.78 μ W. 102
- Figure 4.23 Comparison of the decay dynamics under X-rays and photoexcitation of 15nm, 25nm and 40nm SQWs (defocusing). Red curves are the multiexponential fitting. 103
- Figure 5.1 Comparison of the optical properties between core/shell NPLs film (black line) and core/shell NPLs in polymer film (red line). (a) PL spectra recorded under low intensity optical excitation. (b) PL decay curves of the peak wavelength excited by low intensity pulsed laser to avoid the formation of multiexcitons. 108

Figure 5.2 Radioluminescence spectra of C/S NPLs for different illuminated time. Excitation source: X-rays generated by 35kV voltage and 35mA current.	109
Figure 5.3 The photoluminescence spectrum is fitted by two different functions. (a) Lorentzian fitting, (b) Gaussian fitting.	110
Figure 5.4 The comparison between PL and RL spectra and their fitting line shape with pseudo-Voigt function. PL was measured at low power to avoid the multiexcitons generation. (a) PL spectrum shows a single symmetric peak. And the RL spectrum is fitted by the sum of two components, $y=A_1V_1+A_2V_2$, the corresponding fitting of V_1 (blue line) and V_2 (green line) are also shown in the Figure (b).	111
Figure 5.5 Normalized time resolved RL spectra of different time intervals, early time (0–0.8 ns) and later time (4–6 ns) spectra reveals a red-shifted spectrum at early times, pointing toward multiexcitons generation under X-rays excitation. X-rays illumination at a voltage of 30 kV voltage and 0.3 μ A current.	112
Figure 5.6 Normalized time-resolved fluorescence decay curves of CdSe/CdS core/crown NPLs under photoexcitation (23 μ W/cm ²) (black circle) and X-rays excitation (blue circle), red line is the tri-exponential fitting curve. Photoexcitation is measured by defocusing of 405nm pulsed laser (repetition: 500kHz) to avoid the multiexcitons.	113
Figure 5.7 Normalized steady state PL and RL spectra comparison of core/shell CdSe/CdZnS NPLs with varying shell thickness.	114
Figure 5.8 Normalized fluorescence decay curves of CdSe/CdZnS core/shell NPLs with different shell thickness in polymer under low intensity photoexcitation (defocusing), red lines are the tri-exponential fitting curves.	115
Figure 5.9 (a-c) Power dependent PL decay trace of core/shell NPLs with varying shell thickness, the traces are normalized at long tail to match the single exciton, highlighting the fast components arising at intense optical excitation. (d) The fitting lifetimes of the fast component as a function of power.	117
Figure 5.10 (a) Decay dynamics at main peak of core/shell_1 NPLs for varying power intensity. (b) The evolution of PL intensity as a function of power: slow component is extracted from (a) at 60ns and fast component is the PL intensity at 0ns after subtracting the contribution of single exciton.	119
Figure 5.11 RL and PL decay curves of core/shell NPLs with varying shell thickness. (a,c,e) normalized at long time, highlighting the multiexcitons component. (b,d,f) The fast components of different sized core/shell NPLs for X-rays excitation, obtained by subtracting the single-exciton decay. The red curve in (b,d,f) shows biexponential fitting.	120
Figure 5.12 Normalized time gated RL (a,c,e) and PL (b,d,f) of different time intervals of core/shell CdSe/CdZnS NPLs with varying shell thickness. (a, b) core/shell_s, (c,d) core/shell_m, (e,f) core/shell_l. X-rays illumination at a voltage of 30 kV voltage and 0.3 μ A current. The laser intensity is \sim 33 μ W.	123

Figure 5.13 Normalized steady state PL and RL spectra for core/crown/shell CdSe/CdS/CdZnS NPLs. The power of photoexciton source is low with 405nm wavelength.	124
Figure 5.14 Normalized PL spectra with different power intensity for C/C/S NPLs solution sample. Excitation source: OPO with 405nm wavelength and 50Hz.	125
Figure 5.15 Normalized time gated PL for C/C/S NPLs in different time intervals as indicated in the figures under different power intensity. (a) Laser power is 4nW, (b) and (d) the slices for 0-60ns and after 60ns at laser power 33 μ W. (c) The position of the main peak and the change of the spectral width over time at laser power 33 μ W.	126
Figure 5.16 Normalized RL spectra for C/C/S NPLs in different time intervals as indicated in the figures under X-rays excitation with 30kV accelerating voltage.	127
Figure 5.17 (a) Decay dynamics at main peak of C/C/S NPLs for varying power intensity. (b) The evolution of PL intensity as a function of power: slow component is extracted from (a) at 75ns and fast component is the PL intensity at 0ns after subtracting the contribution of single exciton.	127
Figure 5.18 (a) RL and PL decay curves of core/crown/shell CdSe/CdS/CdZnS NPLs well normalized at long time, highlighting the multiexcitons component. (b) Biexciton fitting of fast component under X-rays excitation, obtained by subtracting the decay curve under photoexcitation from (a).	128
FigureA2.1 (a,c,e)Emission spectra of SQWs with varying shell thickness under varying laser power. (b,d,f) The evolution of integrated PL intensity as a function of excitation power.	138
FigureA2.2 Emission spectra of CdSe/CdS nanoplatelets under varying laser power.(b) The evolution of integrated PL intensity as a function of excitation power.....	139
FigureA2.3 Emission spectra of CdSe/CdZnS nanoplatelets with varying shell thickness under varying laser power.	139
FigureA3.1 Schematic representation of the device for applying voltage on NPLs: CdSe/CdZnS NPLs in polymer is sandwiched between two FTO electrodes coated on glass, epoxy glue is used to attach the second electrode.	141
FigureA3.2 (a) integrated PL spectra under applied voltage from 0V to 200V, (b) Normalized voltage-dependent PL spectra, to highlight to linewidth broadening and the red shift of the peak position as the increasing applied voltage.....	142
FigureA3.3 The red shift of PL peak position over applied voltage with respect to PL peak at 0V extracted from the spectra shown in Figure A3.2(b), fitted approximately with a quadratic function(~ 1.8) of applied voltage (red line)	142

List of tables

Table 3.1 The reaction parameters for SQWs shell growth.	60
Table 4.1 The ratio of various emission species with the neutral X.	87
Table 4.2 Exponential fitting results and excitonic species assignment of 15nm, 25nm and 40nm SQWs.	94
Table 4.3 Summary of the fitting parameters for decay dynamics under X-rays excitation of 15nm, 25nm and 40nm SQWs.	104
Table 4.4 The ratio of different excitation species to single exciton for different sized SQWs, the data extracted from the fitting of RL decay curves in Figure 4.23.	104
Table 5.1. Summary of the fitting parameters for tri-exponential decay, lifetimes with corresponding amplitudes for core/crown NPLs under laser and X-rays excitation. The average lifetimes: $\tau_{avg} = (\sum A_i \times \tau_i) / \sum A_i$, were calculated by using the respective amplitudes of each component.	113
Table 5.2 Summary of the fitting parameters for tri-exponential decay, lifetimes with corresponding amplitudes for core/shell NPLs with different shell thickness under low intensity photoexcitation and the calculated average lifetimes.	116
Table 5.3 The fitting parameters for tri-exponential decay for core/shell_s NPLs under varying power excitation.	117
Table 5.4 The fitting parameters for tri-exponential decay for core/shell_m NPLs under varying power excitation.	118
Table 5.5 The fitting parameters for tri-exponential decay for core/shell_l NPLs under varying power excitation.	118
Table 5.6 Summary of the fitting parameters for tri-exponential decay, lifetimes with corresponding amplitudes for core/shell NPLs with different shell thickness under X-rays excitation and the calculated average lifetimes.	121
Table 5.7 Summary of the fitting parameters for multi-exponential decay, lifetimes with corresponding amplitudes for core/crown/shell NPLs under low intensity photoexcitation and X-rays excitation, and the calculated average lifetimes.	128
Table A1.1 Absorption cross-section estimations for different sized SQWs	135
Table A1.2 The average number of exciton formed per nanocrystal per pulse($\langle N \rangle$) for different sized SQWs	136

List of abbreviations

ABS	Absorption
ASE	Amplified spontaneous emission
BX	Biexciton
Cd(Ac) ₂	Cadmium acetate dihydrate
Cd(myristate) ₂	Cadmium myristate
CdO	Cadmium oxide
Cd(OA) ₂	Cadmium oleate
CM	Carrier multiplication
DDT	1-dodecanethiol
FRET	Forster resonance energy transfer
FWHM	Full-width-at-half-maximum
MEG	Multiple exciton generation
MX	Multiexciton
NPLs	Nanoplatelets
OAm	Oleylamine
OA	Oleic acid
ODE	1-octadecene
PL	Photoluminescence
PLE	Photoluminescence excitation
PMAO	Poly maleic anhydride-alt-octadecene
QY	Quantum yield
QD	Quantum dot
RL	Radioluminescence
SE	Secondary excitation
SILAR	Successive ion layer adsorption and reaction
S-ODE	Sulfur-in-octadecene solution
SQWs	Spherical quantum wells
TEM	Transmission electron microscope
TOP	Trioctylphospine
TOPS	Sulfur-in-trioctylphospine solution
TOPSe	Selenium-in-trioctylphospine solution
TX	Triexciton
Zn(Ac) ₂	Zinc acetate dihydrate

Chapter 1

Introduction

With the rapid development of nanotechnology, colloidal semiconductor nanocrystals research is currently a topical area of scientific interest due to its excellent size dependent physical and optical properties. Nanocrystals are often referred to as "artificial atoms", which are characterized as adjustable emission wavelength according to the size, wide absorption range and fast luminescence decay time. Since the first controlled synthesis of colloidal nanocrystals in 1993[1], the synthetic technique is continuously improved, making it possible to prepare the nanocrystals with various sizes, compositions and shapes. In the past 20 years, breakthroughs have been made from the traditional II-VI and III-V groups to the very promising perovskite nanocrystals, and the synthesis of nanocrystals with different shapes, such as nanorods and nanoplatelets, are also enriching the application prospects. However, the increased Coulomb interaction between electrons and holes on the nanoscale significantly increase the non-radiative Auger recombination rate which becomes the major pathway for charged exciton and multiexcitons recombination, resulting in the decrease of fluorescence yield. This has become an important obstacle for nanocrystals in multi-carrier related applications. The appearance of heterostructures greatly improved the stability of nanocrystals, and also provided a great opportunity to significantly reduce non-radiative Auger recombination. To date, nanocrystals have demonstrated the outstanding optical performances in a wide range of applications including TV screens, light-emitting diodes, lasing media and solar cells[2–5]. In addition, the potential applications of nanocrystals are still being explored, in which the scintillation materials in the form of nanocrystals have recently been received great attention in the scientific field.

A scintillating material (scintillator) is a kind of converter transforming the energetic photon or particle (ionizing radiation) into low energy UV/visible photons. With the discovery of X-rays by Roentgen in 1895[6] and the emergence of the photomultiplier tube, the research of scintillators has made great progress, the scintillators have been discovered in various crystalline and non-crystalline media, one of the most used of which is the thallium-activated sodium iodide (NaI:Tl). Up to date the scintillator-based radiation detectors are widely used in nuclear medicine, high energy physics, homeland security and industrial non-destructive testing[7]. The selection of the scintillation materials depends on the particular requirements of the considered application. With the deepening of the understanding of fundamental mechanisms underlying scintillation

process, more and more materials are available and the properties of scintillators are constantly improving. At present, bulk materials still occupy the commercial scintillator market. In order to improve specific performances (timing, energy resolution...), new scintillating materials are still a very hot research direction.

Research on radiation detection related to nanocrystals gradually emerged in recent years. The first configuration was reported in 2006 and applied to the detection of gamma rays[8]. Subsequent research on nano-scintillators focused on the combination of nanocrystals with bulk materials[9,10]. Recently, scintillator in form of perovskite nanocrystals was demonstrated with remarkable performance[11]. Unlike the traditional bulk scintillators, the output wavelength of nanocrystals can be tuned span the visible light emission such that it can well match with the peak spectral sensitivity of the photomultiplier tube to improve the overall detection efficiency. Moreover, nano-scintillators have the advantages of liquid processing and convenient mass production, which can avoid the complicated procedures of high temperature fabrication and address the problem of high cost of scintillation materials. And some specific application benefit of the nanosize like in photodynamic therapy under X-rays [12,13].

In spite of many attempts have been devoted so far on different types of nano-scintillators, the scintillation mechanism in nanocrystals is still not fully described. A few articles have reported the process of energy deposition and relaxation in nanocrystals after energetic excitation. The interaction of materials with high-energy radiation basically produces a shower of high-energy electrons, which will multiply, thermalized and excite emitting centers. Due to the very small size, below the main migration distances of the involved species, the energy deposition and the distribution of excited states in nanocrystals will be significantly different from bulk materials. In addition, regarding the identification and quantification of excited states under high-energy electrons was reported[14], the preliminary observation indicated that after initial electron shower, in the process of energy relaxation down to band states within a nanocrystal, carrier multiplication and electrons scattering played an important role, leading to the formation of multiexcitons states and charged exciton states. Meanwhile, they also pointed out that Auger recombination seriously hindered the development of nano-scintillators. We believe that a more comprehensive understanding of the scintillation mechanism in nanocrystals is needed to improve and discover novel scintillation materials.

1.1 Aim of the thesis

Motivated by potential of nanocrystals for radiation detection application, this thesis aims to explore the process of energy deposition and charging in nanocrystals under ionizing radiation with different II-VI heterostructures, including spherical quantum well and heterostructural nanoplatelets. The excited states dynamics, especially Auger recombination and multiexcitons will be investigated with optical spectroscopy techniques including steady state spectroscopy and time resolved technique. By comparing with intense optical excitation temporally and spectrally, we are able to verify

and identify the formation of multiexcitons states under X-rays excitation. Meanwhile, through the investigation on the particles with varying sizes, we will analyze the size dependence of the scintillation response, that is, the evolution of ratio of excitonic species with the particle size.

1.2 Organization of the thesis

The thesis is organized in 6 chapters as follow:

In Chapter 2, we present the fundamental concepts necessary to the understanding of this thesis. First, we introduce the quantum confinement effect and surface effect of colloidal semiconductor nanocrystals, and also introduce spherical quantum wells(SQWs), nanoplatelets(NPLs) and their heterostructures in detail. Secondly, we discuss the exciton dynamical processes in NCs, where mainly emphasize the formation and recombination of multiexcitons. Finally, we also describe the scintillation mechanism of bulk scintillators and the development of nano-scintillators.

In Chapter 3, we first present the synthesis principles of core NCs and the heterostructures. Secondly, the characterization techniques used for the detailed investigation of the structural and optical properties in this thesis are briefly introduced. We also report the synthesis of CdS/CdSe/CdS SQWs with varying shell thickness, and different heterostructural NPLs, core/crown, core/shell and core/crown/shell, together with their characterization.

In Chapter 4, we first describe the steady-state radioluminescence spectroscopy, the time-resolved experiments. We also performed the spectral and dynamical measurements with various sized SQWs under the optical and X-rays excitation. By comparing with simulation, we also presented the identification of the excitonic species during scintillation process and further the investigation on their evolution with particle size.

In Chapter 5, we describe the investigation of the scintillation performance of different II-VI nanoplatelets with steady-state spectroscopy and time-resolved methods, including core/crown, core/shell, and core/crown/shell NPLs in which three-sized core/shell NPLs was performed for the comparison.

The Chapter 6 concludes the work and discuss future outlooks.

Chapter 2

Scientific background

In this chapter, before presenting our findings and related discussion, we first introduce the scientific background on colloidal semiconductor nanocrystals and the excited state dynamics, specially the Auger non-radiative recombination and the multiexcitons. Second, we briefly describe the scintillation mechanism and the state of the art of the nanocrystals scintillators, and finally we introduce the optical and electronic properties of two kinds of nanocrystals: spherical quantum wells(SQWs) and nanoplatelets(NPLs).

2.1 Colloid semiconductor nanocrystals

Colloidal semiconductor nanocrystal(NCs) is a nano-sized semiconductor material containing 100-100000 atoms. The size is smaller than or comparable to the exciton Bohr radius of the bulk material, therefore the NCs are subjected to quantum confinement effect, resulting in a quantized energy level and an adjustable energy gap. After first proposed by Ekimov in 1981[15], NCs have attracted great attention due to their fascinating chemical and physical properties, in which II-VI NCs are the most studied, such as CdSe, CdS and ZnS. The ability to precisely control the composition, size, and shape of II-VI NCs has been successfully realized and provides great flexibility in the engineering of their electronic and optical properties. Also, by combining different materials, various types of heterostructures, like CdTe/CdSe, CdSe/ZnS, have been fabricated to specifically alter the excitonic features of NCs to obtain desired characteristics. Nowadays, II-VI NCs has made outstanding progress in lasing media, single-photon sources, photovoltaic conversion, display devices, and biological imaging. With the continuous development of nanocrystals, its applications in other fields are constantly being explored.

2.1.1 Quantum confinement effect

An important parameter of a semiconductor material is the width of the energy gap that separates the conduction from the valence energy bands controlling the emission luminescence wavelength[16]. When a semiconductor absorbs a photon with energy equal to or larger than its energy gap, an electron can be excited from the valence band to the conduction band, leaving a hole in the valence band, and the formed electron-hole pair bound by Coulomb interaction is referred as an exciton. It has lowest energy state

slightly below the edge of the conduction band, which can recombine radiatively to emit a photon[17]. For bulk semiconductors, the energy band structure depends on the element composition and lattice structure and it is a fixed parameter. A natural length scale of the bounded electron-hole in the hydrogen like structure is given by the exciton Bohr radius, a_B , which is determined by the strength of the electron-hole Coulomb interaction.

$$a_B = \varepsilon a_0 \frac{m_e}{m^*} \quad (2-1)$$

where ε is the dielectric constant of the material, a_0 is the Bohr radius of hydrogen atom ($a_0 = 4\pi\varepsilon_0\hbar^2/m_e e^2 \sim 0.53\text{\AA}$), m_e is the rest mass of the electron and m^* is the reduced mass of the effective electron-hole pair. Exciton Bohr radius is a materials intrinsic property. In this thesis, exciton Bohr radii of semiconductors we used is 2.9nm for CdS and 5.6 nm for CdSe.

In the case of semiconductor NCs with size comparable or smaller to the bulk exciton Bohr radius, confinement effect becomes important. Electronic energies depend directly on the degree of spatial confinement of electronic wave functions. One consequence of this is the valence and conduction band edges change from continuous to discrete energy levels, and the band gap of the NCs gradually increases as the size decreases, as presented in Figure 2.1. This phenomenon is known as the quantum confinement effect, which makes it possible to achieve continuously adjustable wavelength in NCs by simply tuning their size and shape[16,18].

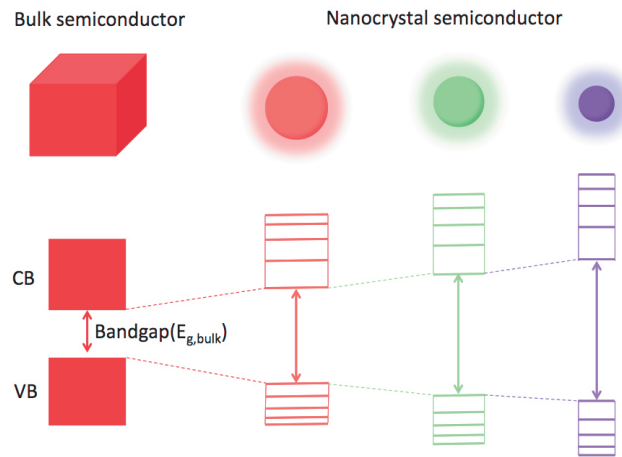


Figure 2.1 Schematic representation of quantum confinement effect: a bulk semiconductor with continue energy band and a fixed energy gap $E_{g,bulk}$, while NCs possess discrete energy levels and the band gap energy increases with decreasing size.

The energy level structure of NCs can be calculated through the effective mass approximation theory, assuming a spherical nanocrystal with a radius of r , the bandgap of NCs can be expressed as[19]:

$$E_g = E_g^{bulk} + \frac{\hbar^2 \pi^2}{2r^2} \left(\frac{1}{m_e} + \frac{1}{m_h} \right) - \frac{1.8e^2}{4\pi\epsilon_r\epsilon_0 r} \quad (2-2)$$

Here E_g^{bulk} refers to the band gap of this material in bulk, \hbar is Planck's constant, m_e and m_h are the effective masses of electron and hole, respectively and e is the charge. ϵ_0 is the dielectric constant in vacuum and ϵ_r is the relative dielectric constant of the material. The middle item on the right is the energy gap change caused by the quantum confinement effect, and the last item on the right is related to the electron-hole Coulomb interaction, which is the binding energy of exciton. The confinement energy is proportional to $1/r^2$ whereas the exciton binding energy is proportional to $1/r$, leading to the dominance of the confinement effect. Therefore, we can see that within the confinement effect size range, as the size decreases, its energy gap will gradually become larger. Just by adjusting the size, nanocrystals with different energy gaps can be obtained.

On this basis, the theoretical and experimental works have further studied the discrete atom-like energy levels of NCs and the corresponding transition selection rules[20]. Figure 2.2(a) shows the electron and hole energy level structure of CdSe NCs with different sizes. $1S_e$, $1P_e$, $1D_e$ and $2S_e$ are the electron energy levels, and $1S_{3/2}$, $1P_{3/2}$ and $2S_{3/2}$ are the hole energy levels. It can be seen from the figure that the band gap of NCs increases as the size decreases. Since the effective mass of CdSe NCs holes is much larger than the effective mass of electrons, the electron energy level spacing is larger, and the hole energy levels are relatively tight. Moreover, for several lowest transitions, the experimental results of energy changes with particle size are highly consistent with theoretical calculations, as shown in Figure 2(b).

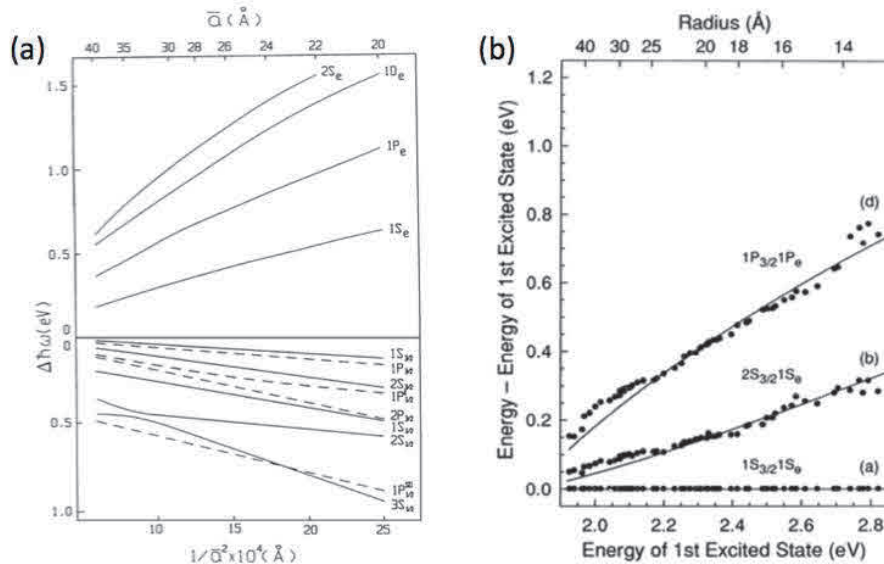


Figure 2.2 (a) Theoretical calculation on size dependence of the electron and hole energy levels in a CdSe quantum dot (QDs). (b) The comparison between theoretical and experimental data for several of the lowest transitions[20].

The quantum confinement effect can occur in any dimension of a semiconductor material. Different confinement dimensions cause the different density of states of the semiconductor energy level. Figure 2.3 shows a schematic of the density of states as a function of dimensionality, going from three-dimensional (3D, bulk) to zero-dimensional (0D, QDs) systems. In bulk materials, the charge carriers are free to move in all three dimensions. The bands are square root dependent of their energy ($\sim E^{1/2}$). For a two-dimensional (2D) material, referred to as quantum well or nanoplatelets, only the thickness of this nanocrystal is smaller than the exciton Bohr radius and excitons can freely move in the lateral directions. So the density of states is affected by the decreased number of freedoms for the charge carriers, resulting in step-like density of states. And for one-dimensional (1D) materials such as nanowires and nanorods, the quantum confinement effect plays an important role in two dimensions, this results in a saw-like density of states with an inverse square energy dependence ($\sim E^{-1/2}$). Finally, the semiconductor material confined in all three spatial dimensions is referred to as quantum dots, they show discrete atom-like energy levels [17,21]. This unique property caused by shape dependence have greatly stimulated enormous interest in exploring novel classes of materials with various electronic and optical characteristics.

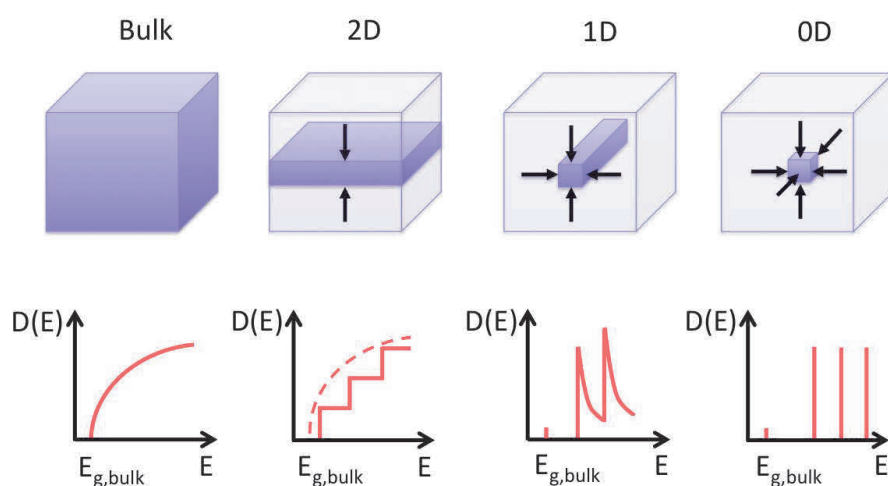


Figure 2.3 Schematic diagram of the density of states as a function of dimensionality. Bulk materials (3D) without quantum confinement effects in three dimensions; 2D refers to quantum wells with quantum confinement effects in only one dimension; 1D refers to rod-shaped or wire-shaped nanocrystals restricted in two dimensions; 0D mainly refers to quantum dots confined in three dimensions.

2.1.2 Surface effect

Surface effect is another well-known nanoscale effect that causes different properties of NCs compared to bulk materials. The surface-to-volume ratio of NCs increases sharply as the particles size decreases. For bulk solids, their size is indeed much larger than the exciton Bohr radius of the particle, and most of the carriers are far away from the surface. Therefore, the influence of surface atoms on the material's properties is basically

negligible for penetrating radiations, whereas the size of NCs is smaller than the exciton Bohr radius, carriers are easily affected by the surface. Therefore, NCs will be very sensitive to surface and environmental changes. The surface effect becomes more and more important on stability and optical properties of NCs with the further reduction of size. Compared with internal atoms, surface atoms have fewer neighbors, and therefore possess unsatisfied chemical bonds, which is referred as dangling bonds. The increasing fraction of surface atoms leads to many dangling bonds, inducing defects on the surface. These defects will bring additional energy levels into forbidden band, considered as trap center to capture the charges created during an excitation, which is detrimental to the high quantum efficiency pursue through non-radiative recombination pathway. In addition, the increase in dangling bonds will increase the surface free energy, leading to the instability, and NCs will tend to aggregate. This aggregation process is often irreversible, which greatly damages the optical properties of NCs and limits its application[22,23]. Thus, reasonable elimination of dangling bonds and defects at the surfaces is often required to improve NCs performance.

To achieve the passivation of the surface, people utilize the ligands on the surface of NCs to form strong bonds with surface atoms to fill the dangling bonds, improving the chemical stability. The common binding groups of ligands are carboxyl, amino, and sulfhydryl groups. One end of the ligand is coordinated with the atoms on the surface, and the other end is compatible with the solvent to provide solution stability. The choice of hydrophilic and hydrophobic ligands depends on the polarity of the solvent. However, some types of ligands have been reported to quench optical properties of NCs, it is important to choose the suitable ligands[24]. Alternative passivation method is to overcoat a shell composed of different materials, creating a heterostructure, which is referred as core/shell structure[25,26]. The existence of a shell makes it possible to isolate the emissive core from its environment, which makes the NCs more stable and robust, and less sensitive to changes in its environment. The core/shell heterostructure will be discussed in detail in the following section.

2.2 Heterostructural nanocrystals

Heterostructural nanocrystals consist of a quantum dot core and a shell of a (or more) distinct material. By using heterostructures instead of bare core NCs, the ability to create novel optoelectronic properties can be extended further. The core and the shell are typically composed of type II–VI and III–V semiconductors. This structure was demonstrated to address the low quantum yield issue of bare NCs with surface related defects by passivating the surface trap states. What's more, the formation of shell can isolate the emissive region with its environment, providing protection against environmental changes and photo-oxidative degradation[22,26].

Core/shell semiconductor nanocrystal properties are based on the relative conduction and valence band edge alignment of the core and the shell. The spatial localization of the charge carriers in heterostructure can be manipulated by controlling the band offsets of the materials[26]. Furthermore, the lattice parameters of shelling materials should be

close to that of the core to reduce lattice stress created by the lattice mismatch and to facilitate epitaxial growth on the core. On the contrary, the growth of the shell results in strain, accompanied by the generation of defects at the core/shell interface or within the shell. These defects can act as trap states to capture the photo-generated charge carriers and diminish the fluorescence quantum yield. As illustrated in Figure 2.4, according to the shell materials and the energy band alignment, core/shell nanoparticles can be divided into three types:

- (1) Type I: the conduction band energy of core material is lower than that of shell whereas the valence band energy of core is higher than that of shell. As a consequence, both electron and hole are confined within the core, making it possible to separate physically the surface of the optically active core from its surrounding medium. Due to the well surface passivation with respect to bare core, coating wide band gap materials is usually employed to reduce non-radiative recombination, which enhances photoluminescence quantum yield and the chemical stability against photo-degradation. In addition to the improvement in quantum yield, shell growth is accompanied by a small red shift of the excitonic peak in the absorption and photoluminescence spectrum. This observation is attributed to a partial leakage of the wavefunction into the shell material. The first published configuration was CdSe/ZnS[27]. However, the lattice parameter mismatch(12%) between CdSe and ZnS limit strongly the continuous growth of shell without the formation of interface defects[25].
- (2) Quasi type-II: one carrier is delocalized over the whole nanocrystal, while the other is localized in one of the materials. The most investigated composition is CdSe/CdS. This allows the electron-hole spatial overlap to be tailored by controlling the size of shell. The delocalization of one carrier reduces the confinement effect, making it possible to tune the emission color over a large range. Therefore, the redshift in spectra upon shell grown is usually larger than that observed in type I. Moreover the lattice parameter mismatch of typical structure CdSe/CdS is only 4%, which conduces to the synthesis of the giant core/shell nanoparticle[3]. The reduction of electron-hole wavefunction overlap as the shell decreases the radiative transition probability and thus increases the exciton lifetime. Due to the decreased Coulomb interaction, Auger recombination rate is concluded to decrease in this configuration, making it feasible for the investigation of multiexciton properties and the suppression of blinking phenomenon[28].
- (3) Type II: In contrast to type I, both conduction level and valence level of one material are higher than the other one, therefore one of either the electron or holes is localized in the core while the other is confined in the shell. The separation of carriers leads to the significant reduction in wavefunction overlap, like quasi type II, which has the effect on elongated lifetime of exciton. The emission wavelength is determined by the energy difference between the occupied states, which will be at a lower energy than either of the

individual energy gap. This configuration thus has been developed in particular for near infrared emission.

The continuous development of heterostructure enables it to satisfy multiple requirements of appropriate electronic and structural parameters simultaneously. For instance, multi-shell structure can realize the decrease of defect induced by lattice mismatch between the core and an outer shell by adding an intermediate layer, such as CdSe/ZnSe/ZnS[29]. Compared to the traditional core/shell structure, it has proven to be more stable and higher quantum yield. Another structure is gradient core/shell NCs with smooth interfacial potential[4]. The further reduced steepness of the interfacial potential makes this configuration a great success in suppressing the Auger effect.

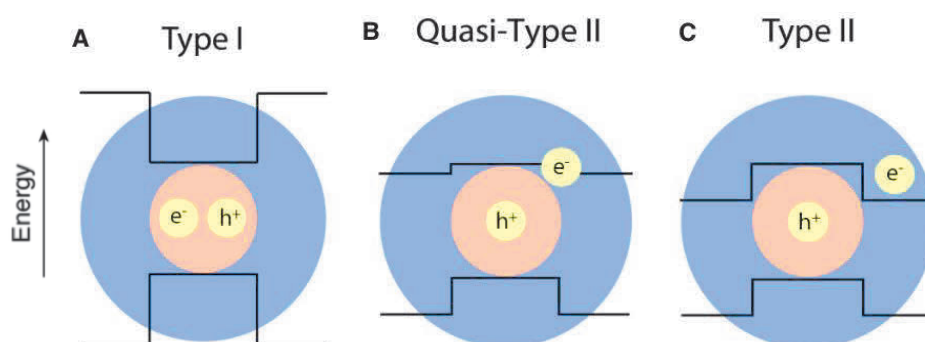


Figure 2.4 Schematic representation of the energy level alignment and charge carrier localization in type I, quasi-type II and type II core/shell hetero-structural NCs, respectively[30].

2.3 Excited state dynamics under photoexcitation

Figure 2.5 is the simplified picture of the exciton dynamical processes in NCs under photoexcitation, as mentioned above, the absorption of a photon in nanocrystals can excite an electron from the valence band to the conduction band, leading to the formation of exciton. Subsequently, the exciton will undergo a series of processes, including relaxation and recombination, to dissipate the energy. This sequence of events involves time scales from a few femtoseconds to a few seconds after photoexcitation[17].

The possible pathways strongly depend on the specific excitation conditions (excitation energy and intensity). For the incident moderate energetic photon ($E = \hbar\omega > E_g$), it will produce hot exciton with excess energy, typically the hot exciton rapidly loses its energy as heat or is trapped by defects. If the system is excited under high-energy photon (in principle $E = \hbar\omega \geq 2E_g$) or high-intensity excitation, the carrier multiplication process will take place, resulting in the formation of the multiexcitons, this will greatly complicate this whole dynamical process. Eventually, exciton is able to emit photon through radiative recombination or lose the energy via the non-radiative recombination, which is mainly caused by sample defects and Auger non-radiative recombination, relaxing the NCs back to the ground state. Here, the main possible excited state dynamics

processes in NCs under different excitation conditions are explained in detail in the following sub-section. An understanding of the rates and pathways of exciton relaxation and recombination processes in NCs is very important for the comprehension of the fundamental physics as well as their utilization in applications.

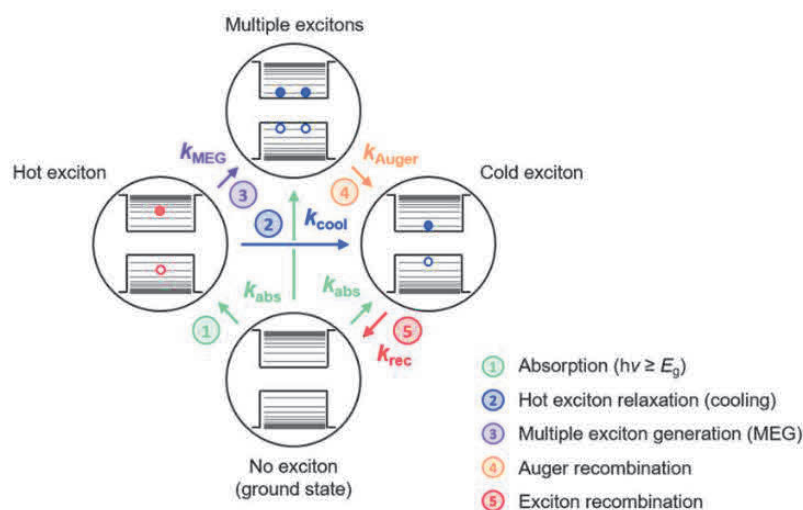


Figure 2.5 Schematic representation of possible relaxation and recombination processes in NCs after photoexcitation. (1) exciton is generated by absorption of a photon with energy $h\omega \geq E_g$ or more photons are absorbed to form a multiexcitons state. (2)The hot exciton may relax to band edge by cooling process. (3)If $h\omega \geq 2E_g$, two or more excitons can be created through carrier multiplication(or multiple exciton generation, MEG) . (4)Multiexcitons will recombine radiatively to emit photon or non-radiatively via Auger recombination. (5) Eventually, the exciton recombines, relaxing the NCs back to the ground state[31].

2.3.1 Hot carriers relaxation

When the excitation energy is equal to the bandgap energy, it is referred to resonant excitation. On the other hand, in a general case, the photon energy is greater than the band gap, usually leading to both electron and hole occupy high levels in the conduction and deep ones in the valence band, this process is known as non-resonant excitation. And the carriers with excess energy are usually referred to as ‘hot carriers’. In bulk semiconductors, the created hot carriers rapidly return to the band edge via phonon-assisted emission in an ultrafast process. This process is typically in hundreds of femtoseconds due to the strong coupling of carriers and phonons within the continuum of energy states. However, when we considered the nanocrystals, the cooling process is significantly different. As the size of the nanocrystals decreases, the discretization of electronic states appears near the band edges, and the electronic intraband spacing will continue to increase with the confinement till hundreds of meV, which is larger than the maximum phonon energy with only tens of meV, preventing the charge carrier relaxation[32]. Auger-type energy transfer is generally accepted as the alternative process. Due to the larger effective mass of hole, valence band possesses a much higher

density of state, making the smaller hole energy states spacing in valence band than electron energy states spacing in conduction band. Hence the electron transfers its excess energy to the hole through the Auger type energy transfer, accompanying with the relaxation to the edge of conduction band. Subsequently, holes dissipate the energy rapidly with the assist of photons[33].

2.3.2 Exciton recombination

Once the electron and hole have relaxed to their respective band edge, subsequently excitons can recombine through radiative and non-radiative recombination. For radiative recombination, the exciton is released in the form of emitted photons. And the energy of emitted photon is equal to about the bandgap minus the bond energy. This characteristic rate is referred to as radiative rate k_r . Sometimes the radiative recombination related to the trapped carriers may also occur, which is called trap emission. For non-radiative recombination, several types of this phenomenon are possible in nanocrystals. Since the presence of defects and dangling bonds in nanocrystals, carriers are captured and blocked in these sites, the emission can be quenched. In addition to the qualities of the particles, Auger effect also is part of the origin of non-radiative recombination in charged and multiexcitons. The characteristic rate is referred to as non-radiative rate k_{nr} . Non-radiative pathways extremely diminish fluorescence quantum yield. If we consider N_e is the population of excited states at time $t = 0$, the evolution of this population will be defined by:

$$\frac{dN_e}{dt} = -kN_e(t) \quad (2-3)$$

Here the rate k can be expressed by the fluorescence lifetime τ . The fluorescence lifetime is the time measured for the number of excited states to decay to 1/e of the original population via the loss of energy through radiative or nonradiative processes.

$$k = k_r + k_{nr} = \frac{1}{\tau_r} + \frac{1}{\tau_{nr}} = \frac{1}{\tau} \quad (2-4)$$

So $N_e(t)$ which is the number of excited states at time t is supposed in simple case to be expressed by the single exponential decay equation of excited states as follow:

$$N_e(t) = N_e(0)e^{-kt} = N_e(0)e^{-\frac{t}{\tau}} \quad (2-5)$$

Fluorescence quantum yield is one of the most important characteristics of fluorophores. It is defined as the ratio of the number of emitted photons to the number of absorbed photons. Since the exciton recombination in nanocrystals usually involves many radiative and non-radiative processes, the quantum yield depends on the various recombination pathways and can be written as:

$$QY = \frac{k_r}{k_r + k_{nr}} \quad (2-6)$$

2.3.3 Auger recombination

Excitation of nanocrystals may lead to charged particles and in such situation Auger recombination is the main non-radiative pathway for energy dissipation, which is mediated by Coulomb interactions between carriers. This process plays an important role in semiconductor nanocrystals when there are three or more charge carriers present, which are referred as trion and multiexcitons. Here, we take trion as an illustration, which is also called as charged exciton. The formation of charged exciton is usually attributed to the charged carriers trapping or Auger ionization. A schematic diagram Auger recombination in charged exciton system is illustrated in Figure 2.6: instead of emitting photons as neutral single exciton by radiative recombination, the energy is transferred to the additional carrier (electron in the conduction band), subsequently promoting it to higher excited energy level, and then dissipated as heat by phonon-assisted thermal process. In direct-gap bulk semiconductors, this process needs to satisfy both energy and translational momentum conservation requirements and hence it exhibits a thermally activated behavior. Additionally, strong spatial overlap of wavefunctions for all carriers is required. Therefore, Auger recombination can only be observed at higher electron–hole pair density. However, in nanocrystals, only energy-matching conditions are needed to be met because of the no well-defined translational momentum, together with the enhanced Coulomb interactions owing to the increased spatial confinement strongly improve the efficiency of Auger effect with respect to that of bulk materials[18], and it can occur for band edge carriers. The timescale of this process is typically on the order of 1–100ps, depending on exciton multiplicity, the size shape and composition, which is faster than that of radiative recombination. A general trend observed of Auger decay rate in core NCs is a linear dependence of Auger lifetimes on NCs volume, which is referred as “universal volume scaling law”[34]. There have been a few recent exceptions to this universal volume scaling of Auger rates in 2D nanoplatelets[35]. The Auger effect in nanoplatelets was demonstrated more sensitive to the changes in vertical thickness(d) with a scaling factor of d^7 , indicating its strong dependence on the degree of confinement. Meanwhile it increases linearly with its lateral area, reflecting the dependence of exciton-exciton collision frequency.

Basically, Auger process has always been considered as the dominant reason for the photoluminescence intermittency in single quantum dots and the reduction of quantum yield[36]. Since the net result of this process is energy loss as heat, the Auger quenching is the main obstacle to commercial application of nanocrystals that require high efficiency, such as light-emitting diodes (LEDs) and lasing medium[17]. In the last decades, a lot of endeavors have been made to inhibit the Auger process. As discussed above, Auger lifetime is involved in spatial confinement of charge carriers. Therefore, the Auger recombination rates can be reduced by increasing the size of nanocrystals with weak confinement complication. Besides, the degree of spatial overlap between the electron and hole wave functions is considered as another influencing factor. Heterostructures based on type II and quasi type II core/shell, have been continuously developed to manipulate the overlap of electron and hole pair. Common configuration CdSe/CdS with thick shell has showed outstanding performance on Auger effect

suppression, the Auger rate can even be prolonged to several nanoseconds[3]. In addition, some research also report alloyed interface with smooth confinement potential leads to the suppressed Auger process, leading to a rather high quantum yield of multiexcitons[37,38]. Indeed, Auger recombination rate in nanocrystals strongly depends on the size, shape and potential steepness of the interface. Increasing requirements of high quality nanocrystals demands us to further understand the underlying physics of Auger recombination and reduce the Auger losses.

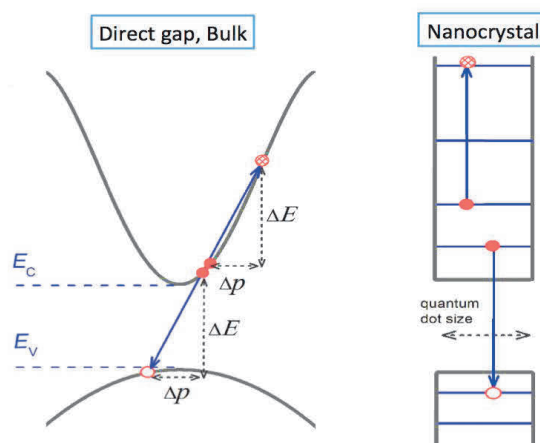


Figure 2.6 Schemes showing the difference between Auger recombination process in direct gap bulk (left) and NCs (right) semiconductors. ΔE and Δp present the change of energy and momentum, respectively. E_c and E_v are the edge of conduction and valence bands. Compared to bulk material, the requirement of momentum conservation is largely relaxed in NCs and Auger recombination occurs efficiently for band edge carriers [18].

2.3.4 Multiexcitons recombination

As we discussed above, on the consequence of strong carrier-carrier Coulomb interaction in nanoscale, the efficiency of Auger non-radiative recombination is significantly enhanced, which represents the predominant pathway of multiexciton decay[34,39,40]. The emergence of large-size and gradient NCs provided an excellent opportunity to exploitation of multiexcitons. The suppression of the Auger effect has greatly improved the fluorescence quantum yields of single excitons and multiexcitons of these NCs. And this breakthrough has provided a good opportunity to explore the huge potential of the multiexcitons phenomena in the application of semiconductor nanocrystals, such as low-threshold NCs lasers, light emitting diodes, as well as solar-energy conversion[3,4]. The realization of all of these applications requires detailed understanding of dynamical and spectral properties of multiexcitons in nanocrystals. Hence, we introduce briefly the optical and electrical properties of biexciton and triexciton, and the carrier multiplication process.

2.3.4.1 Biexciton

The multiexcitonic state composed of two excitons in a single nanocrystal at the same time is the simplest configuration of neutral multiexcitons, referred to biexciton. Through nonradiative pathway, biexciton annihilates an electron-hole pair and pass the energy to other carriers (either electron or hole), exciting the carriers to high energy state or even ionizing them out of the particles to form the charged exciton.

Multiplicity of recombination pathways accelerates the radiative lifetime of multiexcitons. The nonlinear scaling of radiative rate constants of N-exciton states (τ_{Nr}) with N was analyzed by Klimov et al. in 2008[41]. They proposed “free-carrier” model and predicted experimentally and theoretically τ_N likely scales as N^2 in PbSe NCs. Therefore although the scaling factor of two has also been reported for biexciton[42], the relationship generally accepted between the exciton and biexciton radiative rates is $\tau_{1r} = 4\tau_{2r}$. On the basis of recombinations of the possible electron and hole angular momentum states, Katherine E. Shulenberger theoretically and experimentally explained the origin of statistical scaling factor of four. Due to angular momentum selection rules, only half of the excitons are available to radiatively recombine in exciton, and in biexciton two spin-paired exciton can recombine independently, giving rise to a radiative speed up by a factor of two compared to a single spin-paired exciton. The combination of the factors results in a biexciton radiative rate four times faster than that for the exciton[43]. Recently, the development of the suppression of Auger effect makes the fluorescence quantum yield of single excitons and biexcitons reach nearly 100%[37,44]. The lifetime of biexciton also composes with radiative and Auger non-radiative items, $k_2 = k_{2r} + k_{2A}$. Therefore, according to the statistical scaling, the emission quantum yield of biexciton is expressed in Eq 2-7, allowing us to calculate it directly with the exponential fitting parameters of the decay curves.

$$Q_{2X} = \frac{k_{2r}}{k_{2r} + k_{2A}} = \frac{\frac{1}{\tau_{2r}}}{\frac{1}{\tau_{2r}} + \frac{1}{\tau_{2A}}} = \frac{\tau_2}{\tau_{2r}} = \frac{4\tau_2}{\tau_{1r}} \quad (2-7)$$

To further understand the spectral and temporal properties of biexciton, the interaction between exciton and exciton is another important problem to investigate, which is often defined as $\Delta_{BX} = E_{BX} - 2E_X$, where Δ_{BX} is interaction energy, and E_X and E_{BX} are single exciton and biexciton energies, respectively[45]. The magnitude and sign of the interaction energy depend on the spatial distribution of electrons and holes, which is the electrons and holes wavefunction overlap integral. Therefore, different energy band alignments will lead to different Coulomb interaction energies. Specifically, in type I nanocrystals, both electrons and holes are restricted in the same area, as shown in Figure 2.7(a), the interaction force between excitons is attraction, which corresponds to the negative binding energy of biexcitons, leading to a red shift with respect to single exciton on the spectrum. It has been observed in bare nanocrystals and type I samples such as CdSe/ZnS[40,46]. On the contrary, in the quasi-type II and type II structures, the alignment of the energy bands causes the difference in the distribution of electrons and

holes, which leads to the imbalance of local charges. The repulsive force between excitons and excitons has been reported in CdSe /CdS, CdS/ZnSe and other structures, as seen in Figure 2.7(b), and a blue shift relative to single exciton is caused[47]. However, in few recent studies, they achieved to control the nature and strength of exciton– exciton interactions by adjusting the core-shell sizes with CdSe/CdS structure. The biexciton shift transiting from red-shift to blue-shift regimes in a single material system has been observed, typically, thin shell was demonstrated to exhibit the attractive interaction due to the negligible delocalization of the electron wave function. Therefore, the tunable amplified spontaneous emission(ASE) has been realized by engineering biexciton interactions[48,49]. Taking direct carrier-carrier Coulomb coupling and interface polarization into account, Andrei Piryatinski[45] theoretically calculated the biexciton binding energy of type II structure by perturbation theory. Due to the large degree of spatial separation between electron and hole, the repulsion energy in type II can reach to the order of 100meV. While in quasi-type II, because of the delocalization of one carrier, the relatively enlarged wavefunction overlap of electrons and holes reduces the interaction energy, on the order of 10 meV.

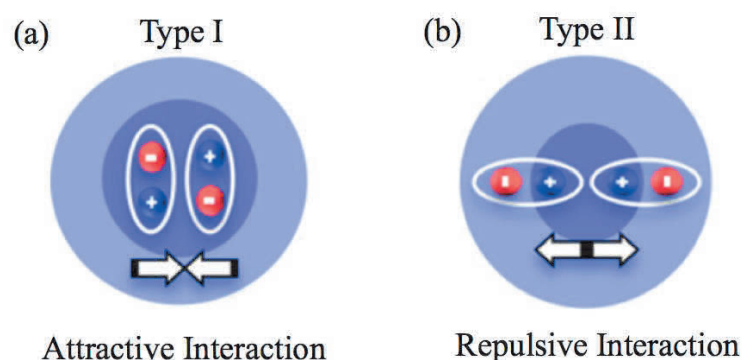


Figure 2.7 Schematic diagram of the exciton and exciton Coulomb interaction in nanocrystals: (a) attractive force, (b) repulsive force[48].

2.3.4.2 Triexciton

In comparison with biexciton, the situation of triexcitons is extremely complicated, because it involves not only the lowest energy quantized state, but also a higher P energy level. According to Pauli's exclusion principle, the conduction band of CdSe is composed of the 5s orbital of cadmium, so the lowest quantized state 1Se at the bottom of the conduction band can only contain two electrons with opposite spins. While the top of valance band is made up of six degenerate 4p atomic orbital of selenium, ignoring the spin-orbit coupling, the lowest energy level $1S_{3/2}$ state of the hole is four-fold degeneracy and can accommodate up to four holes. Since the effective mass of the hole is larger, the energy level interval of the valance band is smaller, p-like hole states can be populated as a result of thermal activation in the triexciton ground state[40,50]. The occupation of the 1P state can only be stable when the 1S state is fully filled. Based on these studies, P-

level related emission will appear at high-energy positions with respect to single excitons, approximately to 200meV[51].

Similar to biexciton, the efficient Auger process seriously hinders its application. In the past 20 years, thanks to the development of ultrafast optical instruments, such as time-resolved spectroscopy, high-energy triexciton emissive feature has been widely reported[46,51]. What's more, on the basis of the study regarding Auger effect suppression, Florencio García-Santamaría et al. observed the pronounced change of emission color in amplified spontaneous emission experiments with giant CdSe/CdS NCs[3]. And the yield of white light emission was observed by Michel Nasilowski et.al, suggesting the effective improvement of high-order(>2) multiexcitons efficiency by synthesized gradient interfacial NCs[37].

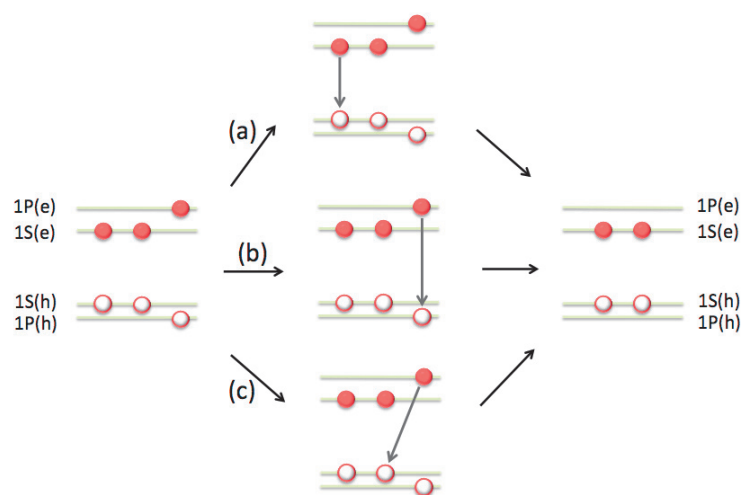


Figure 2.8 Schematic diagram of the different radiative recombination pathways for triexciton in CdSe quantum dots. (a) The triexciton can decay by S-S electron-hole recombination, leading to an excited biexciton, following by the thermal process, (b) or by P-P recombination, leading to a ground-state biexciton, (c) or via the nominally forbidden $1P_e-1S_h$, also followed by a thermal process. Finally, each of these three pathways can bring the system to the ground-state biexciton.

Most of the current studies on triexcitons are based on the differences in spectra, and the predominant recombination pathways for triexcitons remain poorly understood. The generally accepted decay mode is a cascade stepped decay: $TX \rightarrow BX \rightarrow X \rightarrow$ ground state. But the specific process from $TX \rightarrow BX$ is still very controversial. As shown in Figure 2.8, there are three possible recombination pathways, which are S-like: $1S_e-1S_h$, and P-like: $1P_e-1P_h$, $1P_e-1S_h$. Most reports so far acquiesce that this process is completed by P-like transition[51,52]. In 2018, Katherine E. Shulenberger[43] demonstrated that S-like and P-like occur simultaneously, and the S-like transition is dominant through the third order correlation of single CdSe/CdS NCs. In the same year, Jaehoon Lim[4] discovered that the 1P lasing threshold is slightly lower than the theoretical value for the $1P_e-1P_h$ transition. They attributed it to the occurrence and dominance of the $1P_e-1S_h$ transition

pathway. According to the transition selection rule, 1P-1S transition is prohibited. However, due to close proximity between the corresponding energy levels in the valence band, the energy difference between $1S_{3/2}$ and $1P_{3/2}$ is almost negligible, even on a large size scale of nanocrystals, the effect of mixing of the band-edge 1S and 1P hole states can be significant, leading to the permission of 1P-1S transition. In addition, this asymmetric transition has also been proven in many other reports regarding the charged biexciton and triexciton[40,47]. However, in the spectral profile, these two different P-like transitions in CdSe nanocrystals are difficult to be distinguished.

2.3.4.3 Carrier multiplication

Generally, absorbing one photon with moderate energy ($E_g < E < 2E_g$) create only one hot exciton, the excess energy will be released as heat by interacting with phonons (Figure 2.9(a)). When a single high-energy photon ($> 2E_g$) is absorbed, carrier multiplication (CM) has been observed in bulk semiconductors since the 1950s and explained by impact ionization[53], where the hot electron dissipates the energy by pumping the carrier cross the bandgap, forming the additional electron-hole pair, as illustrated in Figure 2.9(b). However, in bulk semiconductors, due to strict momentum conservation and very effective phonon-assisted attenuation, the efficiency of carrier multiplication is considerably low. The no well-defined translational momentum and the strong Coulomb interaction between carriers make the carrier multiplication process in NCs could be highly efficient[39].

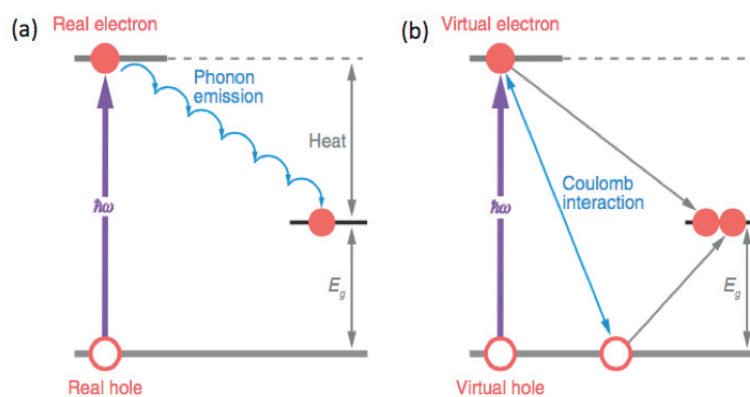


Figure 2.9 Schematic diagram of the carrier multiplication process. (a) Absorbing a photon with energy $< 2E_g$, the electron dissipate the energy as heat. (b) After the absorption of a single high-energy photon ($> 2E_g$), two excitons can be created through the Coulomb interaction in carrier multiplication processes[39].

Since the efficient carrier multiplication effect is of great significance for improving the photoelectric conversion efficiency of solar cells, photodetectors, etc., the CM in nanocrystals has received extensive attention. For traditional solar cells, since the excess energy is not effectively used, the maximum theoretical photoelectric conversion efficiency of a single-gap cell is about 33.7%, which is the Shockley-Queisser limit[54]. However, considering the carrier multiplication effect, the highest photoelectric

conversion efficiency is predicted to be as high as 44%[55]. In 2004, the V.I.Klimov research group first discovered the efficient carrier multiplication effect in PbSe nanocrystals using transient absorption spectroscopy[2]. Subsequently, highly efficient carrier multiplication effects have also been observed in a variety of nanocrystals, such as CdSe and perovskite CsPbI₃ NCs[56,57]. Multiexcitons created by carrier multiplication is the major content we investigate in this subject. Therefore, the brief introduction here will contribute to the understanding of following discussion section.

2.4 Scintillation process and scintillator

2.4.1 Scintillation process

X-ray is a kind of electromagnetic radiation with very short wavelength between ultraviolet and gamma rays, about $(20 \sim 0.06) \times 10^{-8}$ cm. It was discovered by the German physicist W.K. Roentgen in 1895, so it is also called Roentgen Ray[6].

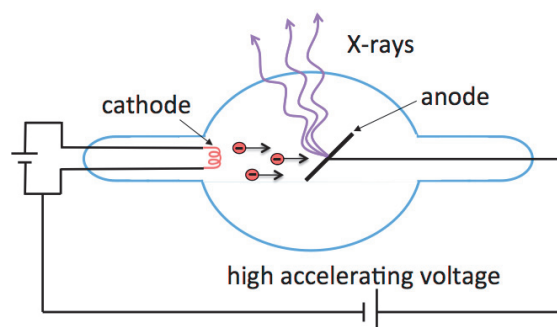


Figure 2.10 Schematic representation of X-rays tube

The device that generates X-rays is called an X-ray tube, which consists of three parts: cathode, anode and window, as shown in Figure 2.10. The two electrodes are used for the target material (such as W, Ag, Mo, Cu) bombarded by electrons and the filament (generally W wire) that emits electrons. Both electrodes are sealed in a high-vacuum glass or ceramic housing. The power supply part of the X-rays tube includes a low-voltage power supply for heating the filament and a high-voltage generator for applying high voltage to the two electrodes. When the filament passes enough current to generate an electron cloud, and there is enough voltage (kV) to be applied between the anode and the cathode, the electrons will hit the target material at high speed. When the high-speed electrons reach the target surface, the movement is suddenly blocked. The lost kinetic energy will be released in the form of photons to form a continuous part of the X-rays spectrum. The radiation generated in this form is called Bremsstrahlung. In addition, by increasing the acceleration voltage, the energy carried by the electrons increases, and it is possible to eject the inner electrons of the anode metal atoms. As a result, holes are formed in the inner layer, followed by the outer layer electrons transition back to the inner layer to fill the holes, and accompanied by emitting photons with a wavelength of about 0.1 nm. Since the energy released by the outer electron transition is quantized, it

forms a characteristic line in the X-rays spectrum, which is called Characteristic radiation. By adjusting the filament current, the temperature of the filament and the amount of electrons emitted can be changed, thereby changing the tube current and the X-rays photon flux. Different excitation potentials or different target materials can produce X-rays of different energies. Due to the bombardment of high-energy electrons, the temperature of the X-rays tube is very high during operation and forced cooling of the anode target is required. The approaches to detect X-rays and more generally ionizing radiation are divided into direct detection and indirect detection[58]. In direct detection X-rays are converted to electrical signals directly. Although this method is highly accurate, in many situations, these detectors are not easily applicable due to their cost and the required cryogenic application. So the indirect method is now more widely used. X-rays are first converted into a visible light, and this conversion is called as scintillation, which is followed by the conversion of light signals into electrical signals in photodetectors, as shown in Figure2.11.

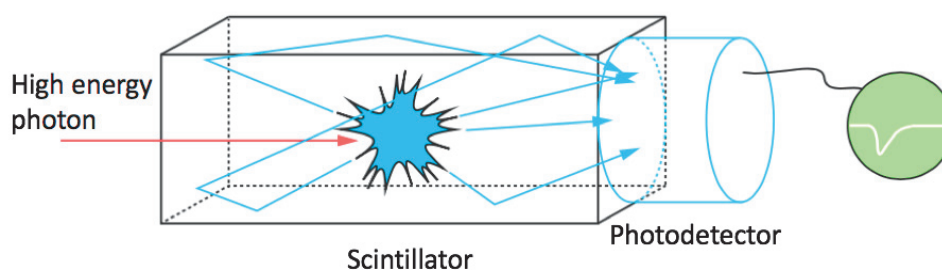


Figure 2.11 A simplified schematic representation of scintillation detector[60].

Scintillators are thus the materials that can convert high energy radiation such as X or gamma-rays into a visible light, and they play a very important role in the field of radiation detection, such as medical imaging, homeland security, high energy physics calorimetry and so on[7,59]. A scintillation detector essentially is composed of a scintillator material and a photodetector that can convert the outgoing light to an electrical signal. The scintillators can be generally categorized into organic scintillators and inorganic scintillators: organic scintillators comprise such as organic liquids and plastic scintillators, and inorganic scintillators typically consist of single crystals, powder or thin films of large band-gap salts matrix doped with activator atoms of appropriate energy states, such as NaI:Tl, CsI:Tl. Nowadays, inorganic scintillators are more widely used in numerous fields, and the novel inorganic scintillators with superb qualities are continuously investigated to satisfy the various applications.

The very first inorganic scintillator material NaI:Tl, was discovered in the late 1940s[60]. Despite the emergence of considerable new scintillator materials after that, NaI:Tl is still the first choice for many applications where cheaper, larger size, and higher efficiency scintillator is needed. However, it suffers from the common shortcomings of inorganic scintillator, long decay constants and hygroscopicity due to limitations in their intrinsic material properties and fabrication requirements. Since that time, a diversity of

scintillators has been reported for various applications. For instance, CsI:Tl is not hygroscopic with high light yield[61], but it shows the poor spectral match with PMT and extremely long decay time. On the other hand, Bi₄Ge₃O₁₂ (BGO) with higher stopping power, making it a very efficient absorber has been widely used in high-energy physics applications[62], but the light yield is much lower than that of NaI:Tl and CsI:Tl. The relatively new materials based on Ce³⁺ doping and Pr³⁺ doping possess the fast decay time (typically tens of ns) and high quantum efficiency[63]. But the high price due to raw materials and processing severely restricts their widespread usage.

Overall, each material possesses unique properties, the choice of scintillator materials depends on the practical application requirements. The most important characteristics considered for a scintillator selection are as follow[64]:

- *stopping power*: determines how efficiently a material will absorb the radiation during the conversion stage of scintillation. High stopping power means large fraction of the incident rays and particles can be deposited in the materials. As mentioned above, this parameter is strongly related to the density and effective atomic number of the scintillator, especially for the photoelectric interaction. Therefore, materials with high density and high Z are desirable.
- *light yield*: corresponds to the number of photons emitted per unit of deposited energy in the material. It is expressed in photons/MeV, is given by the relation: $LY = 10^6 \cdot SQ / (\beta E_g)$, where E_g is the bandgap, S is the efficiency of electron-hole transport to the optical center, Q is the luminescence quantum efficiency of the optical center and β is a constant. High light yield is very beneficial to reduce the noise in medical imaging.
- *response time*: corresponds to the time of emitting a photon after radiation absorption. Short decay time is very important for applications where fast timing is required such as time-of-flight applications.
- *radioluminescence spectrum*: it should well match the spectral sensitivity of the photodetectors.
- *energy resolution*: the ability of the scintillator to distinguish between different radiation energies. It is very important for the spectral measurement.

In addition, large scale production, chemical and radiation stability, self-absorption and cost are also key factors that determine the choice of a particular scintillator. Actually, the selection of scintillator is according to specific requirements and application fields. No scintillator can satisfy all the requirements for use.

The physical process of scintillation is a rather complex issue in inorganic scintillator, which can be divided into three consecutive sub-processes[64]: (I) conversion, (II) transport and (III) luminescence, as depicted in Figure 2.12.

In the first step, high energy photons interact primarily with materials through ionization events, followed by the creation of a large number of highly energetic electrons and holes formed in the material. The interaction of an electromagnetic

radiation with the matter occurs as three types depending upon the incident photon energy of the incident radiation in scintillation: photoelectric effect and Compton scattering are dominant mechanisms for low (below a few hundred keV) to medium energies (a few hundred keV-1MeV) respectively, and the interaction of the radiation with the matter is governed by the electron-positron pair creation for energies above 1.02 MeV[65]. In this thesis, we will focus mainly on detection of photons in the X-rays, involving the photoelectric effect and Compton scattering. The linear absorption coefficient of the photoelectric absorption for energy scales approximately with Z^4 . Hence, increasing the atomic number will increase the absorption probability exponentially, which is consistent with the need of heavy atoms in scintillator[66]. Afterwards, the hot electrons and deep holes that are created in this process will undergo the multiplication process through electron-electron inelastic scattering and Auger processes. When their energy is lower than the threshold, all the electrons and holes will be thermalized to the lowest states in the energy band.

In the transport process, electrons and holes in the conduction and valence bands are transported towards the luminescence centers, respectively. The undesired impurities and lattice defects during the fabrication of material will induce lots of traps in the forbidden gap. These traps compete to capture the migrating charge carriers, causing the considerable loss of excitons through the non-radiative recombination. In addition, the long delay is also the result of these intermediate states. After trapping, a certain thermal energy enables release of the charge from the shallow traps, and then these released carriers will continue to participate in the radiative recombination, resulting in considerable delay or afterglow. Optimization of fabrication and preparation procedures can significantly decrease the defects and traps within a material and improve the scintillating qualities.

In the last step, the electrons and holes are captured by the luminescence centers, and then undergo a recombination process, giving rise to a desired luminescence light. In some particular groups of materials the light generation occurs in radiative transitions between the valence and first core bands[64].

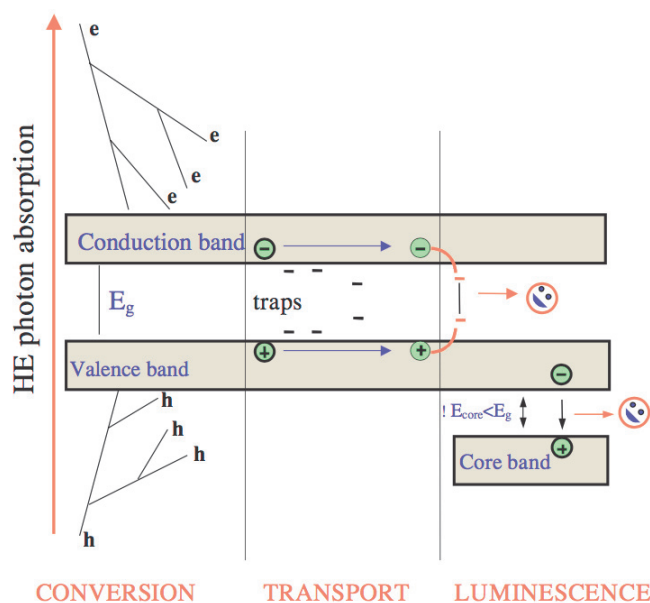


Figure 2.12 Schematic representation of scintillation mechanism in bulk inorganic scintillators. High energy photons absorbed can generate hot charge carriers, followed by thermalization to form a great amount of excitons and subsequent transport to traps involved intermediate states or luminescence centers, where radiative recombination occurs[64].

2.4.2 Nanocrystals scintillator

In recent years, the increasing demand for radiation detection materials in many applications has led to extensive research on scintillators. The discovery of new scintillators has always been an important subject. Nanocrystals have received extensive attention due to their excellent optical properties[7]. Unlike the traditional bulk scintillators, the output wavelength of nanocrystals can be tuned to span the visible light emission such that it can well match with the peak spectral sensitivity of the photomultiplier tube to improve the overall detection efficiency. Furthermore, the solution-processability and practical scalability can also reduce the manufacturing cost and difficulty, making it a promising material for radiation detection. In the past two decades, the response of a large number of nanocrystals under high-energy electrons, alpha particles, X-rays and gamma rays has been widely studied.

In 2006, S.E. Letant and T.F. Wang for the first time reported the characterization of CdSe/ZnS core/shell NCs in porous glass matrix under α particle and gamma-rays radiations. They demonstrated that the scintillation efficiency of the CdSe/ZnS NCs is two times better than that of the conventional NaI:Tl scintillator[8,67]. This strongly suggests that higher efficiencies and resolutions are possible with nanocrystal-based scintillators, and motivated the further research on the scintillator materials in the form of nanocrystals.

The relatively low stopping power is one of the shortcomings of II-VI nanocrystals, leading to a weak scintillation luminescence, hence the combination of a matrix with high stopping power and nanocrystals has been usually used to investigate their potential to be a new class of scintillator. Several research have been reported to fabricate NCs embedded nanocomposite scintillators, the improving of energy efficiency has been achieved *via* energy transfer mechanisms between matrix and NCs. The chosen NCs materials should well match the emission spectral region of the matrix. The high stopping power of the matrix can compensate low energy absorption of NCs. Mingzhen Yao and Marius Hossu integrated CdTe NCs with LaF₃:Ce nanoparticles and observed the enhanced NCs fluorescence upon both UV and X-rays excitation[9,68]. In addition, the NCs–polymer was also fabricated to investigate the scintillation behavior. CdTe NCs was embedded into polyvinyl alcohol matrix, together with the 2,5-diphenyl oxazole (PPO) as exciton harvesting[69], and the addition of CdS NCs in polyvinyl toluene (PVT)-PPO polymer enhanced scintillation from a 1.03 times to more than 3.6 compared to using PVT-PPO without any NCs[70]. However, the intensity of the scintillation light scales with the NCs concentration. High concentration usually induces strong reabsorption and the scattering due to agglomeration. And this type of NCs–polymer hybrids were also designed for gamma-ray sensor, significant enhancement in photoconductivity induced by the gamma radiation in nanocomposite has been demonstrated[71].

Environmentally friendly nanocrystals are always the development trend of nanotechnology, to be scintillator, it will be beneficial to decrease the damage to human tissues, facilitating the practical application in medical imaging. ZnS NCs doped with magnesium sulfide, ZnS(MgS) was studied by E. R. Burke, showing good proportionality and high sensitivity of X-rays[72]. In 2018, Eder Jose Guidelli *et al.* synthesized ZnSe NCs using a microfluidic reactor with uniform sizes and excellent optical properties. They reported the radioluminescence from ZnSe cores under X-rays excitation, revealing the possibility to be a low-toxic scintillator[73]. However, due to the low mass density and effective atomic number of Zn-based NCs, their absorption of high-energy rays is very low, which severely limits the scintillating performance.

Photo-instability is one of the key issues of semiconductor nanocrystals, which severely degrade the performance of scintillation. Several studies reported the optical response of NCs to high energy photons, a rapid loss of output light was observed when the NCs was exposed under X-rays or γ -rays[74,75]. Afterwards, Girija Gaur *et al.* reported the significantly reduced emission intensity with CdTe/CdS QDs immobilized within porous silica under ionizing irradiation[75]. They also pointed that photoionization, carrier traps, and Auger recombination play a role in the radiation-induced photodarkening. Through a thiol-rich surface re-passivation, near complete recovery of X-rays induced emission intensity was achieved, but only partial luminescence recovery was observed for gamma-irradiated samples, which is the result of permanent reduction caused by lattice displacements in the NCs. In 2016, Marie-Eve Delage *et al.* demonstrated multishell QDs are more resistant to ionizing radiation than core/shell QDs, especially in the kV energy range, further confirming the importance of the surface passivation[76].

In addition to the traditional spherical quantum dots with different compositions, nanocrystals of different shapes have also received extensive attention. The first successful synthesis of a two-dimensional II-VI CdSe nanoplatelets(NPLs) was in 2008[77]. Due to its fascinating properties, it has recently been explored in the field of radiation detection[10,78]. In 2019, Turtos R. M. *et al.* constructed hybrid NCs-bulk scintillators structure to measure the scintillation response for 511 keV gamma-rays[10]. A thin film of CdSe/CdS core/crown NPLs was deposited on standard LYSO bulk scintillator, in which NPLs is in charge of fast time response while the bulk scintillator provides stopping power and scintillation light. Ultrafast decay of 80ps associated to multiexcitons has been extracted as the preliminary result, providing a strong impetus for future in-depth research.

The novel nanostructure in the form of perovskite nanocrystals has emerged to be a promising scintillation material in recent years. It shows remarkable performance as scintillator benefit from high stopping power and defect tolerance for high quantum yield[11,79]. In 2018, Chen *et al.* proved 3D perovskite CsPbBr₃ nanocrystals has high fluorescence efficiency under X-rays excitation. The emission wavelength can be easily tuned across the visible light by tailoring the anionic component. In addition, the intense radioluminescence decreases significantly the detectable limitation of the X-rays dose, reducing the damage to human tissues caused by radiation[11]. Furthermore, the solution-processability and practical scalability make them suitable for the mass scale production. However, the inherent thermal and chemical instability and the heavy metal toxicity are the obstacle for this type perovskite nanocrystals in practical applications.

Although a variety of nanomaterials are active in the field of radiation detection, the process of energy deposition and relaxation in semiconductor nanocrystals is still ambiguous and few reported so far. As discussed above, the incidence of high-energy photons yields a predictable cascade of energetic electrons, since the absence of transport process in direct gap nanocrystals semiconductor, the hot electrons and holes are directly thermalized towards the conduction and valence band edges. Unlike bulk materials, nanocrystals behave as discrete energy levels related to quantum confinement, making the excitonic species unknown after the hot carriers ultimately relax to the edge of the energy band.

For the energy deposition, in 2010, Anne-Laure Bulin *et al.* used Monte Carlo simulations to numerically estimate the spatial energy distribution resulting from the interaction between the gamma-rays photons and the Gd₂O₃ nanocrystals. They demonstrated that a significant fraction of the energy is deposited out of the particle, even for the diameter larger than 100nm[80]. To date, there is no direct study on unexamined steps in energy relaxation down to energy band states within a NCs excited by X-rays after the initial electron shower. Instead, the Lazaro A. Padilha research group[14] has compared the temporally and spectrally resolved radiative recombination produced following photoexcitation with 20keV energetic electrons ionizing radiation, identifying and quantifying the types of excitation states produced in NCs under high energy excitation. The analysis directly reveals a dominant population of charged- and multi-

excitonic states, consistent with large contributions from carrier multiplication, multiple types of scattering and ionization processes during relaxation. They also pointed out that the Auger effect is a key factor restricting the study of excited states under ionizing radiation. The investigation of cathodoluminescence can provide guidance for the exploration of X-rays-induced exciton recombination. In our work, thanks to the development of chemical synthesis techniques, the reduction of Auger effect gives us a good opportunity to realize the fine observation and identification of multiexcitons states under X-rays excitation in nanocrystals.

2.5 Spherical quantum wells and nanoplatelets

2.5.1 Spherical quantum wells introduction

Despite the apparent promise of thick-shell NCs on both Auger recombination suppression and enhanced absorption cross-section, however, the thickness of the shell is not allowed to increase indefinitely. The intrinsic reason is the difference in lattice constants between the two materials of the core and shell, namely, with the increase in the thickness, the structural stress on the interface will continue to increase. When the thickness of the shell reaches a critical value, the further growth will introduce structural defects into the nanostructures, and these defects will capture carriers like surface traps, resulting in a serious decrease in the fluorescence efficiency of the NCs. In the commonly used synthetic materials of core/shell nanocrystals, the lattice parameter mismatch between CdSe and ZnS reaches 12%, such a huge amount of misfits make them not suitable choices even for traditional thick-shell NCs. The better candidates for the synthesis of thick-shell NCs should be CdSe and CdS because of the well energy band alignment and the only 4% lattice mismatch between two materials. However, according to the calculation of the critical thickness, when the CdSe layer grown on top of the CdS core exceeds around 3.6nm[81], the quantum yield will drastically reduce due to the formation of misfit defects.

In order to solve this limitation, spherical quantum wells(SQWs) are considered as an alternative structure. It combines the excellent characteristics from both nanoplatelets and regular core/shell nanostructures. The first SQWs synthesized through successive ion layer absorption and reaction (SILAR) was reported by Peng's group, ultrathin layer of semiconductors with a narrow bandgap, epitaxially grown onto a nanocrystal template with a substantially wider bandgap[82]. Since the emissive layer is thinner than the critical thickness, it enables the alleviation of structural stress between two materials by strained layer epitaxial growth. SQWs are considered as an optimal model to create large nanoparticles with a less defect growth. In addition, the thick shell layer ensures the stability and reduces the probability of the SQWs being charged by reducing the possibility of carriers being trapped by the surface traps. Therefore, it could achieve the significantly enhancement of quantum yield compared to the traditional NCs. In 2016, Jeong *et al.* synthesized CdS/CdSe/CdS SQWs through dropwise precursor method with near unity quantum yield[81]. On the contrary to the NCs, the quantum yield of SQWs show a continuous enhancement with increasing shell thickness.

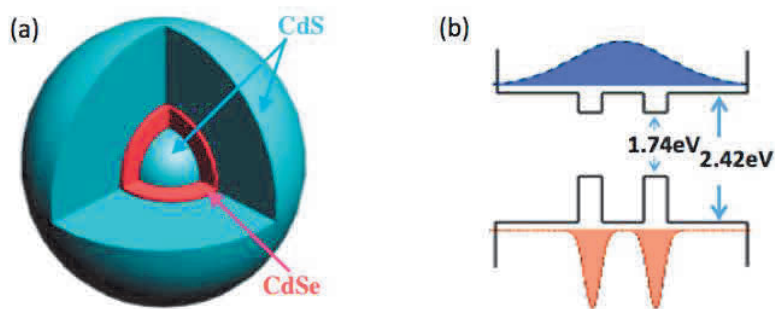


Figure 2.13 (a) Schematic illustration of spherical quantum wells; (b) Quasi type II energy band alignment of spherical quantum wells.

As the best investigated configuration, CdS/CdSe/CdS SQWs comprise three layers: a thin CdSe layer sandwiched between a CdS core and several layers of CdS overcoating, as depicted in Figure 2.13(a). The electronic properties exhibit the strongly core, well and shell thickness dependence. Specifically, SQWs were also reported to possess a quasi-type-II band alignment (Figure 2.13(b)), in which a hole is strongly localized within the CdSe well, whereas an electron is delocalized over the entire nanostructure volume. The electron confinement energy reduces with increasing exterior CdS shell thickness, resulting in the red shift of the absorption and the PL peak position[81], as shown in Figure 2.14(a). And the same tendency of energy shift was observed for different core and well sized SQWs[83]. Meanwhile, the decrease in the electron–hole overlap integral with increasing CdS shell thickness results in a progressive reduction of the single-exciton recombination rate (Figure 2.14(b)).

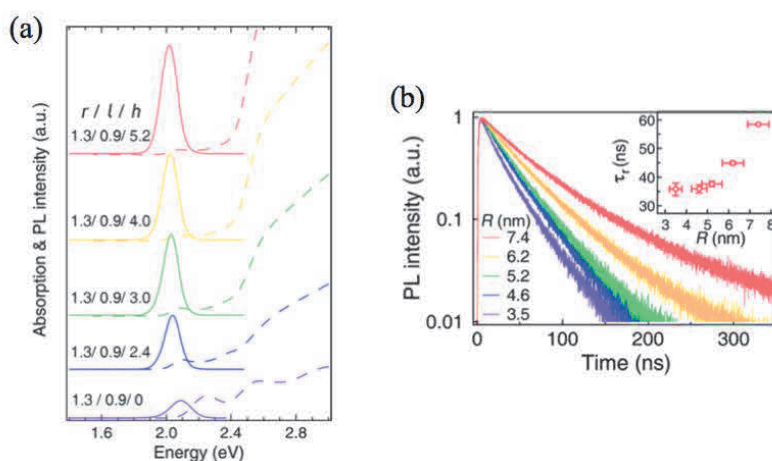


Figure 2.14 (a) Absorption and photoluminescence spectra of different shell thickness SQWs (r : CdS core; l : CdSe well; h : CdS shell), (b) The evolution of ensemble PL decay dynamics with shell thickness (inset: single-exciton radiative recombination lifetime; R is the total size)[81].

In 2020, Gabriel Nagamine *et al.* presented that SQWs enable a relatively large absorption cross-section without the quantum yield loss, the quantum yield of SQWs about 40% larger than counterpart QDs with the same absorption cross-section[84]. Since absorption cross-section is proportional to the volume of nanocrystals, the predicted large absorption cross section in SQWs is attributed to that its volume could far exceed that of traditional QDs. This promising property is beneficial for tremendous research application, achieving the low threshold amplified spontaneous emission and lasing, reducing the working current when applied to electroluminescent devices and reducing the damage to the tissue when they are used in biological imaging[4,84].

In addition, another remarkable property of SQWs is the suppression of Auger non-radiative recombination, leading to the long multiexcitons lifetime. Analogous to QDs, biexciton lifetime depends strongly on the shell dimension, which can be attributed to the increase in the delocalization of the electron and hole wave functions. Till now, the biexciton lifetime of SQWs was demonstrated on the order of nanosecond[84,85]. Meanwhile, as mentioned above, biexciton binding energy is determined by exciton-exciton Coulomb interaction. Through modifying the ratio of different regions, one can manipulate the sign and magnitude of biexciton binding energy in SQWs, the transition from attractive to repulsive force was observed[84].

Owing to the thick shell, SQWs usually exhibit outstanding optical and chemical stability. By applying silica encapsulation *via* reverse micro-emulsion method, the stability of SQWs can be further improved, and it can be dissolved in polar solvents, which is convenient for bio-labeling or display applications[86]. To date, due to the large absorption cross section and the Auger effect suppression, the research of SQWs mostly focused on the optical gain media and light emitting diodes[84,87]. In this thesis, motivated by the fascinating properties, we will utilize this structure to investigate the scintillation behavior of nanocrystals on a large-scale (up to 40nm in diameter) under X-rays excitation, this will give an insight to the exciton recombination mechanism under extremely energetic excitation.

2.5.2 Nanoplatelets introduction

As mentioned earlier, with the development of nanocrystalline synthesis methods, nanomaterials of different structures have been realized. In 2008, S. Ithurria successfully synthesized two-dimensional CdSe nanoplatelets for the first time[77]. Subsequently, nanoplatelets with different composition have also been successfully fabricated[5,88]. Their outstanding optical and electronic properties have attracted widespread attention. Different than other classes of NCs, generally these colloidal NPLs feature lateral dimensions on the order of tens of nanometers with the atomic-scale vertical thickness, while the 2D Bohr radius of the CdSe NPLs is considered to be around 3.5nm[89], leading to the strong quantum confinement effect in only one dimension. By changing the synthesis reaction parameters, atomically precise control of the vertical thickness can be achieved.

The width of the fluorescence spectrum is composed of two factors: homogeneous broadening and inhomogeneous broadening. The coupling of photons and phonons will lead to homogeneous broadening of the spectral lines, but the inhomogeneous broadening is determined by the size distribution of the synthesized nanocrystals. High monodispersity of NPLs allows to eliminate the inhomogeneous broadening, and they thus exhibit purely homogeneous broadening. This results in a very sharp PL profile with a full-width-at-half-maximum (FWHM) typically narrower than 10 nm. In addition, NPLs possess giant oscillator strengths resulting from increased exciton center of mass coherent motion[90]. This huge oscillator strength enables significantly enhanced absorption cross-section and ultrafast recombination rate.

Controlling the number of monolayers (ML) significantly affects the absorption and photoluminescence spectra of the NPLs. Due to the emission wavelength of CdSe NPLs is only determined by the thickness, it generally has fixed emission wavelengths. Figure 2.15 shows the spectra of several CdSe NPLs with different thicknesses, 3 ML, 4 ML and 5 ML, which have been commonly investigated for almost a decade, emitting at around 463 nm, 513nm, and 553 nm. The quantum confinement is relaxed with the increasing thickness, causing a red shift of the excitonic features. For 4ML NPLs, three typical features are observed on the absorption spectrum, they correspond to the heavy-hole(~ 512 nm), light-hole(~ 480 nm) and split off transitions (~ 420 nm). The excitonic features remain almost in the same spectral position regardless of the lateral dimensions because they are much larger than the exciton Bohr radius. When the thickness of the CdSe NPLs is as thin as 3ML, the surface defects will lead to intensive emission. The strong surface related deep trap photoluminescence emission is more obvious in thinner NPLs, which is attributed to the unpassivated atoms at the surface[77].

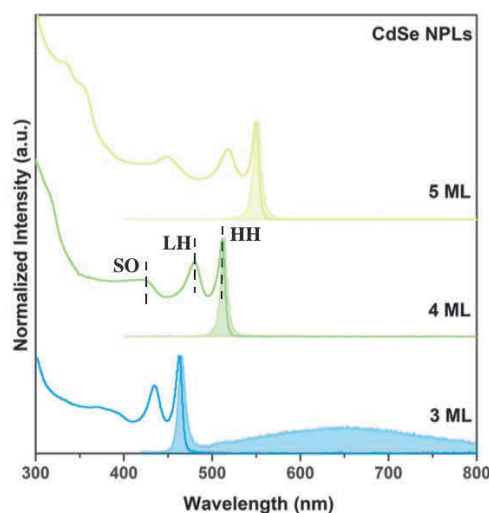


Figure 2.15 Absorption and photoluminescence spectra of CdSe colloidal NPLs with different vertical thicknesses[91].

However, bare core NPLs usually suffer from low quantum yield and poor stability, which seriously affect the practical application of NPLs. Therefore, in order to increase quantum yield, improve optical and chemical stability, and achieve a wider spectral coverage, a diversity of NPLs-based heterostructures have been produced in the past decade, for example core/crown, core/shell and core/crown/shell as illustrated in Figure 2.16, making these two-dimensional materials have made great progress in many applications.

The most widely studied CdSe/CdS core/crown heterostructure has been synthesized by M. D. Tessier and coworkers in 2014[92]. The CdS crown region was grown only in the lateral direction without changing the vertical thicknesses of the NPLs. Since the quantum confinement of the core is retained, the growth of the crown does not affect the excitonic features of the NPLs. The growth of laterally extended crown is manifested as an absorption peak at around 405 nm, leading to a strongly increase in the absorption cross section. Owing to the lateral passivation, the core/crown has been reported with the significant improvement of quantum yield. In addition, the core/crown structure NPLs with different compositions has also received extensive attention, such as type II CdSe/CdTe, alloyed CdSe/CdSeTe[93,94].

In addition to core/crown, inspired by core/shell QDs structure, the low quantum yield and poor stability of NPLs are expected to be improved by coating a shell on the core NPLs. The growth of shell in the vertical thicknesses will induce the relaxation of the quantum confinement effect, making the red shift of excitonic features. Therefore, by controlling the shell thickness, the optical properties can be easily manipulated. Meanwhile, due to the enhanced exciton-phonon coupling with these material combinations, the excitonic features are slightly broadened with respect to core-only NPLs, as shown in Figure 2.16(b). In recent years, different composition core/shell NPLs has been fabricated by different synthetic methods[95,96], in which alloys and/or gradient complex heterostructures have been demonstrated the near-unity quantum yield. Moreover, owing to the partial separation of electron and hole wavefunctions and the smooth confinement potential, Auger recombination has been significantly suppressed in this heterostructure.

In addition, more complex core/crown/shell structures have also been employed in the several researches[97,98]. They pointed out that when compared to core/shell NPLs, core/crown/shell NPLs exhibit significantly enhanced absorption cross-section in the blue spectral region owing to crown layer and improved brightness due to better passivation of the sidewalls of the inner core. So far, the hot injection method for this architecture has still not been reported. The synthesis based on c-ALD technique usually causes low QY, only Shendre *et al.* presented ultrahigh-efficiency aqueous colloidal core/ crown/alloyed-shell quantum wells with QY up to 90% in water[98].

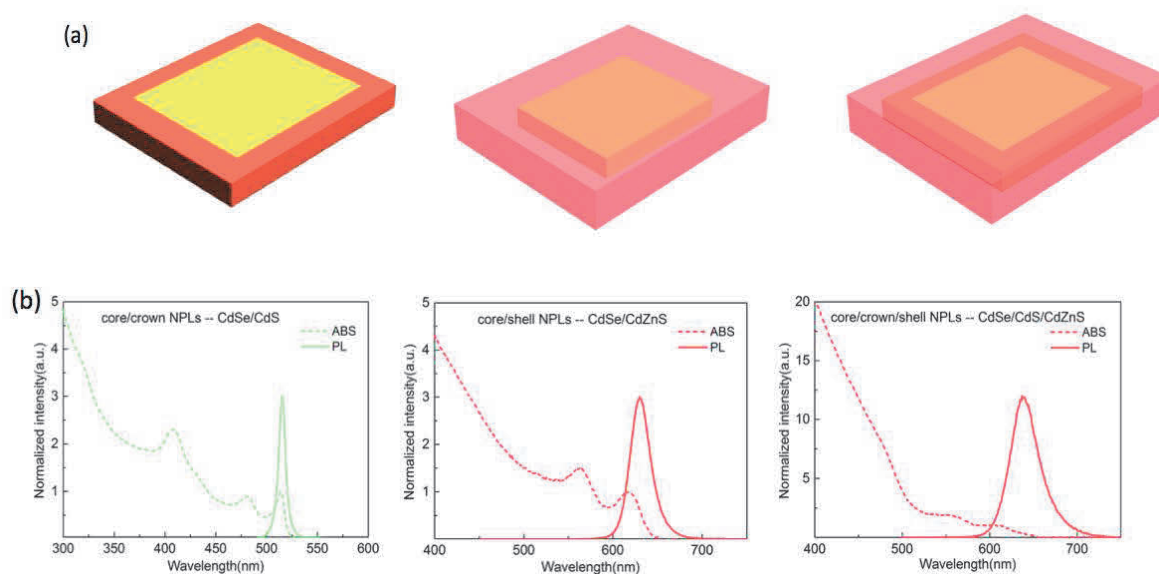


Figure 2.16 (a) Schematic illustration of core/crown, core/shell and core/crown/shell heterostructures. (b) Absorption and photoluminescence spectra of CdSe/CdS core/crown, CdSe/CdZnS core/shell and CdSe/CdS/CdZnS core/crown/shell NPLs, all of which are synthesized at our laboratories.

Even though NPLs can be synthesized by well-controlled synthesis procedures and their excellent properties have received considerable attention, there are still controversies about the growth mechanism of the two-dimensional structure. Since the first synthesis of CdSe was due to the addition of short-chain salts in the reaction solution[77], short-chain ligands were regarded as the key factor in the lateral growth of nanocrystals from the beginning. Long-chain and short-chain ligands (such as oleate and acetate salts) passivated the large and small cadmium-rich surfaces of NPLs, respectively. The long-chain ligand stabilizes the large facet, while the short-chain ligand makes the small facet more unstable, allowing the NPLs to grow laterally and maintain a constant thickness. Lately, Riedinger *et al.* synthesized CdSe NPLs in melts without the presence of short-chain carboxylate ligands, they pointed out that the addition of short-chain carboxylates is critical only in standard liquid-phase protocols, leading to the reduction of monomer concentration, and the solubility of the monomer affects the shape of the crystals. Meanwhile, they proposed a theory, regarding the growth mechanism of zinc blend CdSe NPLs, based on an intrinsic instability in growth kinetics leading to highly anisotropic shapes[99]. The nucleation barriers on narrow facets are smaller than on wide facets, therefore, the growth rates on lateral and vertical dimensions are orders of magnitude difference, yielding the anisotropic-shaped NPLs even for materials with isotropic crystal structures. On the other hand, Peng's group[100] has suggested a different mechanism based on the oriented attachment of seeds through intraparticle ripening.

Chapter 3

Colloidal Synthesis and Characterization of Spherical Quantum Wells and Nanoplatelets

The fascinating properties of nanocrystals have received worldwide attention. Thanks to the continuous development of the colloid synthetic approach, nanocrystals of different sizes, shapes, and compositions have been successfully synthesized in the past decade[101], and the optical and electronic properties of nanocrystals have been significantly improved. Meanwhile, in comparison with bare core, the emergence of heterostructures with higher stability and quantum yield provides better opportunities for their applications in various fields[22,26].

Therefore, this chapter is mainly divided into four parts, we will first present the synthesis theory and setup for core and the core/shell structures. Secondly, the optical and structural characterization techniques used in this thesis are briefly introduced. The last two parts are about the specific synthesis protocols and characterization of nanocrystals, including spherical quantum wells(SQWs) and different heterostructural nanoplatelets (NPLs), core/crown, core/shell and core/crown/shell.

3.1 Synthesis theory and setup

3.1.1 Nanocrystals nucleation and growth

Since the emergence of quantum dots, many efforts have been put in the understanding of the formation mechanisms of mono-disperse nanocrystals. This progressive comprehension makes it possible to achieve syntheses of nanocrystals with controllable size, shape, and composition, in which the thermal decomposition is the most successful nanocrystals preparations in terms of quality and monodispersity[16]. The involved nucleation and growth are presented in the following sub-section.

3.1.1.1 Gibbs -Thompson theory

Homogeneous nucleation is a phase change process that is the spontaneous formation of a new thermodynamic phase from a meta-stability state[102]. Thus, in contrast to heterogeneous nucleation, the occurrence of homogeneous nucleation needs to overcome higher energy barriers. The thermodynamic theory of formation of the new phase is classical Gibbs-Thompson theory, as shown in Figure 3.1.

The Gibbs free energy of a nucleus is in general expressed as the sum of a bulk term ΔG_1 that is proportional to the volume of the nucleus, and a surface term ΔG_2 , that is proportional to its surface area. We assume that the nucleus is spherical in shape with radius r , hence, total Gibbs free energy is given as equation 3-1,

$$\Delta G_T = \Delta G_1 + \Delta G_2 = \frac{4}{3}\pi r^3 \cdot \Delta G_v + 4\pi r^2 \cdot \gamma \quad (3-1)$$

where γ is the surface energy per unit area and ΔG_v is the free energy per unit volume in the bulk. The volume term is negative which is the driving force for nucleus formation. And the surface term has a positive contribution due to the creation of a solid and liquid interface.

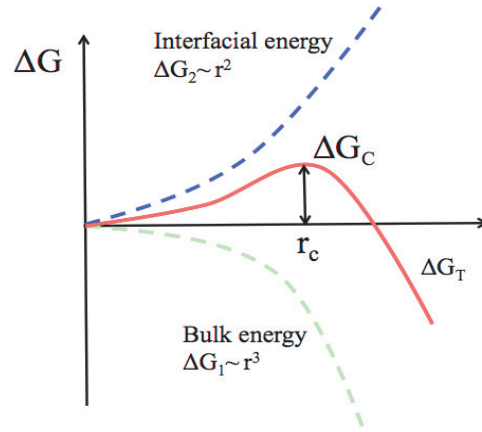


Figure 3.1 Red curve is the total Gibbs free energy as a function of the nuclei radius. ΔG_c is the homogeneous nucleation energy barrier, and r_c is the critical radius. The bulk term ΔG_1 that scales with r^3 is plotted in green. The interfacial energy ΔG_2 is the blue curve that is proportional to surface area.

From the total Gibbs energy curve, we can see that the minimum radius of formed nucleus is r_c , which is referred as critical size. The nucleus smaller than r_c will dissolve into the solution, and the nucleus larger than r_c can exist for further growth. The critical size is reached when free energy ΔG gets to a maximum, which is:

$$d\Delta G/dr=0 \quad (3-2)$$

Simplifying the above result, we can derive that

$$r_c = -\frac{2\gamma}{\Delta G_v} \quad (3-3)$$

$$\Delta G_c = 16\pi\gamma/3(\Delta G_v)^2 \quad (3-4)$$

3.1.1.2 Lamer burst nucleation theory

Burst nucleation theory was proposed by Lamer and co-workers in 1950s[103]. Originally Lamer theory described the production of mono-dispersed sulfur brines. The model is used today for growth of most diverse nanoparticles. It is based on homogeneous nucleation theory, and separates the nucleation process and growth process. Nuclei are generated at the same time and subsequently grow without additional nucleation. Thus, the crystallization of the nanoparticles is complete and the particle size distribution is more uniform.

Figure 3.2 schematically illustrated the processes of nucleation and subsequent growth. Typically nanoparticles are synthesized in three stages[102]. The concentration of monomer increases with time in stage I, no nucleation would occur even above the equilibrium solubility because of the extremely high energy barrier for homogeneous nucleation. The nucleation stage II appears only when the super-saturation reaches the critical nucleation threshold, thereby overcoming the energy barrier, which corresponds to the free energy defined by equation 3-4. While as the formation of nuclei, the concentration of monomer decreases until the critical energy, nucleation stage ends and the reaction enter into growth stage until the concentration of monomer reaches the equilibrium solubility. Lamer theoretical mechanism diagram is shown below.

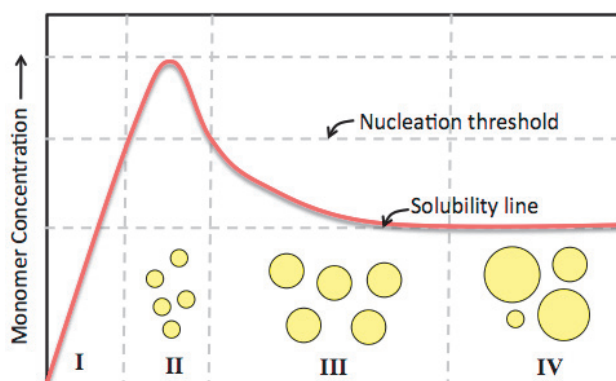


Figure 3.2 Schematic illustration of the nucleation and subsequent growth process.

However, if we do not stop the reaction at a reasonable time, the further growth of nanoparticles occurs in stage IV due to Ostwald ripening, in which large particles compete with smaller ones. Large nanoparticles are thermodynamically favorable, and they will be continuously growing owing to the dissolution of smaller particles[104]. Hence, poly-dispersed samples are often attributed to Ostwald ripening process.

According to the discussion above, reaction factors have significant influence on the quality of synthesized samples. First, the temperature plays a key role during the synthesis, high temperature is required to form the nuclei, however the size and shape of nanocrystals are less controllable in this case, and temperature also determines the

reactivity of the precursors. Therefore, a suitable temperature is extremely important for the precise control of nanocrystals. Second, if the precursor is introduced into the reaction by injection, the rate of injection is another key parameter to adjust the synthesis. The size distribution of nanocrystals can be controlled by fast or slow injection. Fast injection introduces the abrupt increase of the monomer to reach a very high super-saturation, leading to a narrow size distribution of nanocrystals in a very short period of time[103]. In addition, an appropriate annealing time after growth stage enables minimize the influence of Ostwald ripening on size dispersion.

3.1.1.3 Nanocrystals synthesis setup and method

The chemical synthesis reaction usually takes place in a three-neck round-bottom flask as illustrated in Figure 3.3. One neck of the flask is connected with a reflux condenser to limit the evaporation of the solvent during heating, one with a rubber septum through which precursor could be injected or products removed, and the third with a temperature probe. The flask is maintained under an inert gas atmosphere (argon) and heated by a heating mantle. All the chemicals in the flask need to be degassed in order to achieve water and oxygen free conditions. And stirring during the reaction can make precursors mixed efficiently and avoid the aggregation of the nanocrystals.

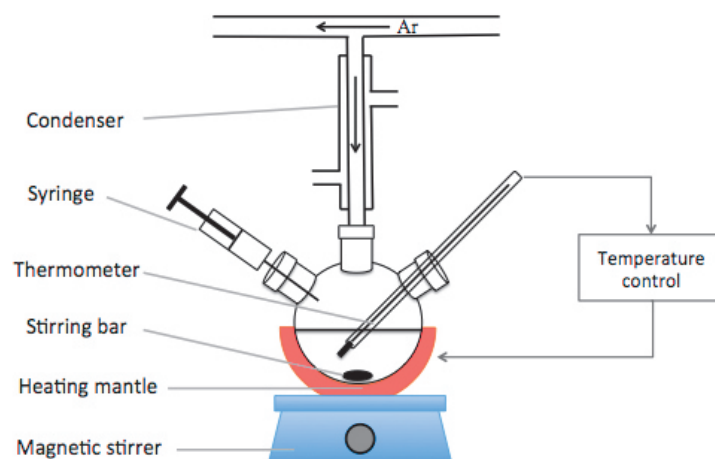


Figure 3.3 Schematic of three neck flask apparatus for nanocrystals synthesis.

As mentioned above, the mono-disperse nanocrystals synthetic strategies have been investigated since quantum dots were proposed[105,106]. To date, the thermal decomposition is the most effective and successful method for high quality nanocrystals synthesis. This method can be divided into two techniques: hot-injection and non-injection. The hot-injection method was introduced by Bawendi and co-workers on the synthesis of cadmium chalcogenide nanocrystals[1]. Sharp burst nucleation occurs due to the rapid injection of precursor into hot solution, including solvent and surfactants. Thus, hot-injection enables the production of narrower size dispersion nanocrystals. However, it is difficult to scale up the synthesis in large quantities. Alternatively, the development of

non-injection method addressed this problem, in which the precursors, solvent and surfactants are mixed in the flask at a low temperature, and then heated up to the nucleation temperature. In order to achieve the formation of mono-sized nanocrystals, refraining from the concurrent nucleation and growth, the precursor choice and the setting of reaction temperature are extremely important during this gradually raising temperature process[107]

3.1.2 Core/shell structure synthesis

Core/shell nanocrystals research has been one of the hot topics in recent decades. On the one hand, the core/shell structure can effectively eliminate the dangling defects on the surface of the bare core, reduce non-radiative transitions, and improve luminous performance. On the other hand, the core/shell structure composed of semiconductor nanocrystals with different properties has new functions and important application prospects in many fields.

The core/shell structure was synthesized for the first time in 1996, Guyot-Sionnest *et al.* successfully covered a ZnS shell on the core CdSe, achieving the enhancement of quantum yield and stability[108]. Since then, two approaches were developed to synthesize core/shell structures. The SILAR (successive ion layer absorption and reaction) method based on the formation of one monolayer at a time by alternately injecting the anion and cation shell precursors. This method successfully solved the problem of self-nucleation of the shell precursor. In 2003, *via* SILAR, Peng's research group successfully synthesized up to 5 monolayers CdS shell on 3.5nm core CdSe with narrow PL line widths in the range of 23–26nm[109]. However, the SILAR method is a very time-consuming procedure, which is not conducive to the formation of thick shells.

Alternatively, the other method is dropwise, that is continuous injection of shell precursors at the same time into the flask containing the core. This requires a good control of the temperature and the slow rate of injection to avoid secondary nucleation of shell material. If the injection rate is too slow, it will lead to Ostwald ripening of the core. The amount of precursors can also be calculated to predict the final size of the nanocrystals. In comparison to the SILAR method, the continuous injection is much faster, but usually results in relatively less monodisperse samples[110]. In our thesis, the aim is to prepare the particle with ultra-thick shell. In order to simultaneously satisfies the criteria: time-saving and high uniformity, we utilize the continuous injection method and meanwhile using the precursors with relatively low reaction rate to achieve a well-maintained particle size distribution during shell growth.

3.2 Optical and structural characterization techniques

To study the rationality of the synthetic method, different characterization techniques are needed to collect sufficient information on the synthesized nanocrystals, such as the size, shape, composition and the excitonic features. The investigation of the quality of the synthesized nanocrystals can give a guideline to improve the synthesis and

the development of a new protocol. In this thesis, the structural techniques used are transmission electron microscopy (TEM), and the optical techniques include absorption spectroscopy (ABS), photoluminescence spectroscopy (PL), photoluminescence excitation spectroscopy (PLE).

3.2.1 Absorption spectrum

Absorption spectroscopy is a powerful technique to determine the absorption behavior of the synthesized nanocrystals, reflecting the size and composition of the sample. In an absorption spectrum, quantum confinement effect is well manifested as the red shift of the excitonic peaks as nanocrystal size increases, which corresponds to the decreasing energy band, as shown in Figure 3.4. And then the bulk behavior appears in large particles. Therefore, we can determine nanocrystals size from the position of first excitonic peak [111]. In addition, the different excitonic peaks in spectrum reveal the optical transitions between the discrete energy levels due to quantum confinement effect. The main absorption peak ($1S_{3/2}(h) \rightarrow 1S_{1/2}(e)$) exhibits a large oscillator strength, leading to a clear feature. And less pronounced absorption features in the shorter wavelength range correspond to excited states of higher energy, where the energy levels behave as a quasi-continuum [112]. The width of these peaks is strongly affected by the size distribution of the nanocrystals dispersion, polydisperse samples induce an inhomogeneous broadening of the excitonic features.

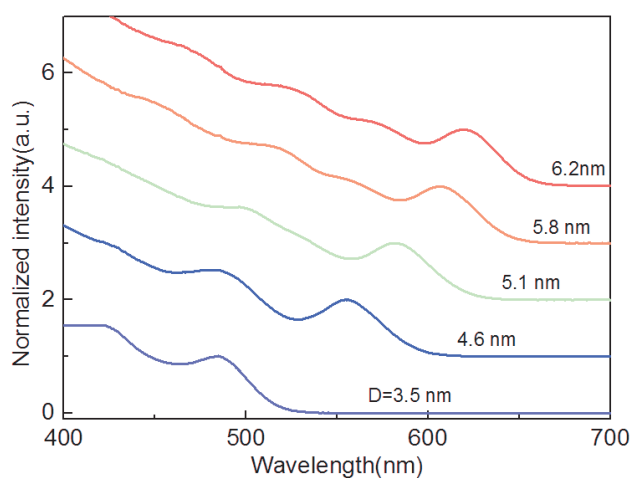


Figure 3.4 Evolution of the absorption spectra with increasing size of CdS/CdSe quantum dots, which are synthesized in our laboratory. Size is calculated by the precursors used

3.2.2 Photoluminescence spectrum

Photoluminescence (PL) is the property of a material to emit light after excitation by absorbing photons. In semiconductors, absorbing photons with an energy superior to its band gap can excite the electron to the conduction band, leading to the formation of exciton. The radiative recombination of exciton leads to the light emission. The emitted photons have an energy corresponding to the band gap of the semiconductor. Therefore,

PL spectrum is usually utilized to follow the evolution of semiconductor nanocrystals growth during the synthesis. Both dispersion solution sample and solid film sample can be used in this measurement. Similar to absorption spectrum, the size-dependent emission color is associated with quantum confinement effect. As illustrated in Figure 3.5, by changing the size of CdS/CdSe quantum dots, the emission spectra can be tuned to span the whole visible light range. Furthermore, the position of the emission peak corresponds to the band-edge energy, and the width of the PL spectrum is characterized by FWHM. The FWHM of the peak can also give us the information about the size distribution of samples[113]. It should be noted here that the defects on II-VI nanocrystals surface usually induce a trap energy level in the forbidden band, therefore trapped carriers emission take place on the longer wavelength than band edge emission. Proper surface passivation is necessary to get rid of these trap states, otherwise the fluorescence spectra can be strongly impacted by the trap emission, as depicted in Figure 3.5.

Typically, the emission peak is red-shifted compared to the corresponding excitonic feature in the absorption spectrum. This phenomenon is usually referred to as Stokes-shift, and this shift originates from the fine structure of the exciton energy levels. The self-absorption caused by a small Stokes-shift is one of the reasons for poor performance on lasing media, scintillator and others application where high concentrations of nanocrystals are needed[114,115]. Therefore, an enlarged Stoke-shift can be required to reduce self-absorption effect. And for the experiments, in order to avoid the self-absorption, typically, the absorbance should be below 0.1 for the spectrum range we measured.

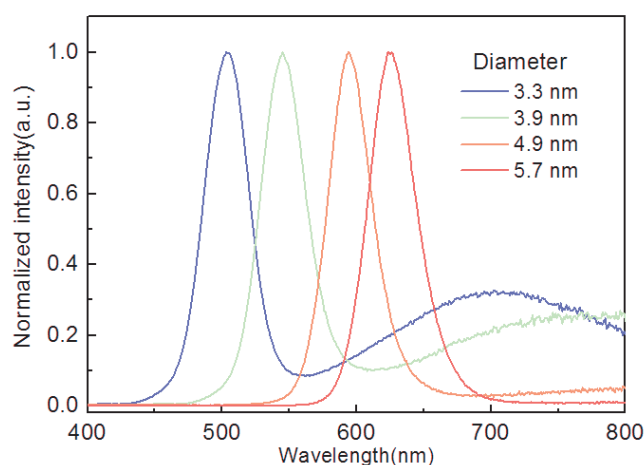


Figure 3.5 Evolution of the photoluminescence spectrum with increasing size of CdS/CdSe quantum dots, which are synthesized in our laboratory. Size is calculated by the precursors used.

3.2.3 Photoluminescence excitation spectrum

Photoluminescence excitation spectroscopy(PLE) is a complementary technique to identify the origin of PL peak feature. At a selected emission wavelength, the intensity of photoluminescence is measured at varying excitation wavelengths. We could observe all

the excitonic states contribution to the luminescence of the selected wavelength. It is expected that PLE spectra of the nanocrystals with well-defined size, shape and composition should be similar to their absorption spectra, as shown in Figure 3.6(a). Therefore, comparing to absorption spectrum makes it possible to figure out the presence of a secondary population. If the sample is polydisperse and secondary population appears during the synthesis process, a huge difference can be observed between ABS and PLE spectra (Figure 3.6(b)). The solution samples should be diluted to avoid the self-absorption, otherwise the PLE value will be much lower than absorbance. Usually, it is better to keep the absorbance lower than 0.1 at the excitation wavelength range.

In addition, the PLE measurements taken at different emission wavelengths provides valuable information about the uniformity of the synthesized nanocrystals. Generally, the detected wavelengths are fixed at the lower energy emission side, the higher energy emission side and the peak of the emission, as shown in Figure 3.6(c). When the three PLE spectra show exactly similar excitonic transitions, it suggests the formation of highly monodispersed and uniform nanocrystals and the effect of inhomogeneous broadening on linewidth is negligible.

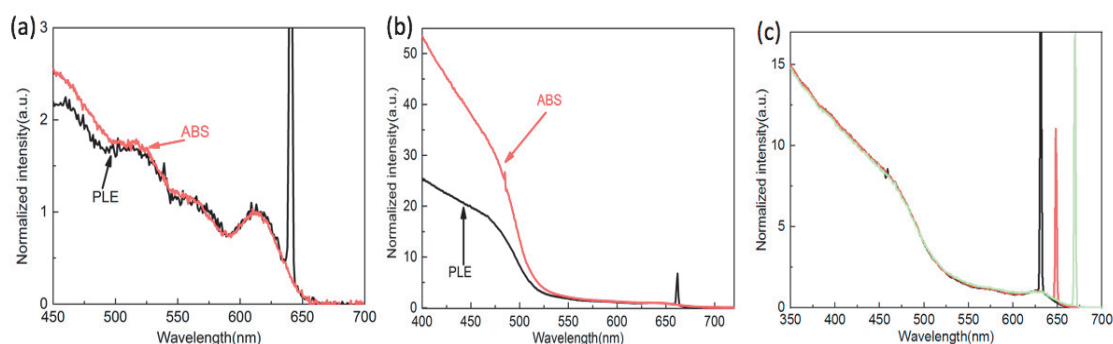


Figure 3.6 Comparison between ABS and PLE spectra. (a) without secondary nucleation and (b) with secondary nucleation. (c) taken at different emission wavelengths (the maximum of the emission, lower energy side and the higher energy side of the emission peak).

3.2.4 Quantum yield measurement

Fluorescence quantum yield (QY) is the emission efficiency of nanocrystals, which is the ratio of the number of emitted photons by absorbed photons, as expressed in equation (3-5):

$$Q = \text{Photons}_{\text{em}} / \text{Photons}_{\text{abs}} \quad (3-5)$$

where Q is the quantum yield. Two approaches are adopted for measurement of quantum yield, relative and absolute methods.

— Relative method

This method is widespread to determine the nanocrystals solution quantum yield. It is performed under identical measurement condition to compare an unknown sample with a

known quantum yield fluorophore, which is considered as a reference[116]. At the same absorbance, to compare the emission intensity with standard is a reliable way to estimate the quantum yield. Much more precise calculation is the gradient method, as depicted below:

$$Q = Q_{ref} \cdot \left(\frac{Grad}{Grad_{ref}} \right) \cdot \left(\frac{n^2}{n_{ref}^2} \right) \quad (3-6)$$

where Grad is the gradient obtained from the plot of the integrated fluorescence intensity vs. optical density, the subscript *ref* denotes reference, and *n* is the refractive index of the solvent.

The absorption and emission region of the reference is better if similar to test sample. To avoid self-absorption effects, for 10 mm cuvette, the optical density must be below 0.1 at the excitation wavelength(350nm in this thesis). The selected excitation wavelength should be sufficiently far from the emission spectra. And it is advisable to use a single detector for all the spectra measurement to minimize the experimental errors introduced by detector positioning[117,118].

— Absolute method

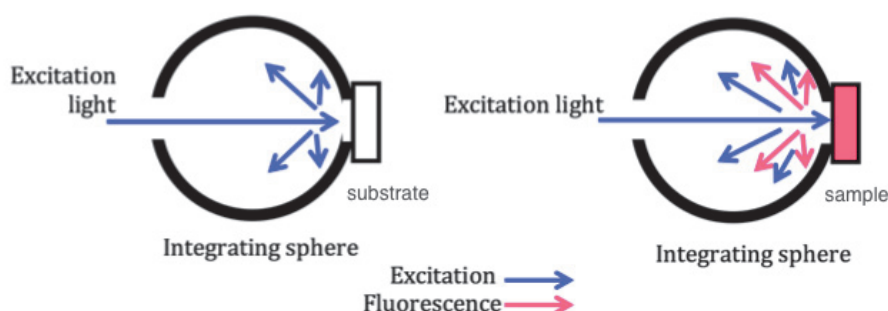


Figure 3.7 Schematic representation of absolute method with integrating sphere. Left: substrate spectrum measurement, right: sample spectrum measurement.

In comparison with relative method, the absolute method directly obtains the quantum yield by detecting all sample fluorescence through the use of an integrating sphere, as illustrated in Figure 3.7. The inner surface of the integrating sphere is highly reflective to make sure no light leak out. The advantage of this method is applicable for both solution and film sample test. Note that due to the energy transfer between particles in film sample, the quantum yield of film samples is usually lower than that of solution sample. Since, in our work, some large sized nanocrystals are not able to suspend stably in the solvent, absolute method will be a better way to determine the quantum yield. Absolute quantum yield of film samples was measured at the excitation wavelengths (410 nm and 450 nm) in this thesis, and the thin film samples were prepared by spin coating the particles on the glass substrate. The absorption and emission of glass substrate

and sample are measured, respectively, and then quantum yield can be given using the ratio between emission photons and absorbed photons of sample as definition[119].

3.2.5 Transmission electron microscopy

Studying the morphology of the colloidal nanocrystals including the shape and size distribution provides important information to verify the rationality and efficiency of synthetic protocol. Since the optical properties of the nanocrystals are also strongly related to their structural properties, the complete understanding of the structural properties of the samples is crucial to the development and improvement of novel heterostructural nanocrystals with the well-defined size, shape and composition, leading to the achievement of superior chemical and optical properties. In this thesis, we have mainly used transmission electron microscopy (TEM) to investigate the structural properties of our synthesized nanocrystals.

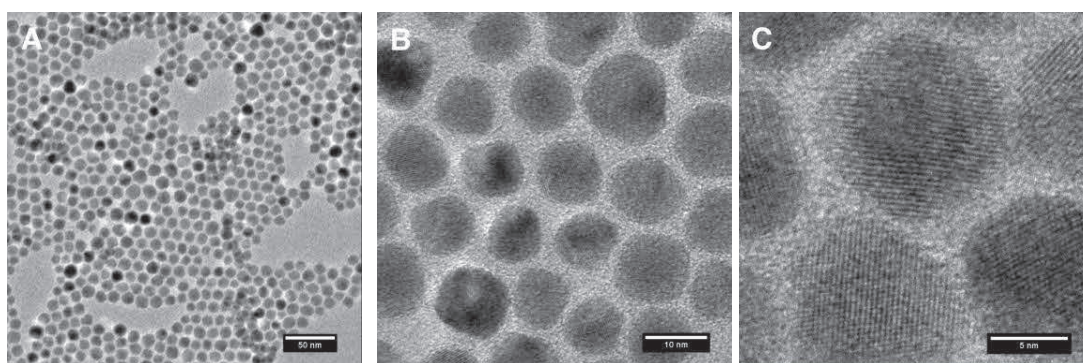


Figure 3.8 TEM images of nanoparticles at different magnifications: A.20000X, B.120000X, C.300000X.

TEM is a useful technique to intuitively investigate morphology and crystalline structure of nanocrystals (Figure 3.8). Electrons beam in microscopy is created by an electron gun and accelerated under 200 kV high voltage, then it is transmitted through an ultrathin mesh copper grid, and the image is formed from the interaction of the electrons with the sample. The sample preparation process is very important to the quality of the images, we usually first dilute our samples, the samples are necessary to be cleaned for several times to remove the excess amounts of organic ligands, which otherwise causes accumulation of charge at the surface under the electrons beam. Then, the diluted solution is dropped on the copper mesh grids and wait for the evaporation of the nonpolar solvent. Finally, the samples are kept under vacuum overnight for the complete drying before the measurements.

3.3 Spherical quantum wells synthesis and characterizations

SQWs(CdS/CdSe/CdS) consist of thin CdSe emissive layer sandwiched in two CdS layers. The strained epitaxial growth diminishes the misfit defects induced by the

structural strain, the high quantum yield of SQWs has been observed recently[81] and its quasi type II bandgap alignment makes it possible to decrease the Auger effect by engineering the electron-hole wavefunction overlap. Therefore, SQWs are considered as a good candidate for investigation of the scintillation properties of nanocrystals. Additionally, owing to the release of the structural strain as the shell grows in SQWs, we expect to synthesize a series of SQWs on a large size scale without the loss of the chemical and physical qualities to achieve the study on size dependence of scintillating phenomenon in nanocrystals. The synthesis and characterization are introduced in the following sub-section.

3.3.1 Synthesis

3.3.1.1 Chemical materials

- 1-octadecene, 90%, CAS : 112-88-9, Sigma Aldrich
- 1-dodecanethiol, 98%, CAS : 112-55-0, Sigma Aldrich
- cadmium nitrate tetrahydrate, >99%, CAS : 10022-68-1, Sigma-Aldrich
- cadmium oxide, 99.99%, CAS : 1306-19-0, Strem
- ethanol, >=99%, CAS : 64-17-5, Carlo Erba
- hexane, CAS : 110-54-3, Carlo Erba
- isopropanol, 99.9%, CAS : 67-63-0, VWR
- methanol, 98.5%, CAS : 67-56-1, VWR
- oleic acid, 90%, CAS : 112-80-1, Alfa-aesar
- oleylamine, 80-90%, CAS : 112-90-3, Acros
- selenium, 99.99%, CAS : 7782-49-2, Strem
- sulfur, 99.99%, CAS : 7704-34-9, Strem
- sodium myristate, >98%, CAS : 822-12-8, TCI
- toluene, 99.9%, CAS : 108-88-3, VWR
- trioctylphosphine, 97%, CAS : 4731-53-7, Sigma-Aldrich

Unless otherwise specified, all chemical materials are used directly without further purification or treatment.

3.3.1.2 Preparation of precursors

Cd(myristate)₂ is prepared according to a procedure published previously[107]. 9.3g sodium myristate was dissolved in 750mL methanol and stirring until completely dissolved (~1h). And 3.7g cadmium nitrate dissolved in 120mL methanol was mixed into the above solution and stirred slowly to obtain white precipitate(1h). Then the precipitate was filtered by a Buchner funnel, rinsed several times with methanol and dried under vacuum overnight.

0.25M S-ODE. 20mL ODE was degassed under vacuum for 30 min at 70 °C to evacuate oxygen and water(P<0.3mbar), and the reaction was performed under argon gas condition and 160mg sulfur powder was added into flask. Then the temperature was heated up to

140°C until all the sulfur powder was dissolved, and the flask was kept at 80°C to prevent sulfur powder from being precipitated out of solution.

0.5M Cd(OA)₂ in OA. 6.42g CdO was dissolved in 100mL oleic acid at 180°C, when the mixture was slightly yellow and transparent, the temperature was decreased to 120°C to avoid the Cd(OA)₂ degrade at high temperature. Then the flask was degassed until P<0.3mbar.

0.5M Cd(OA)₂ in OA/ODE. 6.42g CdO was dissolved in 50mL oleic acid and 50mL ODE at 160°C for 30mins under argon, and the solution was degassed at 100°C for 90mins. Comparing to the 0.5M Cd(OA)₂ in OA, the existence of ODE can prevent the nanoparticles from degrading by oleic acid.

2M TOPSe. 1.58g Se powder was added in 10mL TOP at 100°C for 4h until their complete dissolution. The reaction was performed in glove box to exclude the influence of oxygen. Then TOPSe was stocked under inert gas atmosphere.

3.3.1.3 Synthesis protocol

Spherical quantum wells synthesis is a three steps process[81]. CdS seeds are formed through homogeneous nucleation, and followed by a thin CdSe emissive layer synthesis. The subsequent shell growth is performed to cover different thickness shell on CdS/CdSe-based nanocrystals. For this subject, we are interested in samples coated by very thick shell, thus continuous injection of shell precursors was chosen to fulfill the formation of emissive layer and shell. The protocol is shown in Figure 3.9.

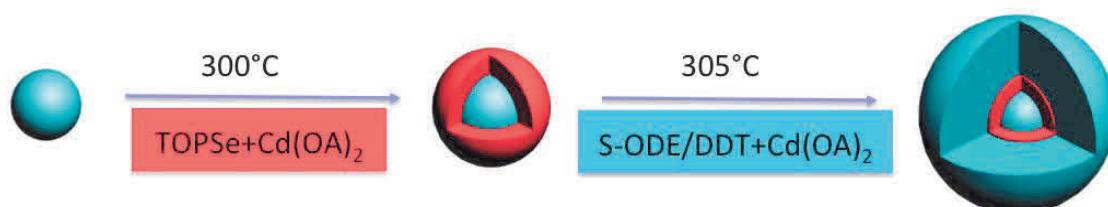


Figure 3.9. The protocol of spherical quantum wells synthesis

The specific experimental steps and parameters are as follows:

Synthesis of CdS seeds. 1.5mL 0.5M Cd(OA)₂ in OA/ODE and 27mL ODE were quickly switched under vacuum and argon for three times. Under flowing argon, the flask was heated up to 270°C, and 1.5mL S-ODE(0.25M) was injected at this temperature. Afterwards, temperature was decreased to 250°C immediately to undergo the growth process for 15mins. After cooling down the mixture to room temperature, the samples were purified by precipitation with ethanol, centrifugated at high speed and redispersed in hexane. The CdS seeds are around 3nm in diameter.

Synthesis of CdSe layer. 2.7mL CdS seeds at 193µM and 5mL ODE were degassed under vacuum at 65°C for 1h. The prepared 0.1M precursors mixtures (0.6mL TOPSe,

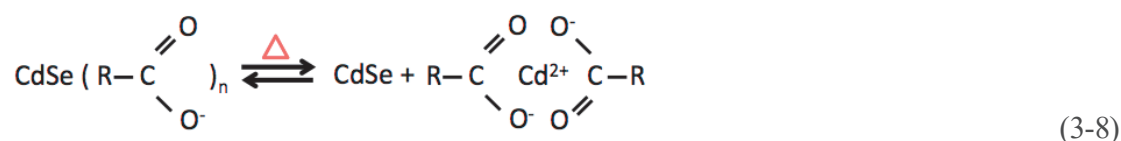
2.4mL Cd(OA)₂ in OA/ODE and 9mL ODE) was injected at 6mL/h at 300°C. 11.2mL mixture was consumed for the desired size emission layer. The solution was cooled down to room temperature, and precipitated with ethanol, toluene and OA. The final sample was suspended in hexane.

Reaction equation of CdSe layer synthesis:



Synthesis of CdS shell. 3mL CdS/CdSe(52μM), 85mg Cd(myristate)₂ and 10mL ODE are introduced in a three-neck flask. Cd(myristate)₂ was added to prevent the degradation of CdS/CdSe at high temperature. And the additional Cd²⁺ can invert the reaction as depicted in equation (3-8).

Reaction equation of CdS/CdSe degradation:



After 30mins of degassing under vacuum at 65°C, the solution was heated up to 305°C and 1mL OAm was injected to form monodispersed nanoparticles (It is better to inject after 2 drops precursors to avoid the CdSe layer damaged by OAm). Cd and S precursors were prepared as 0.2M solution of 1.58mL DDT diluted in 31.42mL ODE, and of 13.2mL Cd(OA)₂ in OA/ODE dissolved in 15.8mL ODE and 4mL OAm. The precursors were injected continuously into the flask by two syringes at 0.8nm/h under argon. Taking aliquots from flask at desired size, 15nm, 20nm, 25nm, 30nm, 35nm, 40nm in diameter, the specific parameters are shown in Table 3.1. The aliquots were reheated up directly to 305°C, 1.5mL Cd(OA)₂ in ODE was added to passivate the surface of SQWs. After 30mins annealing, the reaction was cooled down to room temperature. The nanoparticles were precipitated and redispersed with ethanol and hexane. Then the samples were suspended in hexane. 35nm and 40nm samples are unable to suspend in hexane due to their large size. For characterization, toluene has a good performance to disperse these large sized samples at low concentration.

Reaction equation of CdS shell:



Table 3.1 The reaction parameters for SQWs shell growth.

Diameter(nm)	15	20	25*	30	35	40
Cd precursor (mL)	19	33	43	51	63	72
S precursor (mL)	19	33	43	51	63	72
Ratio of aliquot	1/2	1	1/3	1/3	1/3	1
Concentration(μM)#	3.5	2.6	0.87	0.57	0.38	0.77

*: the reaction was ended at 20nm SQWs, and sample was washed and dispersed in 10mL hexane. The continuous reaction was restarted based on 20nm SQWs(1/2 of total volume) in 10mL ODE.

#: concentration is calculated for SQWs dispersed in 10mL hexane.

3.3.2 Characterization

For II-VI semiconductor nanocrystals, most research has focused on the size of CdSe quantum dots rather than CdS[111,120,121]. The published average diameter of nanocrystals is usually determined by transmission electron microscopy image. Since the low accuracy of this method in the case of small size nanocrystal measurement, the size of CdS seeds in our work is calculated according to reference[122], in which a relatively accurate size is determined by mean of small-angle X-ray scattering(SAXS). The diameter is given from the following equation:

$$D = (1.12 \times 10^{-6})\lambda^3 + (-1.13 \times 10^{-3})\lambda^2 + (3.81 \times 10^{-1})\lambda + (-40.5) \quad (3-10)$$

where λ is the wavelength of the first-excitonic absorption peak. And the extinction coefficient can be calculated by the below equation[123]:

$$\epsilon_{NC} = 6.53 \times 10^{-21} \lambda^{10.11} \quad (3-11)$$

which is using the half area of the first excitonic absorption peak as the correction of size distribution. Based on the extinction coefficient, the molar concentration of CdS seeds is readily obtained by the Lambert-Beer law:

$$C = \frac{A}{\epsilon_{NC}l} \quad (3-12)$$

Here, A is the absorbance at the first excitonic absorption peak of CdS seeds in a given solution (hexane), l is the optical length (1 cm).

3.3.2.1 Absorption and photoluminescence spectra

The absorption spectrum is performed with AvaSpec-2048L versatile fiber-optic spectrometer, which is used for measurements in the UV-VIS-NIR spectral range (200 to 1100 nm). A cuvette with pure hexane was measured as a reference, and then adding some microliters of the samples into cuvette to acquire the spectrum of CdS seeds. As mentioned above, the size of samples can be determined by the position of first excitonic peak on absorption spectrum. We thus taken out aliquots from the flask during the reaction to monitor the growth of the nanoparticles. The final band edge absorption is centered around 392nm (Figure 3.10), according to the calculation, the size of these CdS seeds is around 1.3nm in radius.

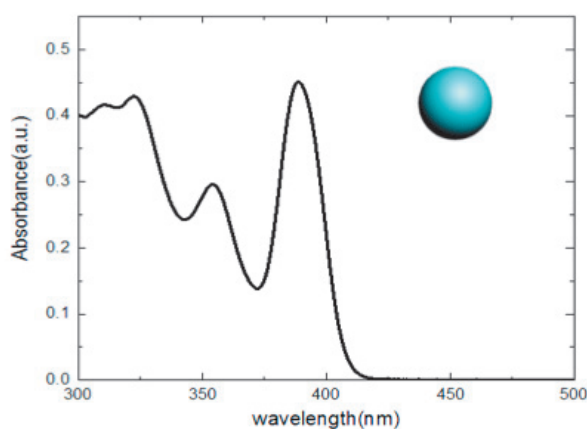


Figure 3.10 Absorption spectra of CdS seeds in hexane

The growth of CdSe emissive layer is manifested on the spectrum, as shown in Figure 3.11(a), aliquots taken at different introduced precursors shows a red shift as the size increases, which is related to quantum confinement effect. We got over the reaction when the band edge absorption is at around 610nm. The size of CdS/CdSe is determined from TEM images, 6.1 ± 0.5 nm in diameter in average (standard deviation of 8% compared to the average value), which corresponds to ~ 1.8 nm thickness of CdSe emissive layer in Figure 3.11(b). This value is consistent with the size we calculated before the synthesis. It means this layer grows homogeneously, all the precursors were

consumed on the CdS seeds, rather than forming the secondary population of pure CdSe nuclei.

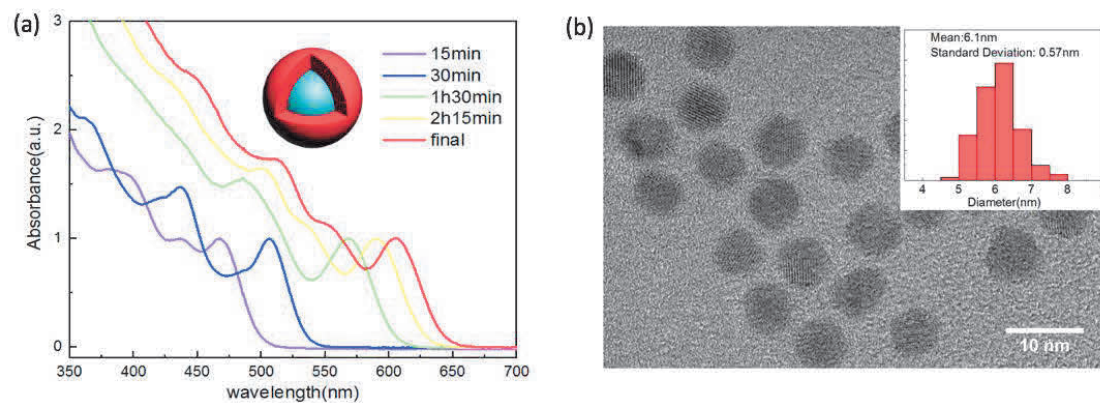


Figure 3.11 (a) Absorption spectrum of CdS/CdSe in hexane: variety color curves represent different aliquots taken during size growing, showing a red shift; (b) TEM image of CdS/CdSe at 400000X magnification, inset is the histogram of size distribution of ~ 100 particles.

The absorption and photoluminescence spectra of different size spherical quantum wells are presented in Figure 3.12. Photoluminescence spectrum is acquired on a FS5 spectrometer from Edinburgh Instruments. Samples suspended in hexane or toluene (35nm and 40nm diameter SQWs samples cannot be dispersed in hexane) are excited at 405nm. In order to interpret the onset of the CdS shell growth, we plot the CdS/CdSe spectrum as a reference. First, absorption at wavelength inferior to 510nm is dominated by the CdS shell, thus the increased absorbance indicates the growth of the shell. Meanwhile, the volume ratio of CdSe layer to CdS shell reduce continuously, making that the absorbance of the CdS shell is prevalent and the peak features of CdSe are nearly disappeared and negligible. Secondly, an obvious red shift after the formation of shell is attributed to the delocalization of electrons in the entire nanoparticle. For a quasi-type II energy band alignment, the degree of confinement reduces as the size increases, leading to a continuous low energy shift. However, we observed the identical emission position for variety SQWs synthesized, approximately at 650nm. The reason of this behavior is that we study ultrathick shell nanocrystals, where the change in energy gap is already very small[3].

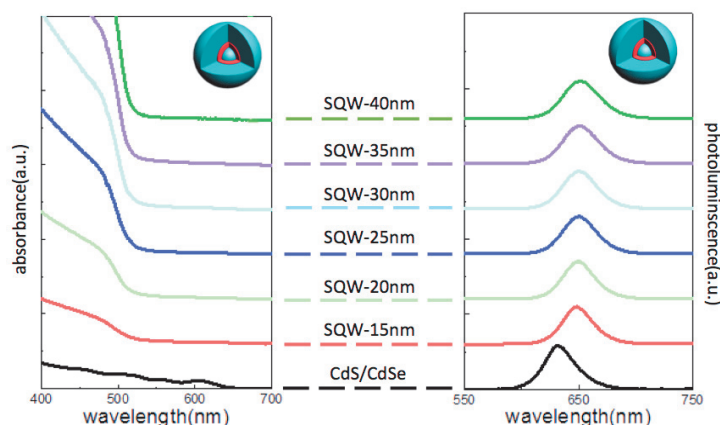


Figure 3.12 Absorption(left) and photoluminescence(right) spectra of CdS/CdSe and different sized spherical quantum wells: 15nm, 20nm, 25nm, 30nm, 35nm, 40nm.

The FWHM of all the SQWs samples is around 30nm, as we know, this value is strongly influenced by the polydispersity of the sample. Typically, CdSe quantum dots with a low polydispersity have a FWHM of around 20 to 30 nm. Considering the difficult-to-control size distribution of our samples due to their large size, 30nm width basically corresponds to monodispersed samples. Compared to 55nm of FWHM in the gradient potential QDs with comparable dimension in the previous report[37], the interpretation of the narrow linewidth is the relatively smaller size dispersion, as well as the small structural strain dispersion in sandwich-like structure[81].

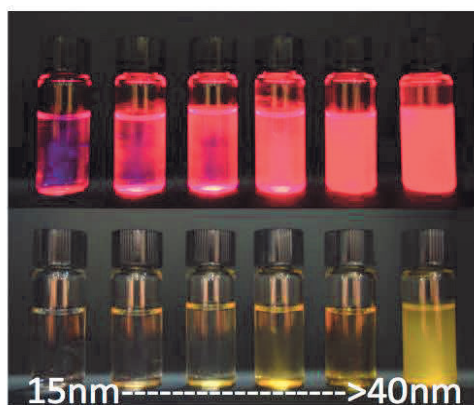


Figure 3.13 Image of different size SQWs from 15nm to 40nm dispersed in hexane or toluene with the same concentration under white light and UV light excitation.

All of the samples with same concentration under white light and UV light are shown in the Figure 3.13. Here, the quantum yield is measured with relative and absolute methods. The relative method is only applied for the measurement of smaller SQWs (15nm and 20nm). The quantum yield in solution are around 80% (reference sample is Rhodamine 101). And the quantum yield in film of larger SQWs (30nm and 40nm) are about 35% measured by absolute method. Owing to the energy transfer in film sample, the quantum yield should be higher in the case of solution. This high quantum yield in

such giant particles suggests the influence of the misfit defects as the shell grows is negligible in SQWs compared to the conventional core/shell structure.

3.3.2.2 Photoluminescence excitation spectroscopy

Photoluminescence excitation spectrum is measured with low concentration samples (absorbance < 0.1 at the whole measurement range) to exclude the impact of self-absorption. As we introduced above, PLE spectra allow us to identify the secondary nucleation through the comparison with absorbance. We acquired the PLE spectra on FS5 spectrometer from Edinburgh Instruments. As shown in Figure 3.14, we compared PLE spectra and ABS of CdS/CdSe and spherical quantum wells.

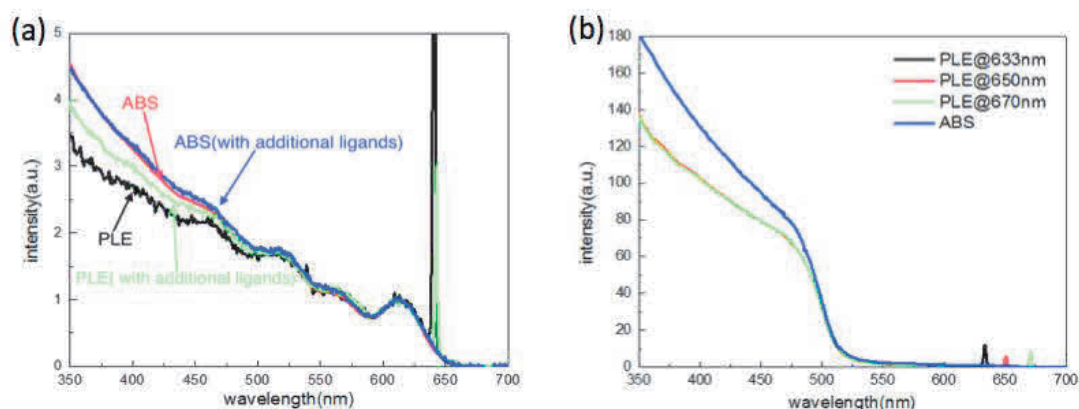


Figure 3.14 Comparison between ABS and PLE spectra. (a) CdS/CdSe and the same sample with additional ligands measured at maximum emission; (b) spherical quantum wells (30nm in diameter).

As shown in Figure 3.14(a), in comparison with ABS, the intensity of PLE spectrum of CdS/CdSe behaves slightly lower at short wavelength. After adding the carboxylate ligands, we observed an enhancement of the PLE intensity. Indeed, a part of the ligand is stripped during purification process, leading to the formation of the traps involved with dangling bonds. The capture of carriers by the traps is responsible for the reduction of the PLE curve. And the additional ligands can decrease the traps by bonding with the dangling bonds, resulting in the increase in the emission intensity. Therefore, the discrepancy between PLE and ABS is not caused by the secondary nucleation, we are allowed to conclude the samples are homogeneous.

For spherical quantum wells in Figure 3.14(b), we selected three emission wavelengths near the bandgap, the monodispersity of sample can be manifested with the identical PLE. Besides, the intensity of the PLE spectrum below 510nm should mainly indicate the presence of CdS shell. However, when compared with ABS, a discrepancy between two spectra can be seen, implying a small part of secondary nuclei CdS core existence in this sample. The impact of this small quantity of nuclei is acceptable in our work. And size-selected purification can be applied to separate two populations with different size.

3.3.2.3 Structural characterization

Figure 3.15 is the transmission electron microscopy images with different sized SQWs, the measurement was performed at magnification 30000X. The sample with a relatively low concentration was dropped on the copper grid. And then this mesh grid was degassed under vacuum overnight to remove ligands and solvent. TEM images allow us to visually compare changes in size and shape of samples. We clearly observed the increase in nanoparticle size, implying the successful shell precursors deposition on the core. The synthesized particles exhibit a faceted morphology and somewhat irregular shapes, as frequently observed for large core/shell QDs[4]. Since the shape of our samples is strictly not spherical, we selected maximum Feret diameter to represent the size of these samples. The size is estimated by software ImageJ, but the overlap between nanoparticles in large sample image compels us to measure them manually. The diameters of the samples are characterized from 15 nm up to approximately 40nm, exceeding the size of almost all published QDs until now. The size distribution standard deviations are around 12%, 10%, 15%, 10%, 10% and 12%, respectively (Figure 3.15, inset). These size dispersions are well enough for such large nanoparticles.

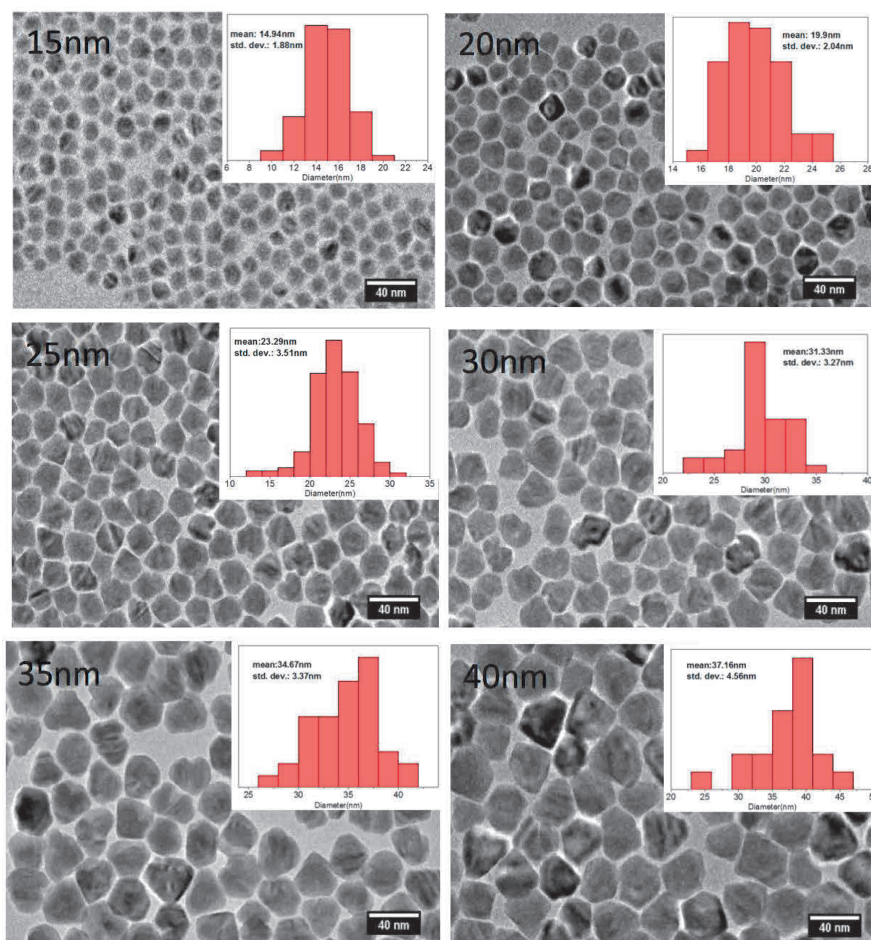


Figure 3.15 Transmission electron microscopy (TEM) images of different size SQWs at magnification 30000X, insets are histograms of size distribution.

We have synthesized a series of SQWs(CdS/CdSe/CdS) with different shell thickness, the total diameter is from 15nm up to around 40nm. The successful coating of the shell is demonstrated by analyzing the optical spectra and TEM morphology, all the samples emit at approximately 650nm with a narrower FWHM(~30nm). The narrow linewidths and about 10% deviation from TEM images are the evidence for the good size dispersion. Additionally, we have proved the SQWs synthesized exhibit high quantum yield ~80%, even for the giant 40nm SQWs the quantum yield in film is around 35%, which is the result of the reduction of misfit defects due to the release of the structural strain in SQWs.

3.4 Colloidal Synthesis and Characterization of Heterostructural Nanoplatelets

Nanoplatelets have been applied in many applications since it was first synthesized in 2008[77]. In this thesis, we will discuss another potential application as a kind of scintillating material. Due to the giant oscillator strength in nanoplatelet, its decay time is much faster than in traditional QDs, which is a significantly attracting property to the fast-timing radiation detection. Therefore, here, our aim is to synthesize different heterostructural NPLs: core/crown(C/C), core/shell(C/S) and core/crown/shell (C/C/S) to explore the underlying physics under X-rays excitation, and also to compare the difference on their scintillation behaviors.

3.4.1 Chemical materials

- 1-octadecene, 90%, CAS : 112-88-9, Sigma Aldrich
- 1-dodecanethiol, 98%, CAS : 112-55-0, Sigma Aldrich
- cadmium acetate dihydrate, >=98%, CAS : 5743-04-4, Sigma Aldrich
- cadmium nitrate tetrahydrate, >99%, CAS : 10022-68-1, Sigma-Aldrich
- ethanol, >=99%, CAS : 64-17-5, Carlo Erba
- hexane, CAS : 110-54-3, Carlo Erba
- oleic acid, 90%, CAS : 112-80-1, Alfa-aesar
- oleylamine, 80-90%, CAS : 112-90-3, Acros
- selenium, 99.99%, CAS : 7782-49-2, Strem
- sulfur, 99.99%, CAS : 7704-34-9, Strem
- sodium myristate, >98%, CAS : 822-12-8, TCI
- toluene, 99.9%, CAS : 108-88-3, VWR
- trioctylphosphine, 97%, CAS : 4731-53-7, Sigma-Aldrich
- zinc acetate dihydrate, >=99%, CAS : 5970-45-6, Sigma Aldrich

Unless otherwise specified, all chemical materials are used directly without further purification or treatment.

3.4.2 CdSe nanoplatelets

First, we started with the synthesis of CdSe core NPLs: 4ML CdSe nanoplatelets having four complete monolayers of CdSe with an additional layer of Cd atoms were synthesized with a slightly modified recipe from the literature[77]. In a three-neck 250 mL flask, 1.02g of cadmium myristate and 70 mL of ODE were loaded. The solution was degassed and mixed under vacuum at 90°C for 1 hour, the vacuum pressure being lower than 0.3mbar, to remove oxygen and undesired solvents. Then, 72 mg Se was dissolved in 2mL ODE, and it was rapidly injected into the flask under an inert atmosphere (argon). Afterwards, the temperature of the solution was set to 240°C. When the solution color becomes bright yellowish (generally around 205°C), 300mg cadmium acetate was added. The time of acetate addition is very important for the reaction yield of 4ML NPLs. After reacting for 10 min at 240°C, the solution was cooled to 150°C and 6mL OA was injected. Adding OA at high temperature is more effective, while injection of OA at low temperature will cause the aggregation of NPLs. Then, the temperature was continued decreasing to RT. When the solution temperature approached to the boiling point of hexane 69°C, 90 mL of hexane was injected to avoid the stacking of NPLs. The preliminary solution usually contains the surplus precursor and the byproduct as 3ML NPLs and QDs. Due to the difference in the size of different types of particles, we separate 4ML NPLs through size-selective purification step. By adjusting the ratio of solvent and anti-solvent, 3ML NPLs can be centrifuged out first. Next, further dissolution and re-precipitation can separate out ultra-small QDs. Therefore, we can get rid of the undesired byproduct and obtain the pure 4ML NPLs. Finally, the nanoplatelets were dispersed in hexane.

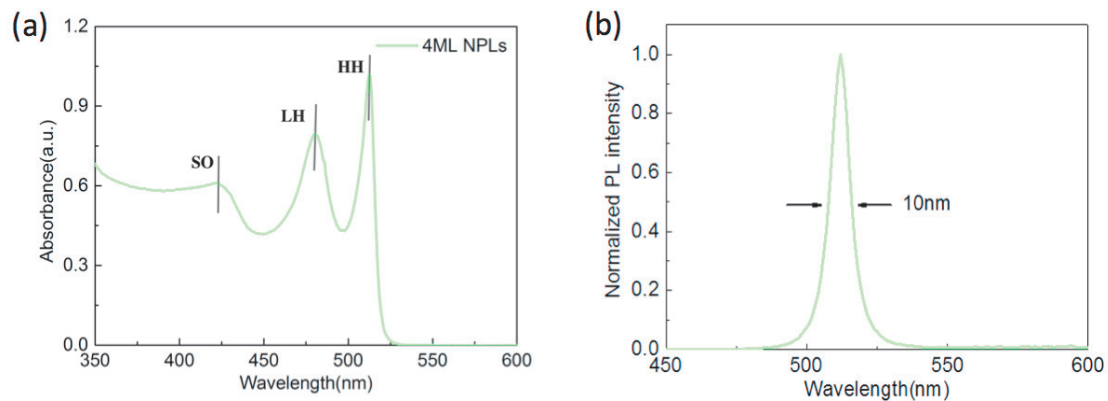


Figure 3.16 Absorption and normalized photoluminescence spectra of 4ML nanoplatelets. The excitation photon wavelength is 350nm.

Absorption and photoluminescence emission spectra of these CdSe core NPLs are given in Figure 3.16(a,b). The sharp excitonic features in absorption spectrum are observed around 480nm and 511nm, corresponding to electron/light hole (LH) and electron/heavy hole (HH) transitions, respectively, and the feature around 420nm is assigned to split off (SO) transition[90]. Furthermore, the very sharp emission profile of NPLs at 512nm is observed in the PL spectrum, the linewidth is narrower than 10 nm, indicating the high monodispersity.

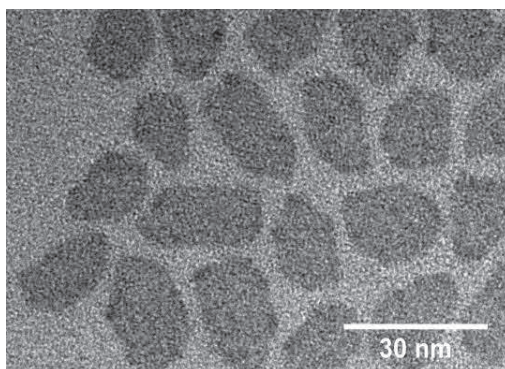


Figure 3.17 TEM images of 4ML CdSe NPLs.

TEM image of CdSe NPLs is shown in Figure 3.17. Although the morphology is irregular, most of the particles are rectangular-like, with the smallest lateral side length about 10nm. And the thickness of 4ML is around 1.2nm. So both of side lengths surpass the exciton Bohr radius of 2D CdSe, which is around 3.5nm[89,124], only vertical dimension is confined and no lateral confinement could be observed. These CdSe NPLs will be used as a core for the subsequent synthesis of core/crown, core/shell and core/crown/shell architectures.

3.4.3 Core/crown CdSe/CdS

In the past decade, the core/crown NPLs structure has received tremendous attention due to its excellent physical and chemical properties[92,125,126]. Here, we tried several different approaches to perform the synthesis, in order to obtain high quantum efficiency and uniform shape, including shell precursors mixture solution injection and different kind of anion precursor injection.

Approach 1: Anisotropic Growth Solution injection.

Anisotropic growth solution was prepared following the previously published procedure with slight modifications(scale up the quantity of precursors)[92]. The preparation is divided into two steps. First, for Cd precursor, 960 mg of cadmium acetate dihydrate, 680 μ L of OA, and 4 mL of ODE were loaded in a three-neck flask. The solution was heated to 100°C under vacuum for 20 min until the formation of whitish color homogeneous gel. For the preparation of S precursor (0.1M S-ODE), 150mL of ODE in 250 mL three-neck flask was degassed to remove air and water at 70°C for 30 min. Then under argon 480 mg sulfur was added. The temperature was set to 140°C until a slight yellow solution formed and then cooled down to RT. Then Cd precursor was mixed with 6 mL S precursor, heating and sonication steps were followed alternately till two precursors completely mixed, and then the anisotropic growth solution was used for the CdS crown coating.

For crown synthesis, 3mL 4ML NPLs (20 μ L core nanoplatelets dissolved in 3mL hexane has an absorbance of 0.15 at 350nm) and 5mL ODE were loaded into three-neck flask. The hexane was removed in vacuum for 1 h at 65°C. Subsequently, the temperature was heated to 210°C under argon and then different quantities of anisotropic growth solution was injected at 8 mL/h. After the injection, the solution was cooled down to room temperature and 1mL OA was added at 80°C to avoid the aggregation. The solution was purified by ethanol and hexane only once. Finally, the C/C NPLs was dispersed in hexane.

Approach 2: Single precursor injection-- S-ODE

First, a 0.05M S-ODE precursor was prepared by mixing 8mg of sulfur powder into 5mL of ODE. Afterwards, it was ultrasonicated for at least 30 min until a slightly turbid solution without visible precipitate. For crown growth, 4mL of ODE, 190 μ L of OA and 160 mg of Cd(Ac)₂ were combined into a 50 mL three-neck flask, then degassed for 1h at 65°C. 5mL NPLs was injected into the flask under vacuum. Then the solution was heated up to 220°C under argon. When the temperature reached 210°C, the S precursor was injected at 20 mL/h. After the injection of desired amount precursor, the solution was cooled down to room temperature, and 0.6mL OA was added at 90°C to avoid the aggregation. The solution was purified by ethanol and hexane only once, and then dispersed in hexane.

Approach 3: Single precursor injection--TOPS

Alternatively, crown synthesis based on the TOPS was a slightly modified procedure from the literature[125]. At first, we prepared 1 M TOPS solution by dispersing 160.3 mg of sulfur into 5mL of TOP. The solution was stirred overnight at room temperature in an air-free glovebox to ensure the S powder was completely dissolved. To avoid the oxidization, the solution was stored in the glovebox. Afterwards, 0.5mL of 1M TOPS solution was diluted in 9.5 mL ODE to form 0.05M TOPS, preparing for the crown growth procedure.

To overcoat a CdS crown, 8 mL of ODE, 180 mL of OA, 96 mg of Cd(Ac)₂ and 4mL of 4ML CdSe NPLs were combined into a 50 mL three-neck flask. As usual, the mixture was degassed in vacuum for 1 h at 60°C. Subsequently, the solution was heated up to 240°C under an argon atmosphere. When the temperature reached 215°C, 2 mL of 0.05M TOPS precursor solution was injected at the rate of 12 mL/h to form a thin crown. After completion of the injection, unlike the previous two approaches, the solution was directly cooled down to room temperature without additional OA. The solution was washed by addition of a 2: 1 ethanol : hexane mixture. The resulting C/C NPLs was finally redispersed in hexane.

The absorption and photoluminescence spectra of C/C NPLs synthesized by different methods were presented in Figure 3.18. They exhibit consistent electronic features. In comparison with core 4ML NPLs, with the formation of CdS crown layer, a new

absorption peak appears at around ~ 400 nm. By adjusting the amount of precursors, the CdS crown absorption peak becomes more pronounced, leading to a significant increase in the absorption cross section. However, the PL spectra show no significant change compared with core NPLs, this is ascribed to the lateral growth, maintaining the confinement on vertical dimension. The emission peak of all synthesized C/C NPLs is at approximately 515 nm, only a slight redshift (around 3 nm) in the spectra can be observed, which is caused by the change of dielectric constants due to the formation of the CdS crown [127].

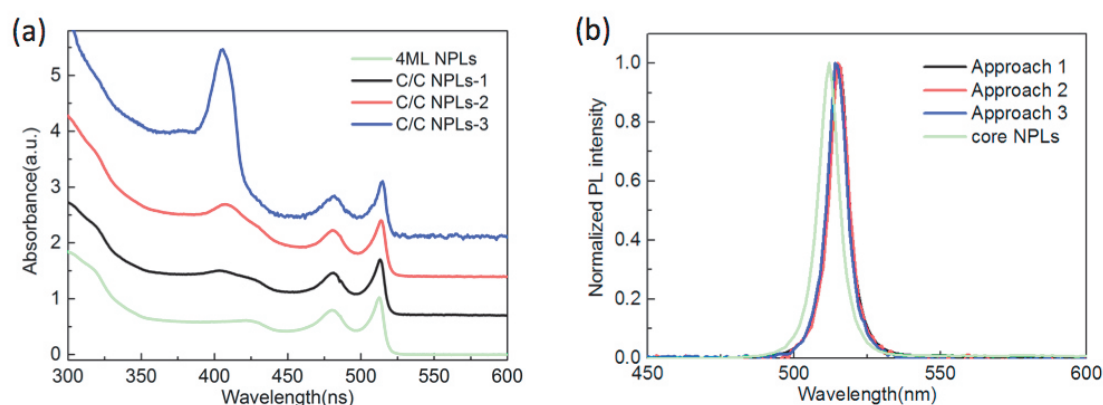


Figure 3.18 (a) Absorption spectra of CdSe/CdS core/crown NPLs with the crown increasing, (b) photoluminescence spectra of C/C NPLs synthesized by three methods with different crown size, comparing with core 4ML NPLs.

From the TEM images, the core/crown NPLs synthesized with S-ODE involved approaches usually show the irregular shape, as shown in Figure 3.19(a) and (b). On the contrary, the particle fabricated with TOPS gives a regularly shaped C/C NPLs with straight edges (Figure 3.19(c)) and this extreme uniform shape has been reported to cause a further increase of the quantum yield. It is also certain that the regular shape is helpful for subsequent overcoating and application. Replacing the common S-ODE with TOPS was demonstrated to affect the reactivity of sulfur, and the low reactivity was responsible for the formation of uniform shape [125]. Additionally, the PLE of C/C NPLs measured at three different selected wavelengths is illustrated in Figure 3.19(d), the emission at these three wavelengths originates from the same luminescent species since exactly similar spectral profiles are obtained, suggesting a great monodispersity in this core/crown NPLs. The analogous PLE has been observed for all the C/C NPLs in this thesis.

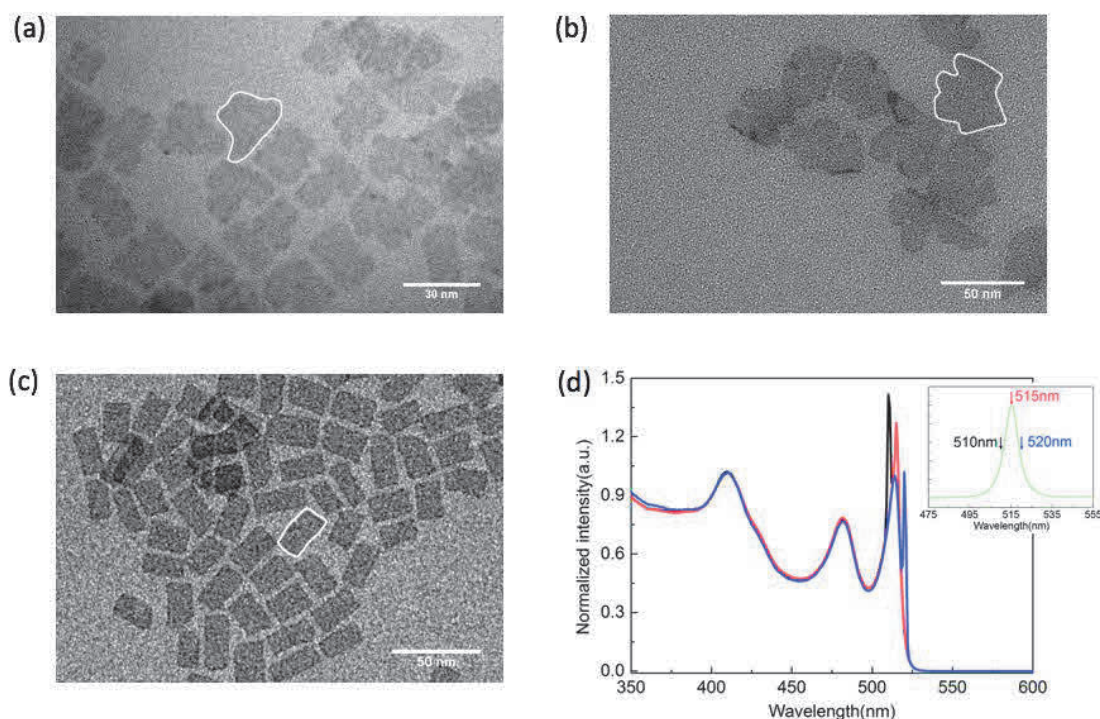


Figure 3.19 TEM images of core/crown NPLs synthesized by three different approaches, (a) anisotropic growth solution, (b) S-ODE, (c) TOPS. (d) PLE of core/crown NPLs (approach 3) at different emission wavelengths (as shown in inset).

3.4.4 Hot-injection alloyed core/shell CdSe/CdZnS

Motivated by the core/shell structure of QDs, in order to improve the performance of NPLs, different approaches and materials have been constantly investigated to fabricate heterostructural core/shell NPLs. To date, shell coating is usually achieved by two approaches. First, by alternately depositing cation and anion layers at low temperature, colloidal atomic layer deposition (c-ALD) techniques are able to form highly uniform growth shell with atomically precise thickness control[128]. However, c-ALD approach usually suffers from low quantum yield and poor stability issues. On the other hand, by adding the precursor of shell at high temperature, one can obtain core/shell NPLs with uniform and high quantum efficiency. But the lower thermal stability of NPLs, compared to that of QDs makes the high-temperature shell growth method difficult to perform in the NPLs system. To prevent etching and dissolution of the NPL cores prior to shell growth, Rossinelli *et al.* investigated different reaction solvents to develop a hot-injection shell growth method to coat a thick CdS shell on CdSe NPLs[129], which was demonstrated with predictable better chemical and optical quality.

Hence, our synthesis is according to the recently reported protocol to form an alloyed CdZnS by hot injection[130]. Specifically, 14mg of Cd(Ac)₂, 34mg of Zn(Ac)₂, 0.5 mL of OA, 5 mL of ODE and 5mL of CdSe core NPLs was loaded in a 50 mL three-neck flask together. The mixture was degassed at 80 °C for 1h to remove oxygen,

moisture, and hexane. Meanwhile, the precursors were reacted to form $\text{Cd}(\text{OA})_2$ and $\text{Zn}(\text{OA})_2$. Then, the solution was heated up to 300°C under argon atmosphere. Subsequently, 0.5 mL of oleylamine was injected quickly at 90°C . 350 μL of 1-Octanethiol dissolved in 20 mL of ODE was injected at 165°C at 10 mL/h. The addition of precursors at relatively low temperature can limit the destruction/etching of the core NPLs. Then the injection rate was decreased to 4 mL/h when the temperature reached 240°C . After the complete injection, the solution was kept for 50 min at 300°C for annealing and full consumption of unreacted precursors. Then the solution was rapidly cooled down to room temperature, and 5 mL hexane was added at 60°C . Finally, the core/shell NPLs was precipitated by ethanol, and redispersed in hexane.

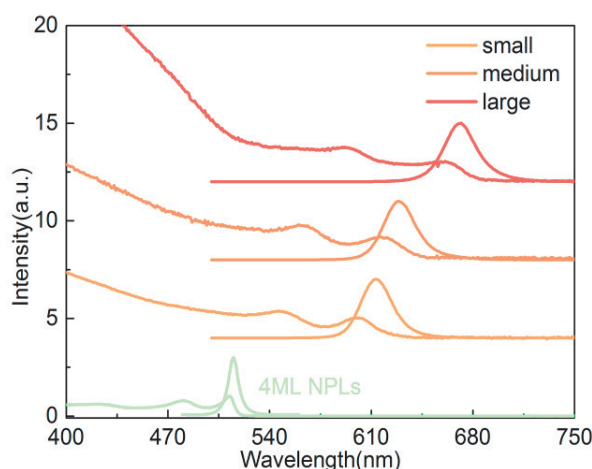


Figure 3.20 Absorption and photoluminescence spectra evolution of three core/shell CdSe/CdZnS NPLs with the increasing shell thickness.

We successfully synthesized three different thicknesses core/shell NPLs, emitting at 615 nm, 631 nm and 671 nm respectively. The absorption and photoluminescence spectra are given in Figure 3.20. In comparison with core NPLs, the absorption spectra also possess the clear HH and LH transitions peak, but the difference is that the excitonic features have been experienced a strong red shift when the shell is coated. This red-shift continuously increases with the increase in CdZnS shell thickness which can be explained by the decrease in quantum confinement. Besides, since the Cd reactivity is higher than that of Zn, the inner shell is mainly composed of CdS, and the outer surface is Zn-rich. The conduction band alignment difference of CdSe and CdS is negligible. Electron delocalization into the shell could be another reason for the excitonic features red-shifting. In addition, as the shell increases, the absorbance in the blue spectral region is enhanced, resulting in the larger absorption cross-section. And the FWHM of PL spectra are around 25 nm for all the samples. The broadening, compared to 4 ML NPLs, is attributed to stronger coupling to phonons in the shell[131]. The quantum yield in thin films is measured as approximately 50% for all the samples by absolute method.

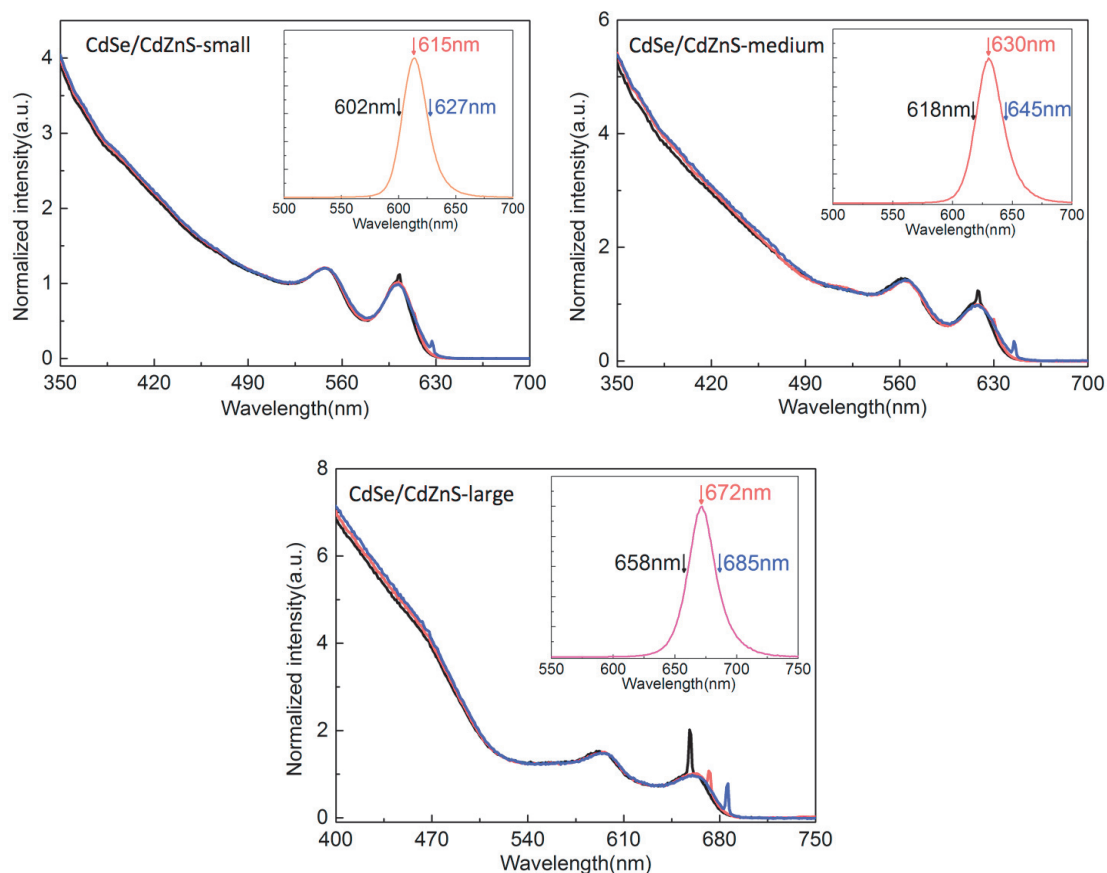


Figure 3.21 Photoluminescence excitation spectra of core/shell CdSe/CdZnS NPLs with different thickness shell measured at different emission wavelengths.

In order to verify the uniformity of the shell growth, we measured the core/shell CdSe/CdZnS NPLs PLE spectra at different emission wavelengths, as shown in Figure 3.21. The same excitonic features taken at fluorescence peak position and on both sides have been observed, which suggests a uniform coating of the shell and the induced inhomogeneous broadening is negligible. Moreover, from the TEM images in Figure 3.22(a), the shell growth is manifested as the change of the vertical thickness of nanoparticles, the thickness of the small core/shell NPLs is determined as around 3.5nm (4ML core NPLs thickness is ~ 1.2 nm), which matches with the estimated thickness of ~ 1.2 nm. It corresponds to 4 monolayers shell. And the thickness for medium and large core/shell NPLs are estimated as 4.2nm and 9nm, corresponding to 5ML and 12ML shell. Though the core shape is irregular, all the core/shell NPLs appear the rectangular shape, as presented in Figure 3.22(b) and (c).

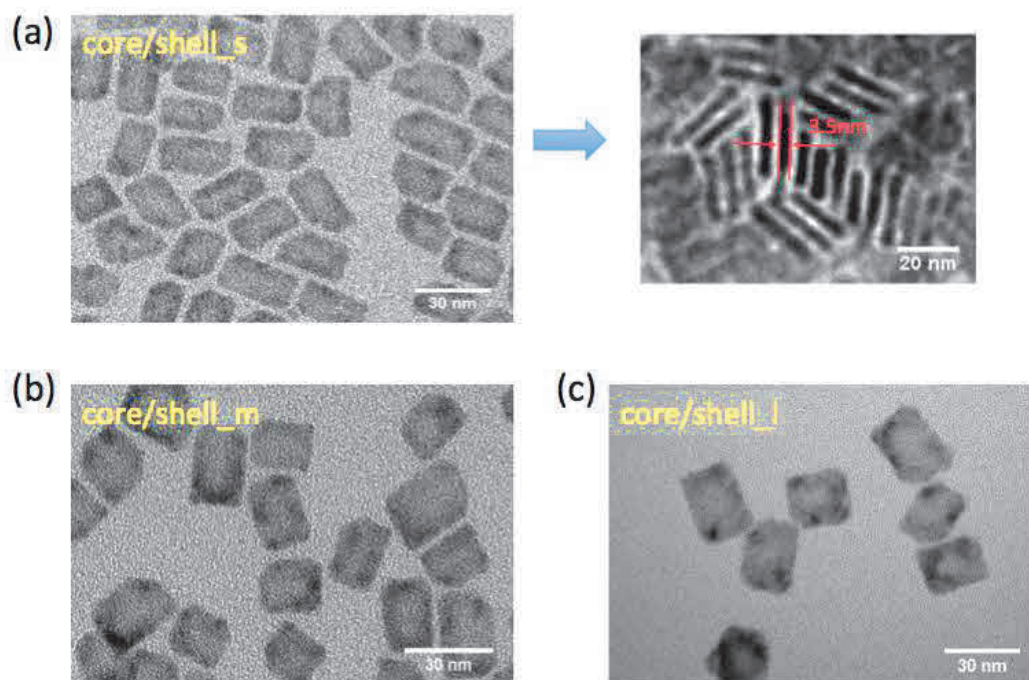


Figure 3.22 TEM images of different thicknesses core/shell CdSe/CdZnS NPLs. (a) and (b) are core/shell_s, the arrow shows the vertical thickness is around 3.5nm, (c) and (d) are core/shell_m and core/shell_l, respectively.

3.4.5 Hot-injection core/crown/shell CdSe/CdS/CdZnS

More complex architecture core/crown/shell NPLs has been recently employed to achieve amplified spontaneous emission(ASE), with an ultralow threshold of ~ 800 nJ/cm². This is attributed to the combination of the characteristics of C/C and C/S in this structure, that is, large absorption cross-section and suppressed Auger non-radiative recombination[115]. However, so far, the synthesis approaches of C/C/S NPLs are all based on c-ALD[97,98,115], resulting in low quantum yield and poor stability. In this thesis, we try to apply the hot-injection protocol to fabricate the core/crown/alloyed shell CdSe/CdS/CdZnS NPLs.

The procedure is similar with C/S synthetic method. Core NPLs were replaced with 3mL C/C NPLs(10mL in total, synthesized with TOPS) as the seeds, and they were mixed with 12 mg of Cd(Ac)₂, 27.5 mg of Zn(Ac)₂, 0.5 mL of OA and 5 mL of ODE into 50 mL three-neck flask, following by the degassing and reaction process. Then the solution was heated up to 300 °C under argon atmosphere. 0.5mL of oleylamine was injected quickly at 90°C. 350μL of 1-Octanethiol was dissolved in 20mL of ODE, and the injection rate was set as the same as above 10mL/h first, and then turned to 4mL/h until 7mL precursor was consumed. After the complete injection, the solution was kept for 20 min at 300 °C for annealing and then rapidly cooled down to room temperature. After washing and precipitating, the final C/C/S NPLs was dispersed in hexane.

In the Figure 3.23(a), we presented the absorption and photoluminescence spectra of C/C/S NPLs and an absorption spectra of C/S NPLs with the similar emission wavelength (dark dash). Except for the heavy hole and light hole transitions, the C/C/S exhibits a larger absorbance than that of comparable C/S NPLs, particularly in the blue spectral region. The marked increase at around 500 nm that is related to absorption from the coating CdS crown. However, the excitonic features are broadened, the width of the emission profile is around 40nm, larger than that of the regular C/S NPLs FWHM. To examine the uniformity of our sample, the PLE is shown in Figures 3.23(b): the spectra at different wavelengths of PL peak show the similar features, indicating that the origin species are not very distinctive. Therefore, the polydispersity of the particles is not the reason for the broadening of the spectrum.

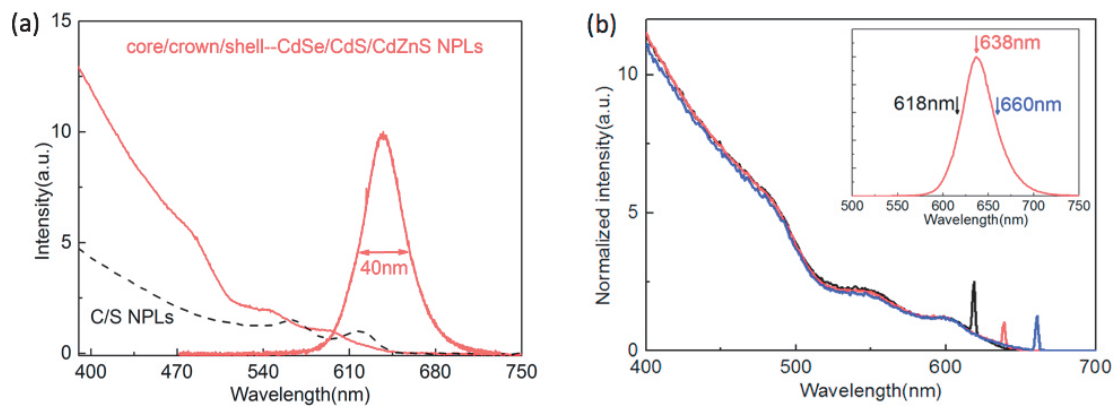


Figure 3.23 (a) Absorption and photoluminescence spectra comparison of core/shell (black dash line) and core/crown/shell NPLs (red solid line). (b) PLE of C/C/S NPLs with different thickness shell measured at different emission wavelengths.

From the TEM images in Figure 3.24, the lateral shape is nearly monodispersed and rectangular with average size (16 nm and 34 nm). The thickness in the center is around 3 nm, corresponding to 3 ML shell. However, the larger contrast has been observed at the corners, indicating the vertical size is thicker at the corner than the center. The resulting C/C/S NPLs thus form overall bone-shaped nanocrystals. Actually, this morphology has also been observed in core/shell. The presumable growth process was reported by Andrea Castelli *et al.* [132]. They explain it as anisotropic shell with double structures (zinc blend and wurtzite type). A cubic shell at first grows in thickness, and then {111} facets might be available at the corners, which provide suitable locations for the growth of a wurtzite shell. Here, I think the efficient change observed in C/C/S is due to the peripheral CdS crown promotes the wurtzite shell growth. And this bone shape should be responsible for the larger linewidth. The quantum yield in thin film was measured as ~25%, the reduction of the quantum yield compared to that of C/S NPLs is unknown, one of the interpretation might be the defects generated on the corners.

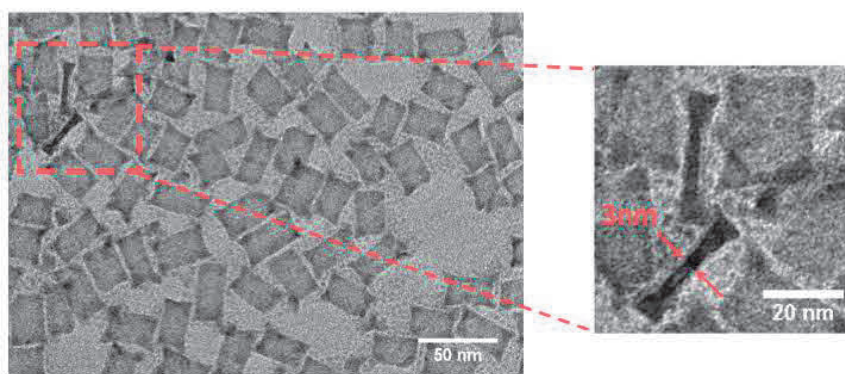


Figure 3.24 TEM image of core/crown/shell CdSe/CdS/CdZnS NPLs.

We have synthesized three different types of heterostructural nanoplatelets. First, for core/crown CdSe/CdS NPLs, by using the TOPS instead of the S-ODE as a S precursor, we achieved the improvement of the morphology with the rectangular shape, which is beneficial of the subsequent coating and the application. The low reactivity of sulfur in TOPS has been demonstrated to be responsible for the formation of uniform shape[125]. Secondly, we prepared the core/shell CdSe/CdZnS NPLs with three varying thicknesses by hot-injection approach. The quantum yield in film was kept around 50% for all the samples, which indicated the alloyed shell leads to the decrease in the defects induced by the lattice mismatch. Therefore, we will employ these samples to investigate the size dependence of scintillation properties on 2D nanocrystals. Finally, for the first time, we synthesized the core/crown/shell NPLs via the hot-injection methods, 3ML CdZnS was successfully coated on the CdSe/CdS. Though the broadening emission linewidth and a moderate quantum yield in thin film were obtained, due to larger absorption cross section, we believe that with the further development on the synthesis, this configuration will be promising.

3.5 Conclusion

In this section, based on the fundamental colloid nanocrystal synthetic theory, we first successfully synthesized a series of SQWs with different shell thickness. The total diameters of resulting SQWs are from 15nm up to approximately 40nm in diameter, exceeding the size of almost all published QDs until now. Thanks to the release of the structural strain in this sandwich-like configuration, the misfit defects in giant particles is much less than in conventional QDs, which is demonstrated by the high quantum yield (up to 80%) for 15nm and 20nm SQWs, even for the larger particles(40nm) the quantum yield is around 35% in thin film. The samples are also characterized with narrower photoluminescence spectra linewidth and an homogeneous morphology, suggesting the good quality of the synthesized samples. Besides, we have also fabricated different heterostructural NPLs, including core/crown, core/shell and core/crown/shell. Through using TOPS replaces the traditional S-precursor, we achieved the formation of the regular

shape of core/crown NPLs. And *via* hot-injection methods, three different sized core/shell NPLs with high quantum yield have been prepared. For the first time, we synthesized a core/crown/shell NPLs through the hot-injection method, though the quantum yield is only 20% in film, this experiment proved the possibility to fabricate this structure by hot-injection methods. These samples will be applied in the subsequent research regarding scintillation mechanism of nanocrystals under ionizing radiation.

Chapter 4

Scintillation properties of spherical quantum wells under X-rays excitation

The breakthrough of the Auger recombination suppression has stimulated the development regarding the application of the multiexcitons phenomena in semiconductor nanocrystals, such as low-threshold NCs lasers, light emitting diodes, as well as solar-energy conversion[4,133–135]. In addition, another attractive application is for radiation detection scintillator materials. So far, there have been several related reports[8,10,11,136], but a few were reported on the energy deposition and relaxation process of high-energy photons in NCs.

Therefore, in this chapter, we first introduce several characterization techniques used here, including steady-state radioluminescence spectroscopy and time-resolved measurement. Next, we will compare the temporal and spectral features under intense optical excitation and X-rays excitation of SQWs with different sizes to realize the identification and assignment of excitation species, involving single exciton and multiexcitons recombination. The scintillating behavior evolution with the size of SQWs is further given. By comparison of spectral analysis with numerical simulations, we are able to draw a picture of a fundamental understanding of the underlying physics in the scintillation process of such nanocrystals.

4.1 Experimental setups

4.1.1 Radioluminescence setup

The light emitting induced by ionizing radiations is referred as scintillation sometimes also called radioluminescence(RL). The measurement setup under X-rays excitation in our laboratory is presented in Figure 4.1, which consists of an X-rays tube, a monochromator and a CCD. The technical difference from PL measurement setup is that the incident X-rays is generated in a protective cover to prevent the leak of the radiation. And then for the sample preparation, unlike that of the photoexcitation, glass and quartz substrate are usually not the good candidates for measuring scintillation luminescence under X-rays excitation, because the excitation can be strongly absorbed and their intrinsic scintillation signal, even with a poor yield introduce a significant effect on the

sample spectrum because of the significant X-rays absorption as compared to the studied film (a few tens of nm). Furthermore, the amount of nanoparticles in the solution sample is relatively low, making an inefficient absorption and emission intensity under X-rays radiation. Hence, instead of dispersed NCs in cuvette, X-rays induced luminescence can only be performed using a solid film sample dropped on Si substrate. Additionally, our setup can also be employed to achieve the PL measurement, facilitating the spectra comparison with radioluminescence.

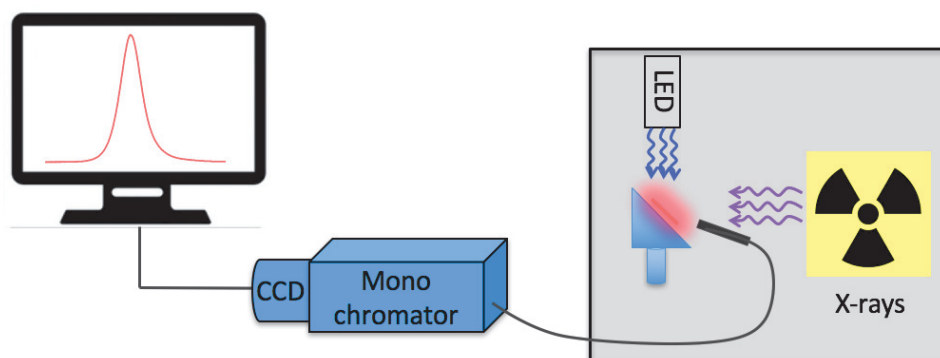


Figure 4.1 Schematic representation of radioluminescence and photoluminescence setup.

4.1.2 Time-resolved measurements

Time-resolved spectroscopy is a useful technique to study excited state dynamics of nanocrystals and the understanding of complex spectral shapes. It gives us the opportunity to observe, explore and understand the fast time multiexcitons events taking place in the NCs. Here, decay curve measurement and time resolved emission spectrum are presented.

4.1.2.1 Decay curve measurement

Decay curve measurement is using time-resolved spectroscopy to record the fluorescence decay curves of the samples. Since the PL signal is proportional to the average number of exciton formed in the excited NCs, it allows to directly measure the exciton population in time following the different kinetic recombination processes. The setup consists of a pulsed laser emitting at 405nm, a monochromator, a photomultiplier tube (PMT), PicoHarp300 time-correlated single photon counting (TCSPC) and several filters, as shown in Figure 4.2. In principal, a pulsed laser excites the sample and triggers the counting, and then the emitted photons from the sample after a certain time are detected by a PMT at a selected wavelength. The electronic system records the time between the laser pulse generation and the sample's photon detection. At the end, the detected photons are counted as a function of the time. This process is repeated millions of times. These photon counts from many excitation events compose a histogram to form decay curve over time. The smallest time bin of our TCSPC is 16ps, while the overall full

width half max spans from 200ps to 400ps depending on the set power of the laser, which is high enough to analyze the multiexcitons with a lifetime of on the order in the ns range. Moreover, the laser repetition rate must be slow enough to ensure that all the excitonic species have time to recombine before the next laser pulse. Typically, the repetition time is at least 3 times longer than the longest lifetime of the NCs. In addition, in order to avoid artefacts caused by the high emission intensity, we keep the input counts value lower than 5% of the laser repetition rate.

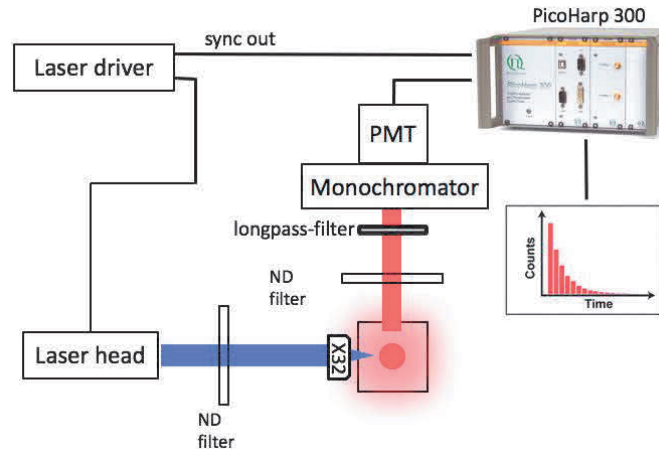


Figure 4.2 Schematic representation of photoluminescence decay curve measurement setup.

By analyzing the kinetics of fluorescence decay curves, one can obtain information on the sample's photoluminescence lifetime, which is an important characteristic of NCs. Theoretically, this decay curve can be fitted by an exponential with a time constant $k = 1/\tau$ which is the lifetime:

$$N(t) = N(0)e^{-kt} = N(0)e^{-t/\tau} \quad (4-1)$$

However, when considering the polydispersity of the sample or several recombination pathways, like the multiexcitons, these yields to different monoexponential decays, resulting in the multiexponential fitting of the measured decay curve as in the following equation:

$$A_1e^{-t/\tau_1} + A_2e^{-t/\tau_2} + A_3e^{-t/\tau_3} + A_4e^{-t/\tau_4} + Noise \quad (4-2)$$

By adjusting neutral density filter, we are allowed to acquire the decay curve under variety laser powers. Based on the definition of the multiexcitons, we can identify the excitonic species through the analysis of the power dependence on each time constant. Therefore, it is a very commonly used technique to study the radiative and non-radiative recombination of multiexcitons. Besides, in this thesis, this setup can be modified to perform the decay curve under X-rays excitation. The specific adjustments can refer to the relevant part in Figure 4.3.

4.1.2.2 Time resolved emission spectrum

Due to the ultra-fast recombination characteristics of multiexcitons, steady-state spectroscopy is not the most efficient approach to observe multiexcitons emission features. Inspired by the time-resolved decay curve measurement, we take the decay curves at different wavelengths, and then integrate the counts of emitted photons at different times over the whole measured spectral range through a homemade program to obtain fluorescence spectra under different time windows, which is called as time resolved emission spectrum. In this case, we are allowed to extract the extremely fast recombination components from the entire spectrum, enabling a direct comparison between multiexcitons and single exciton recombination spectra. Combined with the fluorescence decay curve, it can be beneficial for us to have a deeper understanding of the excitons dynamics in nanocrystals.

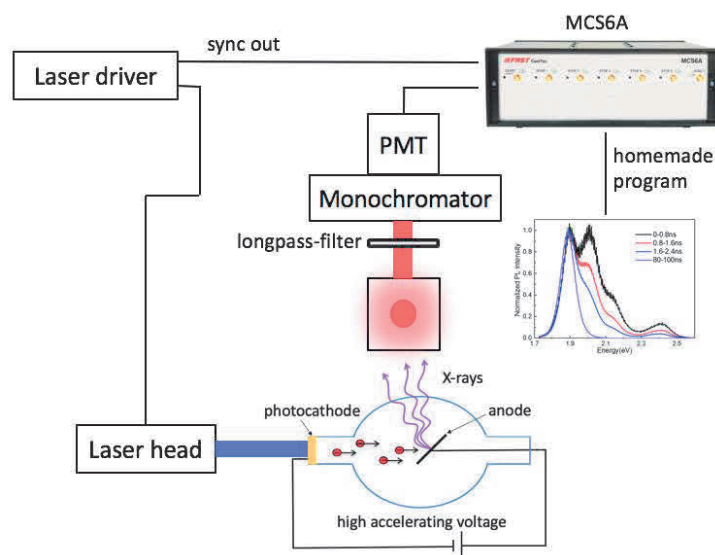


Figure 4.3 Schematic representation of time resolved emission spectrum setup under X-rays excitation

The schematic representation of experimental setup is given in Figure 4.3, which is exemplified as X-rays excitation. It consists of a pulsed laser, an X-rays tube, a PMT, a monochromator and a multichannels counting MCS6A. Samples were mounted in front of the window of the X-rays tube. First, a laser pulse triggers the counting to start, simultaneously, pulsed X-rays with same repetition rate are generated by the laser at 405nm to excite the samples. Then by scanning the wavelength in monochromator, the emitted photons are collected by PMT after a certain time to form the decay curve of different wavelengths in MCS6A. Subsequently, the homemade Labview program integrates decay curves for all wavelengths describing the emission spectrum. The time gating is done after a post treatment, with a variety of time windows, giving a time resolved emission spectrum. Similar to the lifetime measurement, it can also be used for photoexcitation measurement with slight modification (Figure 4.2). The power dependent

spectra can be acquired by adjusting the neutral density filter. However, the difference is that the TCSPC is replaced by a multichannel counting, to overcome the artificial issue caused by the deadtime of TCSPC in the case of a great amount of emitted photons. The drawback is the minimum time bin restricted to 800ps, making it less resolving for the lifetime record.

4.2 Possible mechanism in nanocrystals and simulation

4.2.1 Possible scintillation process in nanocrystals

It is well known that multiexcitons can be produced by absorbing more than one photon in a very short time window from the same pulse upon intense optical excitation, following by the thermalization process and relax the carriers to the lowest energy state, as shown in Figure 4.4(a). Alternatively, the multiexcitons can also be generated through a carrier multiplication process with the absorption of a single photon whose energy is at least twice than the energy gap. Twice the gap is the minimum required from energy conservation considerations, but in general it is admitted that it requires several times the gap [137]. The hot electron releases its energy by inelastic scattering with another valence electron, promoting it into the conduction band. Inspired by the carrier multiplication of moderate energy photon, the involved mechanisms under X-rays irradiation and more generally under ionizing radiation can be speculated. The energetic electron interaction with matter is undoubtedly a complex process involving multiple time, energy and space scales, therefore the process differs significantly from the moderate photon excitation. In brief, the X-rays photon interaction with materials leads to the photo-ionization of an electron from a core band generating a primary highly excited electron-hole pair composed of a core hole and a hot electron (several keV). The primary electrons essentially escape from the material and generate secondary electrons by elastic collision. Subsequently, these unstable hot carriers will undergo the carrier multiplication process. Once secondary electron-hole pairs cannot be produced due to the lack of energy as compared to the gap, the thermalization process becomes dominant and phonons are produced, ultimately forming exciton and multiexcitons and emitting light when the radiative transitions are favorable. The plausible mechanisms are sketched in Figure 4.4(b). The hole relaxes mainly through Auger cascade generating as well secondary electron-hole pairs. In a less extend, X-rays florescence occurs. Unlike bulk scintillating materials, instead of transporting the charge carriers up to their radiative recombination or their energy transfer to a luminescence center [64,138], the case on nanocrystals experience significant escape of charges, depending on the particle size, as described in Bulin *et al.* [80]. Motivated by this hypothetical analysis, we will explore the scintillation characteristics in NCs by comparing the optical response under X-rays and intense light excitation.

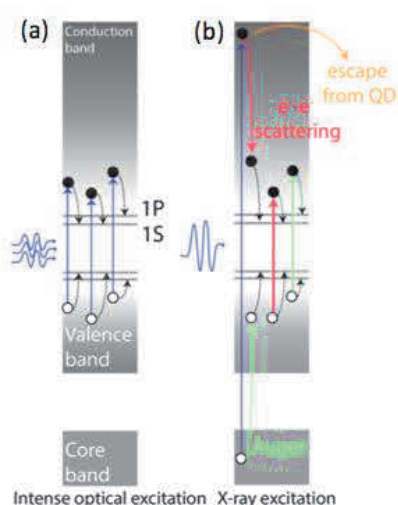


Figure 4.4 Schematic representation of the multiexcitons formation process in nanocrystals (a) Absorbing three low energy photons simultaneously by intense pulsed excitation, (b) Simplified energy relaxation process by X-rays excitation (only three electron and hole pairs are shown).

4.2.2 Simulation of the scintillation process in nanocrystals

This simulation part has been fully performed by Prof. Andrey Vasil'ev from the Lomonosov Moscow State University. In order to simulate the physical mechanisms occurring along the energy relaxation, we used the micro-theory of scintillation fully based on the dielectric response function of the material, which is recently observed in the reference[139]. Originally developed for single crystals, the model has been adapted for nanocrystals, namely considering the geometrical parameters of the SQWs and introducing a work function in order to build up the energy diagram (Figure 4.5).

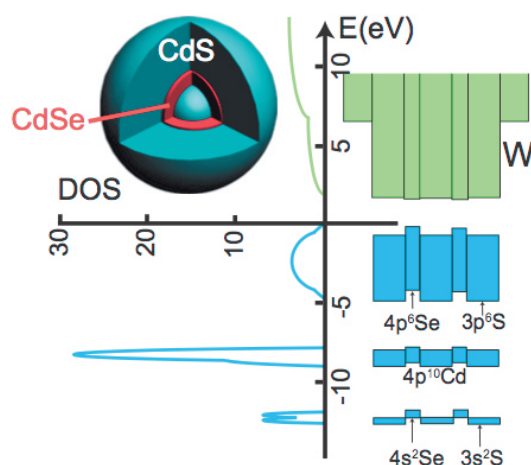


Figure 4.5 Schematic energy band diagram and density of state function of the SQWs.

Excitation of NCs under X-rays is due to fast electrons created from primary photoelectric event in some SQWs. A fast electron with kinetic energy from 10 to 30 keV produces secondary electronic excitations (SE) in a NC. The first part of the simulation estimates the number of produced secondary excitations as a function of the particle diameter. These secondary excitations (SE) have different total energies, and the distribution of SE energies in bulk materials is proportional to the energy loss function $Im(-1/\epsilon(\hbar\omega))$ where ϵ is the complex dielectric permittivity of the material, and it depends on the energy lost $\hbar\omega$. It can be obtained from the Livermore database. For isolated NCs the distribution of SE over energies deviates from the bulk energy loss function due to appearance of surface plasmon resonances, but, for packed NCs, we can use the bulk approximation. Because of the complexity, we have considered a two-step procedure. First, the distribution of the number of scattering events per particle for the primary electrons forming 1, 2, 3... energetic secondary electron-hole pairs are estimated. Then, for a given number of scattering, *i.e.* initial number of SE, we estimate the time dependence of the population of the formed neutral excitons (X, XX, XXX...) as well as charges species (X^+ , XX^+ ...). This second part takes into account the electron-electron interaction, the thermalization *i.e.* the electron phonon scattering, the Auger process, a work function of $W=5\text{eV}$ as well as the radiative recombination considering the following cascades (case of XXX) $XXX \rightarrow XX + h\nu_{XXX} \rightarrow X + h\nu_{XX} \rightarrow h\nu_X$. The simulation is based on rate equations with changing of the number and charge of excitations. It supposes a strong interaction of excitations in NC; the coefficients of rate equations are proportional to the densities of states.

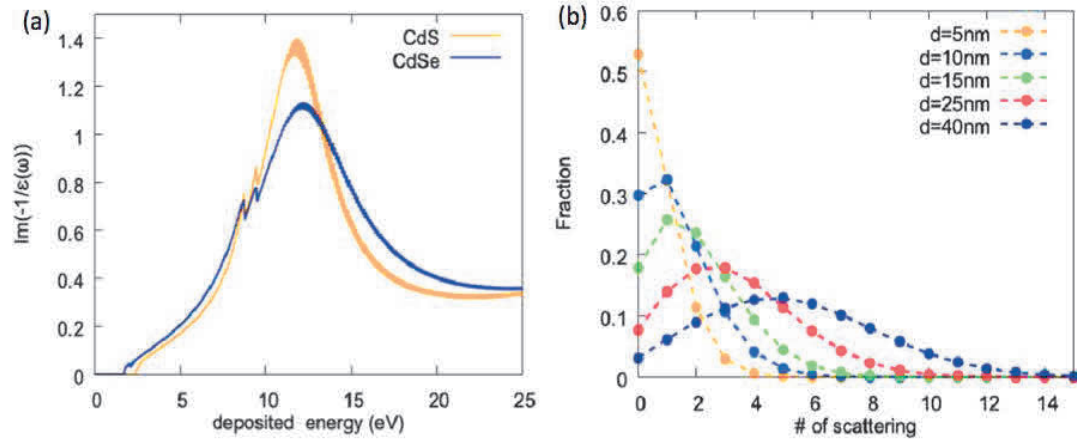


Figure 4.6 (a)Energy loss function restricted to 0-25 eV for CdS and CdSe. (b)Distribution of the number of scatterings for a 30keV primary electron for various particle sizes.

As for the distribution of the number of electron-electron scattering for the primary electrons, we can approximate the mean energy of these excitations to be about the plasmon energy corresponding to the maximum of the energy loss function presented in Figure 4.6(a) (about 12 eV for CdS and CdSe). The mean number of SEs produced by an electron passing through a NC is therefore $(-dE/dx)\Delta x/\hbar\omega_{pl}$, where $(-dE/dx)$ is the

stopping power (2.5 eV/nm for an electron having a kinetic energy of 30keV in CdS), Δx the mean free path of an electron through NC with diameter d ($\Delta x = 2d/3$) from geometrical considerations). The number of SEs created in matter should be distributed according to Poisson distribution. More accurate consideration demands techniques like the one used by Landau when he described so-called Landau fluctuations, *i.e.* fluctuation of energy deposited by a particle in thin layer with Δx width. Just for the estimation, the average of the SEs with energy $\hbar\omega_{pl}$ produced by a fast electron in NC with diameter d is distributed in nearly Poisson way as seen in Figure 4.6(b). As an intermediate remark, the distribution of the number of SEs highlights that multi-SE is likely to occur even in the 15nm particles and is dominating at larger sizes. For that reason, we have considered for the second steps of the simulation several initial situations where the particles contain 1, 2, 3... SE with energies distributed along the energy loss function.

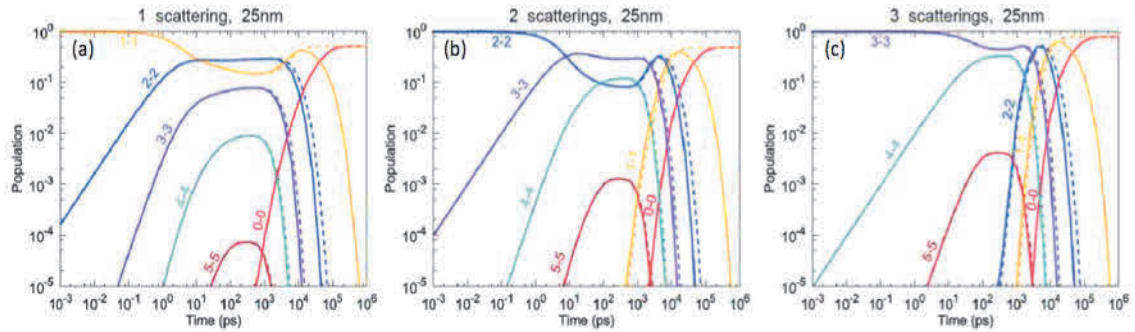


Figure 4.7 Simulation of evolution of excitations in NCs. (a) calculated time evolution of the population of neutral excitations (1, 2, 3 ... electron-hole pairs) for a 25nm SQWs considering an initial situation with a single secondary electron hole pair. Dashed curves corresponds to the simulation without considering radiative recombination. (b) and (c) Same simulation with initial situation with 2, 3 secondary electron hole pairs. For the simulation, radiative recombination considers a radiative decay time: $\tau_X=50\text{ns}$, $\tau_{BX}=12.5\text{ns}$, $\tau_{TX}=5.6\text{ns}$. Excitation source: 20keV photons.

For clarity, we present the time evolution of populations of neutral species for a 25nm particles in Figure 4.7. In order to describe the mechanisms prior to the radiative relaxation, the dashed lines correspond to the simulated population when the radiation recombination is turned off. It allows to highlight that the population evolutions of high order excitons considering radiative transitions (solid curves) is almost superimposed to the curves when the radiative recombinations are turned off (dashed curves) evidencing that the Auger quenching is dominating. We thus did not consider photon emission of higher order exciton than XXX. In order to extract the trends for comparison with experimental data, the ratio of various emission species with the neutral X are summarized in the Table 4.1.

Table 4.1 The ratio of various emission species with the neutral X.

	# SEs	15 nm	25 nm	40 nm
XX/X	1	0.22	0.25	0.29
	2	0.34	0.35	0.39
	3	0.34	0.35	0.39
X ⁺ /X	1	0.12	0.086	0.064
	2	0.88	0.51	0.32
	3	0.25	0.14	0.087
XXX/X	1	0.026	0.038	0.05
	2	0.17	0.19	0.23
	3	0.20	0.23	0.26

4.3 Steady state radioluminescence

To assess the scintillation property, a series of SQWs were tested under X-rays illumination. As a first step toward probing the scintillation behavior in nanoparticles, we compared steady state emission spectra under optical and X-rays excitations of 15nm, 25nm, 30nm and 40nm SQWs deposited on silicon substrate. Before deposition, the solution of SQWs was diluted in a solution of hexane : octane (9:1). The mixture of hexane and octane can dry homogeneously avoiding the coffee-ring effect that concentrates the NCs on the border of the drop[140]. The films were obtained by dropcasting respectively 40 μ L, 20 μ L, 20 μ L and 10 μ L of solution concentrated at 3.5 μ M, 0.87 μ M, 0.57 μ M and 0.77 μ M and then the films were left to dry several minutes. Because the goal is to compare spectral shapes under X-rays and optical excitation, it requires to guarantee to be out of any significant self-absorption regime (able to modify the spectral shapes), and radioluminescence is more sensitive to the thickness of the sample since the extremely strong penetrating ability of X-rays. Therefore, very thin films are required to perform the experiment. The steady state spectra were performed on a SR-500i imaging spectrometer from Oxford Instruments. When compared to the PL spectra of the solution samples (abs<0.1 at excitation wavelength) as shown in Figure 4.8, no obvious shift and broadening were observed, indicating the self-absorption and energy transfer of the film samples were negligible.

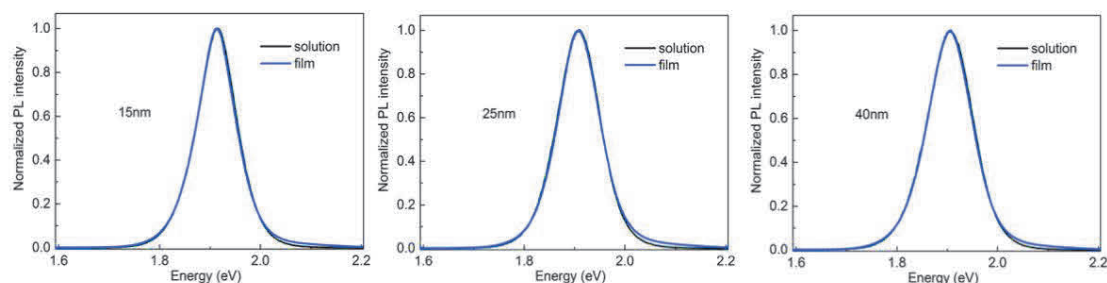


Figure 4.8 Photoluminescence spectra comparison of solution samples (black line) and film samples (blue line).

The accumulation time for photoluminescence and radioluminescence acuirements are set as 10s and 600s, respectively. The PL spectra were measured under a weak optical pumping at 405nm with a power of 3.5 μ W(unfocused). As show in Figure 4.9(black line), a single band was observed, which is attributed to the single exciton (X) peaking at 1.914eV(648nm), 1.908eV(650nm), 1.907eV(650nm), 1.906eV(651nm) for respectively the 15, 25, 30 and 40nm particles. In the case of X-rays excitation (35kV, 35mA on W anode), the RL spectra exhibit a blue-shifted shoulder, and as the size increases, a small blue shift of the maximum of emission is observed as the size increases (1.912eV, 1.912eV, 1.914eV and 1.917eV)(Figure 4.9(red line)). We attribute this blue-shifted shoulder indicated by the blue arrow to the multiexcitons emissions occurring under X-rays excitation contrary to weak intensity optical[78]. The shift increases with the increasing shell, might be caused by the discrepancy of the exciton-exciton Coulomb interaction in different sized particles[45]. In addition, we also think the difference at low energy side can be partially related to trap-related emission in larger NCs[141]. Considering intense photoexcitation and X-rays excitation, traps and defects are filled by a great amount of carriers, leading to a reduction of trap-related emission. Therefore, X-rays excitation differs from low power optical excitation which cannot generate multiexcitons.

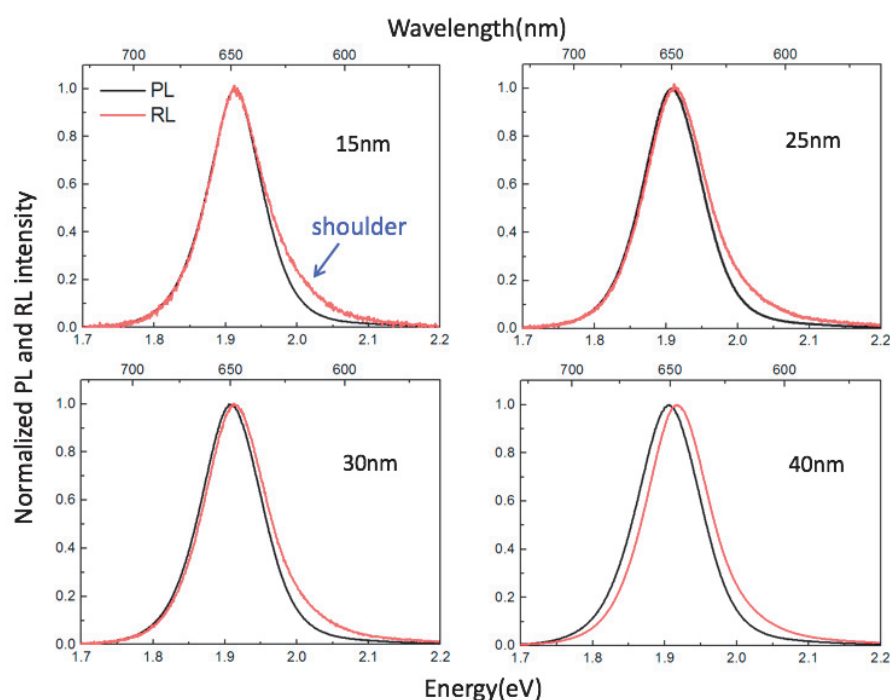


Figure 4.9 Steady-state PL and RL spectra of a series of drop-cast SQWs (15nm, 25nm, 30nm, 40nm). Excitation source: 405nm light emitting diode(black line) and X-rays illumination at a voltage of 35 kV (red line).

Since several studies have reported a rapid loss of emission intensity when the NCs was exposed under X-rays or γ -rays[74,142], it is necessary to examine the photostability of our samples under high energetic excitation. Here, we applied the above smallest and

largest (15nm and 40nm) SQWs for experiments to verify the photostability of the samples. The experimental conditions are the same as above. The samples are placed about 5 cm in front of X-rays output window, and irradiated with X-rays(35kV,35mA) for up to one hour, during which RL spectra of different irradiation times are acquired, and all the accumulation times are set to 400s to facilitate the comparison of emission intensity changes at different irradiation times. As illustrated in Figure 4.10, we did not observe any emission intensity degradation with the increase in irradiation time, even the relatively smaller 15nm SQWs show excellent photostability. This implies that the existence of thick-shell CdS achieves a well surface passivation, so that the sample is able to resist the photo-oxidation induced by ionizing radiation, thereby reducing the damage to the emission intensity. Since the accumulation time is 600s when the above steady-state RL measurements were performed, there is no need to consider the effect of degradation. And such a good photostability guarantees the reliability of the subsequent experimental results.

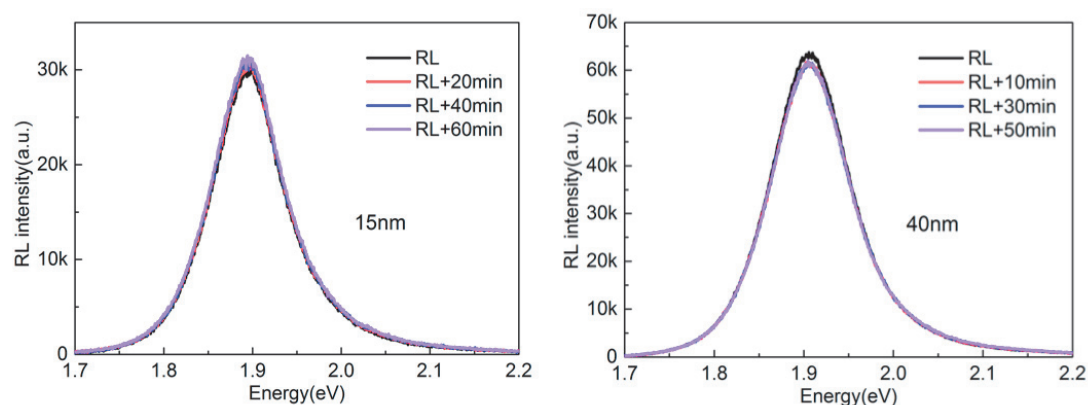


Figure 4.10 Emission intensity evolution with different X-rays illumination time of 15nm and 40nm SQWs. The X-ray images were recorded at a voltage of 35 kV. The accumulation time is 400s.

4.4 Photoexcitation

4.4.1 Photoluminescence decay curve measurement

Generally, steady state spectroscopy based on the ensemble samples does not enable the differentiation and observation of high order multiexcitons. In order to further figure out the specific excited state, we employ the time-resolved technique to observe the short-lived components and realize the spectral and dynamical analysis of multiexcitons under both pulsed laser excitation and X-rays excitation.

We first investigate the effect of shell thickness on the single exciton lifetime, by the mean of the decay curve measurement with 15nm-40nm SQWs. The excitation source is a Deltadiode from Horiba with the output light wavelength of 405nm and 100KHz repetition. The pulsed laser is defocused to avoid the formation of multiexcitons(the

photons absorbed per NC on average $\langle N \rangle \ll 1$). The decay curves are shown in the Figure 4.11(a). As the shell grows, the lifetime of exciton is continuously prolonged. The recombination rates strongly decrease in the larger NCs, which is consistent with the delocalization of the electrons into the shell, leading to a reduction of electron-hole wavefunction overlap[81]. The PL decay should theoretically be well fitted by an exponential function. However, for large particles, apparently multiexponentials are needed to fit the decay curves. For instance, 40nm SQWs, the lifetimes we extracted are approximately 40ns, 180ns and a very long time constant 990ns. Here, we make a hypothetical assignment of these lifetimes. First, we assign the longest lifetime to the trap-related delayed emission. It involves the capture of the charge carriers of the traps, and then a time-delay due to detrapping process, subsequently, the radiative recombination of the recovered carriers at $1S_{3/2}1S_e$ exciton state results in such a long lifetime.

Secondly, the assignment of time constant 180ns based on the reference[81], in which the single exciton of largest SQWs they prepared (15nm in diameter) is characterized with around 60ns lifetime. Owing to significant reduction of the electron-hole wavefunction overlap in our 40nm SQWs compared to the 15nm they studied, we can expect the increase in the single exciton, thus the time constant 180ns is assigned to single exciton. Due to the inevitable charging effect, the shorter time constant 40ns probably comes from the charged exciton. The fitted single exciton lifetimes of the ensemble samples are plotted in the Figure 4.11(b). Note that the single exciton of 15nm SQWs is around 35ns, which is a little smaller than the reported value 60ns. Compared to the one they reported with similar sizes (1.3/0.3/5.8nm), our samples (1.3/1.8/4.4nm) with a thicker CdSe emissive layer can lead to the increase in electron-hole overlap integral, which is responsible for the reduced lifetime. Additionally, we would like to point out delayed emission in large particles extends the lifetime of single excitons to a certain extent, so the fitted value may be overestimated compared to small particles.

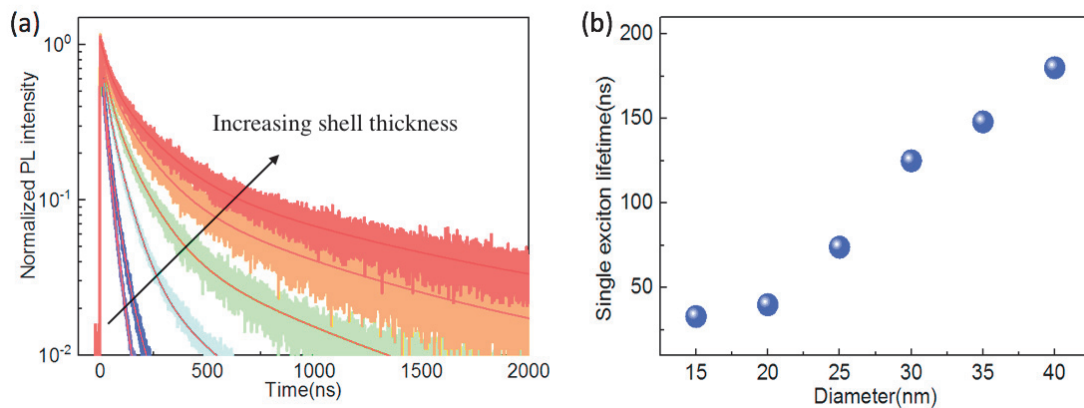


Figure 4.11 (a) PL decays of ensemble CdS/CdSe/CdS SQWs with varying shell thicknesses under low intensity excitation without focusing and wavelength filter. (b) Single exciton recombination lifetime for varying sized SQWs.

In the following section, we will focus on 15nm, 25nm and 40nm SQWs. To observe and analyze the dynamical evolution with varying excitation intensity, we first performed the decay curve measurement to record the decay kinetics of drop-cast 15 nm SQWs under different power photoexcitation, varying from 1nW to 35 μ W, the diameter of the laser spot is around 4 μ m. In Figure 4.12, the decay curves were recorded at three different energy positions on the spectrum, which is illuminated by a low power (a)($\langle N \rangle \sim 0.003$) and a relatively high-power photoexcitation (b)($\langle N \rangle \sim 4$). For low power, the PL spectrum is only composed of single exciton, although the detected wavelengths are different, the decay curves obtained are consistent, indicating that they are derived from the same excitation species recombination. When $\langle N \rangle$ is around 4, which makes sure the possibility to generate the multiexcitons, we observe significantly different decay behavior, where the proportion of fast components gradually increases with the blue shift of the detection position. At 2.14eV, the rapid decay is on the order of the instrument response (IRF). This indicates that there are different recombination pathways at these three positions, involving the formation of single, charged and multiexcitons. Next, we will discuss the spectra and dynamics of these excitation states in detail.

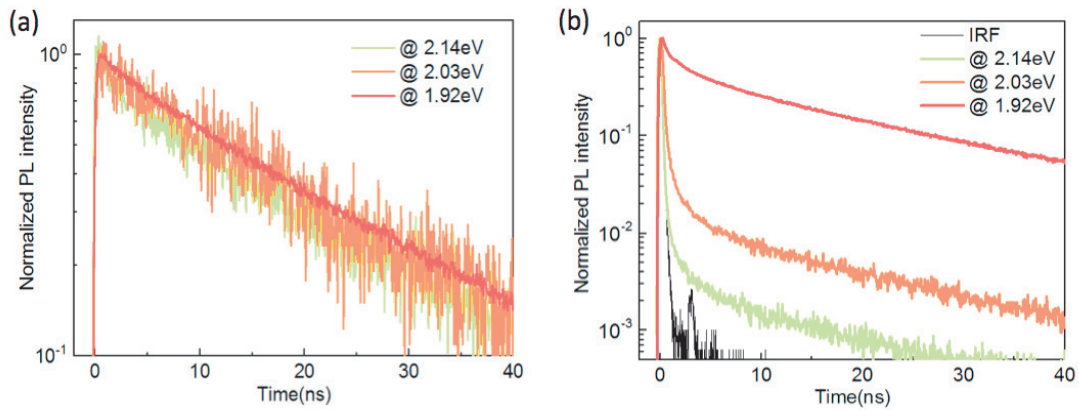


Figure 4.12 Decay dynamics measured at three different energy positions of a drop-cast 15nm diameter SQWs. (a) $\langle N \rangle \sim 0.003$, (b) $\langle N \rangle \sim 4$. Black curve in (b) is the instrument response function (IRF).

Since multiexcitons states can be generated at high pump powers by rapid successive absorption of multiple photons, the most common way to identify the excitation species is the analysis of their power-dependent properties. We focus on the dynamical signature at bandgap band ($\sim 1.9\text{eV}$) to identify the species specifically. The decay curves show the strong power dependence, as illustrated in Figure 4.13. Specifically, at low power, the photons absorbed per NC on average $\langle N \rangle \sim 0.003$ ensures that there is no formation of multiexcitons, emission should be almost exclusively from the single exciton state. However, because the charging effect in NCs is usually unavoidable, even when the excitation optical intensity is very low, the entire decay curve still has a part of the contribution from charged excitons. As the excitation power increases, we normalized the PL decay traces at 60 ns to match the long-lived single

exciton emission tail. We observe the emergence of additional fast components in the early time, corresponding to the multiexcitons. And the traces become indistinguishable at $t > 15$ ns, indicating that all of the multiexcitons have already decayed and only single exciton left in the rest of recombination process.

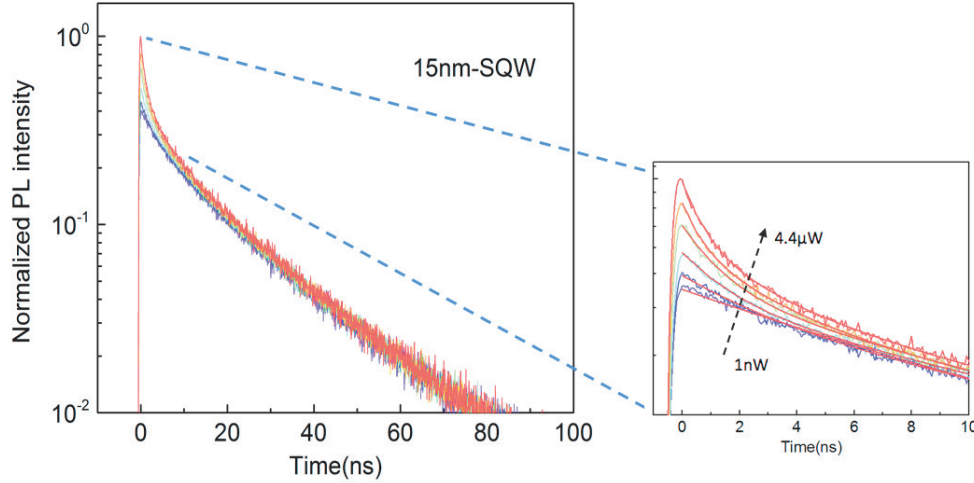


Figure 4.13 The PL decay curves of 15nm diameter SQWs under various excitation powers are normalized at 60ns to match the single exciton tail, highlighting the fast multiexcitons component at early time.

The method of extracting different excited states from the total time decay curve is based on the lifetime differences of these physical events. By exploring the spectral distributions and excitation power dependences, the excited states can be distinguished and assigned according to their unique spectral and temporal characteristics. Here, at lowest intensity excitation, the decay curve in Figure 4.13 exhibits two exponential dynamics by 12ns and 31.7ns lifetime. Based on our analysis above, these time constants can be assigned to the charged exciton and single exciton emission. There may be a slight difference in lifetime due to the size distribution of the NCs. This is because the sample is placed on the focused spot in this measurement. At high excitation power, in order to quantify the lifetime of multiexcitons, we subtract the contribution of single exciton obtained by scaling the curve measured for $\langle N \rangle \ll 1$, from the traces measured for high power, which allows us to isolate the purely fast components dynamics. As shown in Figure 4.14(a), we obtain the multiexcitons decay at the power of $1.6\mu\text{W}$ ($\langle N \rangle \sim 4$). The extracted dynamics can be fitted to a two-exponentials decay with 0.72ns and 3.14ns lifetimes. We also found that with the increase of excitation power, these lifetime components gradually decrease.

Next, in order to validate the assignment of the fast decay component to multiexcitons recombination, we plot the relation of fast component integral PL intensity in the first ns with respect to the power fluence, as illustrated in Figure 4.14(b). The analysis of power-dependent dynamics reveals the composition of the superposition peak, that is a mixture of various excited states. First, as we expected, the slow component

extracted at long-lived region (~100ns) where the fast multiexcitons has already recombined scales linearly with the laser intensity. This behavior is in agreement with the single exciton feature. On the other hand we observed a nearly quadratic (~1.88) dependence of the fast component integral intensity with respect to power, indicating the absorption of at least two photons within the same pulse by a single SQW. Thus on the basis of these measurements and analysis, the biexciton and higher order (>2) multiexcitons are characterized by 3.14ns and 0.72ns, respectively.

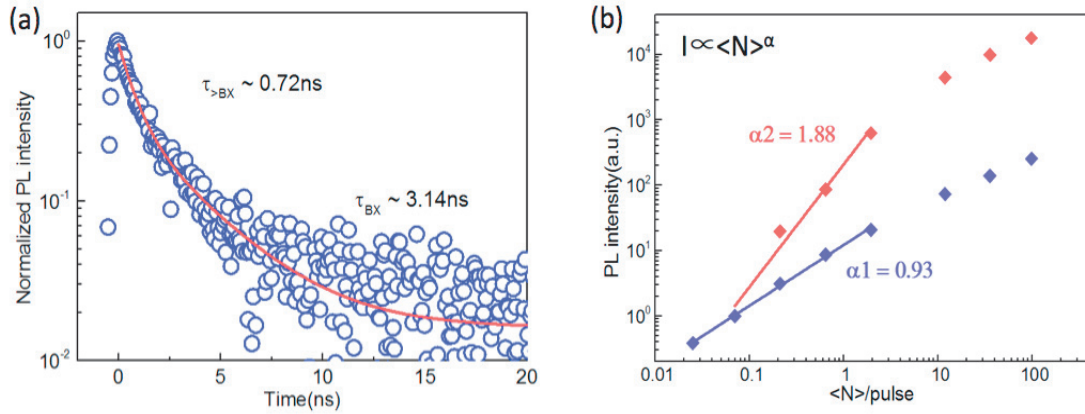


Figure 4.14 (a) Multiexcitons dynamics in 15nm SQWs obtained by subtracting the scaled single exciton contribution from high power decay ($\langle N \rangle \sim 4$), it can be fitted with two exponentials by 0.72ns and 3.14ns. (b) Power dependent integral PL intensity of fast component (red square) and slow component (purple square). Slow component shows a single exciton signature and the fast component follows an approximately quadratic dependence on power.

In order to elucidate the effect of shell thickness on the performance of multiexcitons, we further examine the power dependent PL dynamics at bandgap emission band of 25 nm and 40 nm SQWs with the same excitation conditions, as shown in Figure 4.15. To match the single exciton emission tail, we normalized the decay curves of various excitation fluences at 100ns and 250ns, which allows us to highlight the emission of multiexcitons. They show extremely different behavior in comparison with that of 15nm SQWs, especially the 40nm sample. At low pump level, the decay curve of 40nm SQWs predominates by a significantly long-lived single exciton (~180ns). The delocalization degree of the electron spatially decreases the overlap between electron and hole wavefunction, which is responsible for this low recombination rate. Besides, as the power enhanced, multiexcitons again emerge with considerably long lifetimes, the fast component is not completely decayed even at 100ns. Also, by fitting the decay curves at different powers, we have extracted the characteristic lifetimes of multiexcitons. As a summary, Table 4.2 shows the four types of excited states with different lifetimes for 15nm, 25nm and 40nm SQWs, and further gives the hypothetical assignments of each type.

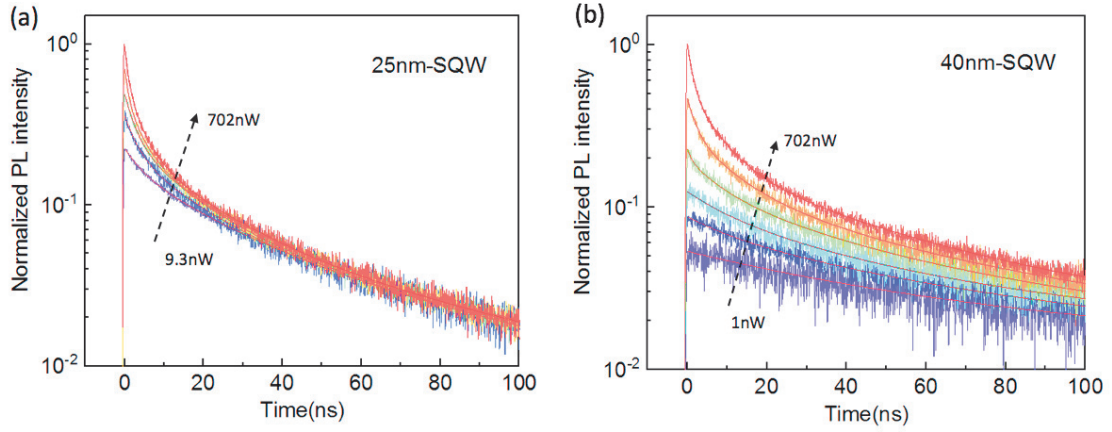


Figure 4.15 The PL decay curves of 25nm(a) and 40nm(b) diameter SQWs under various excitation powers are normalized at 100ns and 250ns to match the single exciton tail, compared to that of 15nm SQWs, the multiexcitons components are longer lived.

Table 4.2 Exponential fitting results and excitonic species assignment of 15 nm, 25 nm and 40 nm SQWs.

	τ_1 (ns)	τ_2 (ns)	τ_3 (ns)	τ_4 (ns)
15nm	31.7	12	3.1	0.7
25nm	74	21.3	4.3	0.9
40nm	180	40	10	1.2
Assignment	X0	X*	BX	>BX

The time constants are extracted at $\langle N \rangle \sim 4, 3$ and 3 for 15nm, 25nm and 40nm SQW, respectively.

According to the statistical scaling described by our earlier study[41], $\tau_{r,BX} = \tau_{r,X}/4$, using measured single exciton radiative lifetimes, we are able to estimate that the radiative lifetimes of biexciton, $\tau_{r,BX}$, are ~ 7.9 ns, 18.5ns and 45ns, respectively. Then we can calculate the quantum yield of biexciton are around 40%, 23% and 22%, which are similar with the values reported for alloyed NCs recently[4,143]. Contrary to our expectation, the biexciton quantum yield of large sized samples is relatively low. Since the delayed emission in large particles causes the lifetime of single exciton to be overestimated as we mentioned in section 4.4.1, we believe that the quantum yield of biexciton in large particles is underestimated here. Considering that the biexciton lifetime is composed of radiative lifetime and non-radiative lifetime, $\tau_{BX}^{-1} = \tau_{r,BX}^{-1} + \tau_{A,BX}^{-1}$ (here we neglect non-radiative decay channels other than Auger recombination)[144], for 15 nm SQWs, $\tau_{BX} = 3.1$ ns and $\tau_{r,BX} = 7.9$ ns, and we obtained $\tau_{A,BX}$ of 5.1 ns. And we also estimated the Auger lifetime of biexciton is 5.6ns and 12.9ns for 25nm and 40nm SQWs, respectively. Obviously, compared to the typical Auger recombination lifetime in NCs,

which is a few hundred picoseconds[34], it is extended by nearly up to two orders of magnitude in our samples. Similarly, we can conclude that the quantum yields of charged excitons are 76%, 58%, and 44%, respectively, and the corresponding Auger recombination lifetimes are 49ns, 50ns, and 72ns.

4.4.2 Time-resolved photoluminescence spectrum

In addition to the decay curve measurement to record the dynamics, in the thesis, time-resolved emission spectrum measurements were also employed to directly observe and analyze the changes in spectra with varying excitation intensity. First we performed the time-resolved PL spectrum measurement of drop-cast 15nm SQWs under the same optical excitation source(405nm) and intensity range, from 9.3nW to 35 μ W. In order to investigate the ultrafast recombination of multiexcitons, here we can extract the PL spectra of multiexcitons through integrated spectra at different time intervals. As presented in 4.16(a), the time-resolved PL spectrum were recorded when the incident laser is at a low power, approximately 9.3nW, corresponding to the average number of excitons formed per NC per pulse $\langle N \rangle \sim 0.02$. It is well known that multiexcitons in larger quasi-type II QDs induce the blue-shifted features (repulsive interaction) with respect to single exciton[37]. Here, from the time gated spectra comparison of early time and late time, we cannot observe the signature of blue-shifted emission under low intensity excitation. The identical spectra manifest the absence of the multiexcitons emission and also indicate the homogeneous of this sample. If the sample is polydispersed, a red shift should be observed due to the energy transfer from small to large particles[141]. In addition, almost no delayed emission was observed for 15nm SQWs, indicating that the sample is nearly trap-free, which is attributed to good surface passivation and release of interface strain.

When considering the high intensity optical excitation, the spectra evolution is significantly different. Here, we also performed the time-resolved PL spectrum measurements under higher power illumination with the same film sample. The power is around 35.78 μ W, corresponding to $\langle N \rangle \sim 90$. The time gated spectra are illustrated in Figure 4.16(b). Distinct emission features emerge in the early time at high energy side, and as the time increased, the features decay fast till disappear, leaving a single exciton spectral profile. These features are strongly power-dependent, which is the typical signature of multiexcitons.

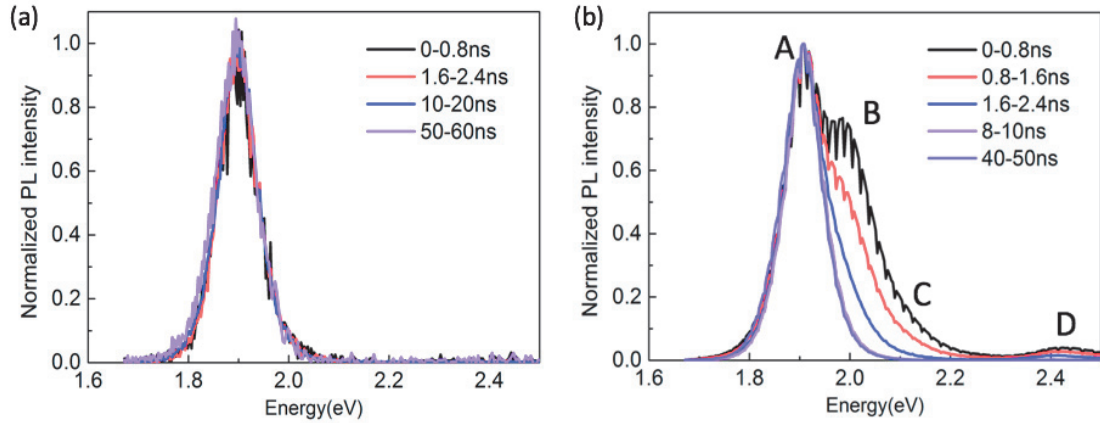


Figure 4.16 Comparison of time gated spectra corresponding to different time intervals of 15nm SQWs. (a) 9.3nW, (b) 35.78 μ W.

In order to further interpret these distinct features, we plot the comparison of first 800ps time gated spectra under different intensity excitation, as shown in Figure 4.17(a). Note that in general, the regular drops observed are due to a small oscillating jitter of unknown origin having a significant impact of the first channels. We are allowed to directly see the power dependence of the excitation species. The various emission features with significant different dynamics are observed in sequence as the excitation power progressively increases for 15nm sample, which are named as Peak A, B, C and D. According to the emission energy, the features can be divided into two types: core states emission and shell emission.

Here, on the basis of the lifetime fitting results from the decay curve measurements of 15 nm SQWs, we first give a spectral assignment to the features originating from core states. At bandgap peak (Peak A), compared to the single exciton spectrum (1.906 eV, late-time spectrum in Figure 4.17), there is around 6meV blue-shifted (1.912 eV). Generally, exciton-exciton interaction energy is on the order of 10meV in biexciton, thus we assign it to the superposition of charged exciton and biexciton. In addition, a pronounced emission peak at 1.98 eV (Peak B) and a third peak at around 2.11 eV (this peak is clearly distinguishable in larger particles in the following section, Peak C) can be seen. Considering the Coulomb effect of multi-carriers, the peak with 80 meV blue-shift relative to single exciton emission is assigned to 1S-1S transition involving states with more than four charge carriers[145], which has been proved the dominant pathway in multiexcitons[43], including charged biexciton, triexciton and higher order. In addition, partial multiexcitons can also be recombined by 1P-1P and 1P-1S transition[4], according to the research of Efros, Al. L. on CdSe NCs electronic structure[20]. We deduced that the higher feature at around 2.11eV originates from the P-level related emission. In comparison with 2nd derivative of absorption spectrum in Figure 4.17(b), the stokes shift of bandgap peak is around 50 meV, and the P-level peak stokes shift is also around 50meV. Finally, another band (Peak D) at around 2.4 eV have also been observed under high intensity excitation. Owing to position of Peak D closes to CdS bandgap energy,

here we assign it to shell-related optical transition[143]. When a large number of excitons presence in the nanoparticles, the electron–hole pairs recombine directly in shell states to emit high energy photons instead of thermal relaxation to core energy states.

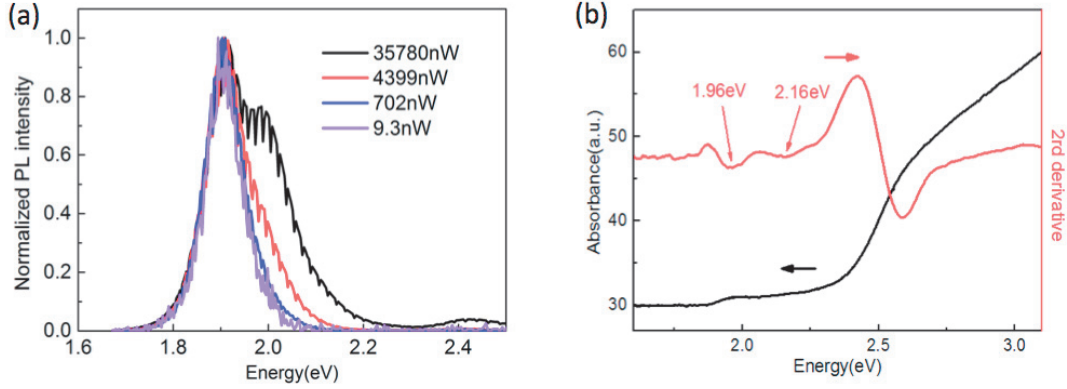


Figure 4.17 (a) Normalized time-resolved PL spectra in first 800ps as a function of power for drop-cast 15nm SQWs. The excitation wavelength is 405nm. (b) Absorption (black), and absorption second derivative (red) spectra of 15nm SQWs. The arrows mark the $1S_e-1S_h \rightarrow 1.96\text{eV}$ and $1P_e-1P_h \rightarrow 2.16\text{eV}$ transitions.

We also carried out the time-resolved PL spectrum with 25nm and 40nm SQWs under the same laser power range. The time gated spectra of the highest power excitation are shown in Figure 4.18 (a, c): we can also observe the four distinct emission bands, originating from multiexcitons recombination. The feature shift with respect to the single exciton is summarized in the Figure 4.18(b). Compared to that of 15nm SQWs, the blue shift of each peak increases with the shell increasing. Peak A in 15nm SQWs is almost at the same spectral position as the single exciton peak (only 6meV shift). However, for 25 nm and 40 nm SQWs, this shift is approximately 20 meV and 30 meV, respectively. The shift of Peak B is around 95 meV and 102 meV, and Peak C is blue shifted by around 240 meV and 260 meV. The reason for the trend of the higher energy in comparison to the single exciton for the largest SQWs is that the delocalization of the electrons over the shell region increases with an increase in the shell thickness, this results in a more type II like behavior companied by the increase in the exciton-exciton repulsive interaction[45,146]. This measurement is very sensitive to the focusing, slight deviation will make a strong effect on the ratio of the excitonic species, not on the peak position.

Besides, significant long-lived emission can be seen from the time gated spectra with a slight broadening on the red side of the spectra at late time in Figure 4.18 (d), this delayed emission has been demonstrated as the trap-related emission. Since the spectrum of the delayed emission is similar to the single exciton, it can be explained that delayed emission is the result of recovery of trapped carriers and emission from $1S_{3/2}1S_e$ exciton state. Usually, the delayed emission peak position exists slight redshift compared to the typical exciton, indicating the possibility of carrier trapping in smaller NCs is less likely than in the larger ones which might have more traps[141].

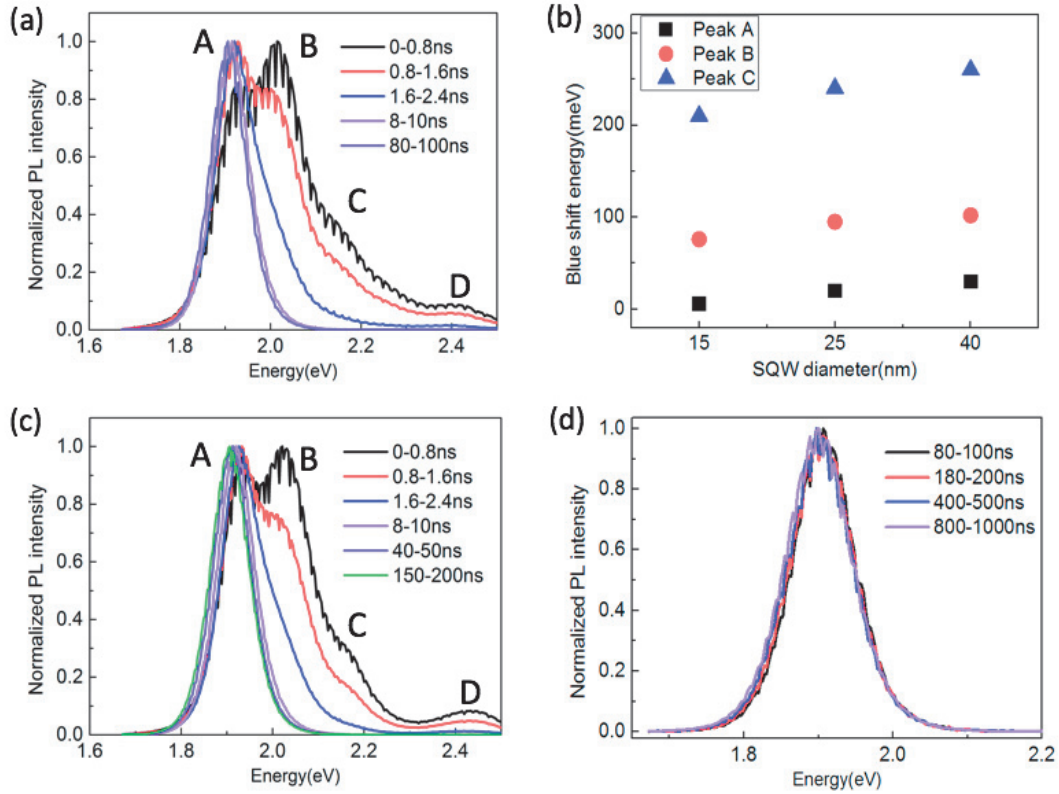


Figure 4.18 (a, c) Comparison of spectra corresponding to different time intervals of 25 nm and 40 nm SQWs at power $35.78 \mu\text{W}$. (b) The energy shift of the different peaks with respect to single exciton peak for 15 nm, 25 nm and 40 nm SQWs. (d) Delayed emission at the late time of 40 nm SQWs.

Figure 4.19 presents the comparison of total emitted photons between low (black line) and high (red line) power excitation, which are consistent with the steady state PL. As we expected, the spectral profile under high power excitation is analogue to that under X-rays excitation, that is, a shoulder is observed on the blue edge, involving the formation of multiexcitons and, as the shell thickness increases, the spectrum under intense photoexcitation shows a slight blue shift around 3 meV, 6 meV and 12 meV for 15 nm, 25 nm and 40 nm SQWs, respectively. These observations reveal the energy recombination under X-rays radiation might undergo the similar process with that of intense photoexcitation. Meanwhile, it also points out that to compare the photoexcitation is a feasible way to investigate the excited state in radioluminescence. Therefore, in the following section we will further give the decay curve and time-resolved RL spectrum under X-rays excitation, and then explore the composition of its emitted light through comparative analysis.

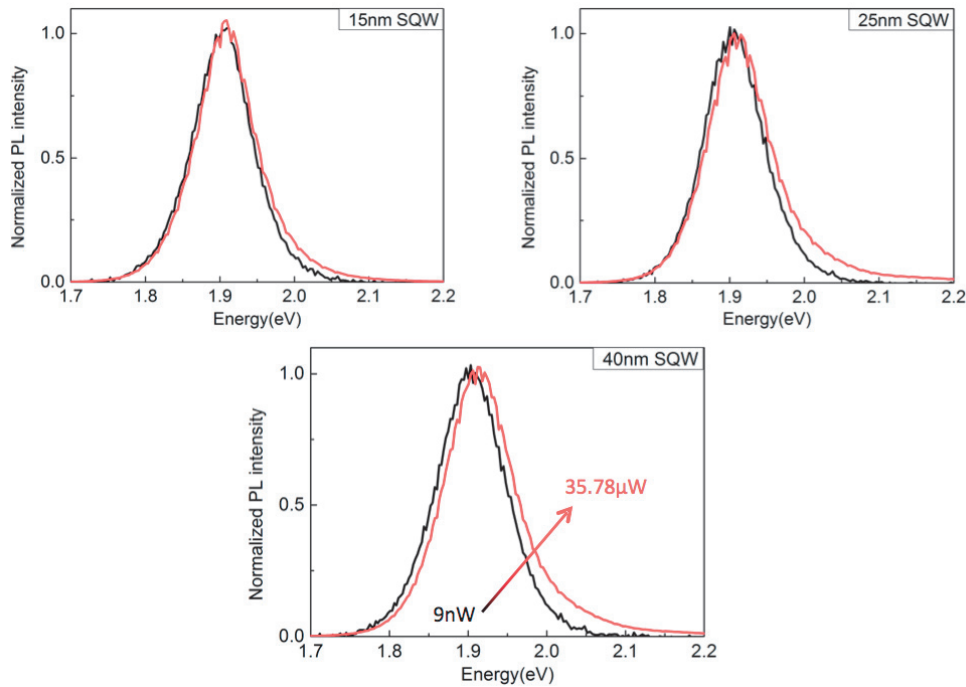


Figure 4.19 Integrated total photons under low(black line) and high(red line) power excitation of 15nm, 25nm and 40nm SQWs.

4.5 X-rays excitation

In this sub-section, in order to investigate the excitonic behavior under ionizing radiation, similarly to optical excitation we carried out the time-resolved measurements with X-rays excitation (acceleration voltage 30kV on W anode). Through the comparison with the photoexcitation, we qualitatively analyzed the dynamical and spectral properties of excited states under X-rays excitation.

First, as shown in Figure 4.20, we recorded the decay curves at three different emission wavelengths of 15nm SQWs. To acquire the signal with a good signal to noise ratio, the integration time is set to 3600s because of the weak signal due to the low X-rays energy absorption by the very thin layer of particles. The multi-exponential curve indicates the emission might be composed of several different excitonic species or experience quenching. Besides, a drastic change in the time response can be also observed under X-rays excitation as a function of the emission wavelength. Consistent with intense optical excitation, as the wavelength decreases, the curve decays more and more rapidly. This reveals that different types of recombination processes might occur at short-wavelength positions, which might be the signature of high order excitons presence.

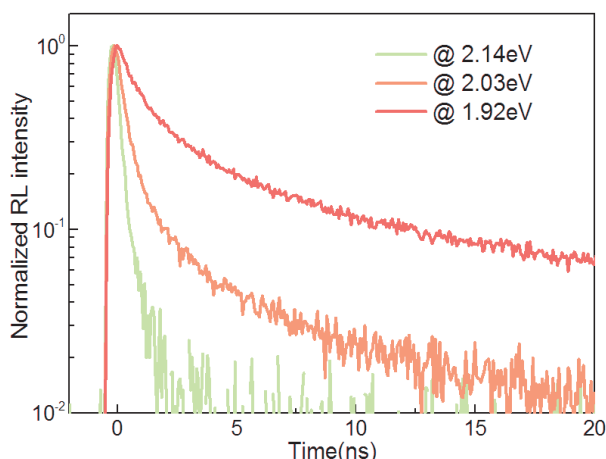


Figure 4.20 Decay dynamics measured at different energy of 15nm sample. Excitation source: X-rays illumination at a voltage of 30 kV.

4.5.1 Time-resolved radioluminescence spectrum

Separating emission both spectrally and temporally allows us to observe multiexcitons features. The same strategy is thus used to highlight and compare X-rays induced multiexcitons emissions at short time. First, temporal evolution of the emission spectra of the samples after the pulsed X-rays excitation is given in the Figure 4.21. This measurement is set to 400s/point in order to obtain an acceptable signal to noise ratio. And the slits of the monochromator are opened four times larger(1mm) than that of photoexcitation (0.25nm). As can be seen in the Figure 4.21, it shows similar trends to intense optical excitation for all the particles. This observation is consistent with the response of catholuminescence in nanocrystals reported by Lazaro A. Padilha[14,147].

Because of the weak signal, we use here 0-2ns time gate width instead of 0-0.8ns. Although the different emissive features are not as easy to distinguish as that of the 0-0.8ns interval, we still observed a significant spectral broadening on the blue edge at early time. The emission peak at 2.0eV and 2.4eV can still be clearly identified, and another weak emission band is between 2.1-2.2eV. Then the blue-shifted peaks gradually disappear as time passes after the excitation pulse hits the sample, indicating their fast decay dynamics. At longer time gates, the spectrum shifts towards longer wavelengths by different energy over time. Similar to the photoexcitation, we compare the shift of the bandgap peak with respect to single exciton position for three samples, which are approximately 6meV, 22meV and 27meV for 15nm, 25nm and 40nm, respectively.

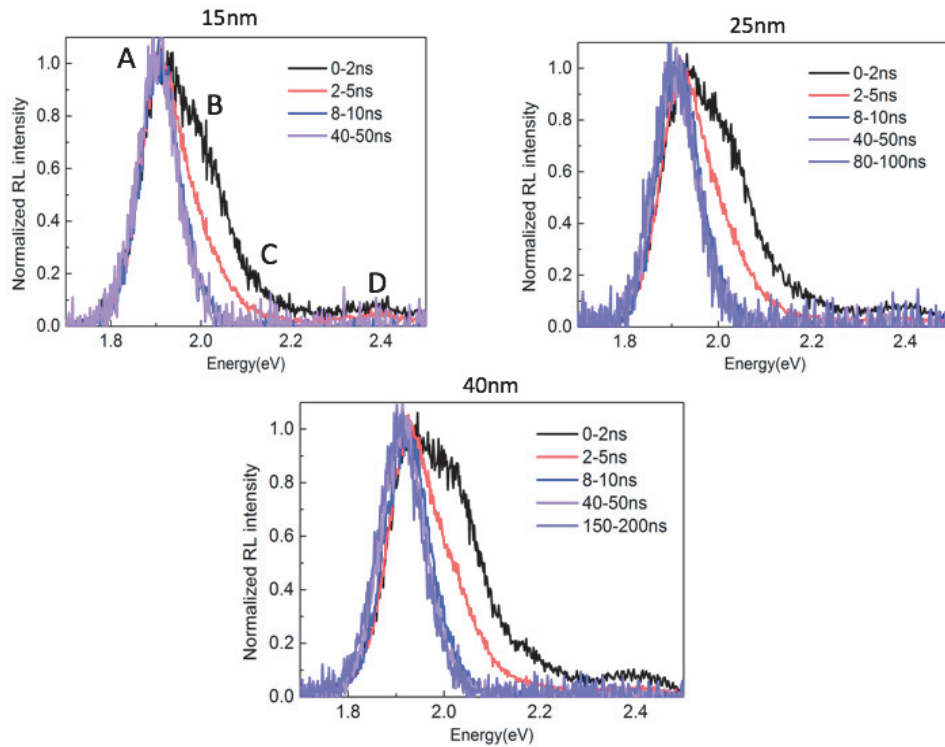


Figure 4.21 Comparison of time gated spectra corresponding to different time intervals of 15nm, 25nm and 40nm SQWs under X-rays excitation. Excitation source: X-rays illumination at a voltage of 30 kV.

It is instructive to directly compare the RL and PL data for all sized particle. We compare the first 2ns emission under X-rays and intense optical excitation ($35.78\mu\text{W}$) to highlight the fast component features as illustrated in Figure 4.22. We clearly see the similar spectral profiles under the two excitations, the difference just lies in the ratio of each excitation state. Based on this remarkable spectral similarity between PL and RL, we are able to assign these features to the multiexcitons under X-rays excitation, including charged exciton and biexciton emitted near the bandgap, and the ultrafast emissive bands raised from S-level transition and P-level transition involving the multi-carriers (>4). These observations imply that as we predicted, during the secondary electron energy relaxation process, the electron-electron elastic scattering, carrier multiplication and Auger ionization play an important role, promoting the formation of considerable electron-hole pairs and making SQWs occupied with high-order excitation species.

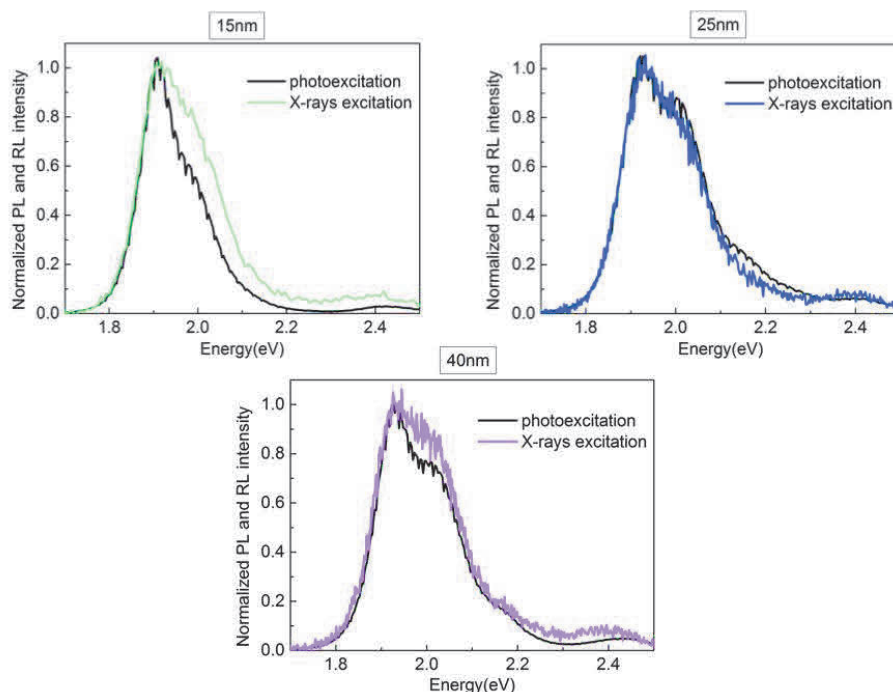


Figure 4.22 Comparison of time gated spectra at 0-2ns interval for 15nm, 25nm and 40nm SQWs under X-rays excitation with high intense photoexcitation. Excitation source: X-rays illumination at a voltage of 30 kV and the laser power is 35.78 μ W.

4.5.2 Radioluminescence decay curve measurement

In order to further confirm the assignment of excitonic species, we employ the time-resolved technique to record the decay dynamics under X-rays excitation for three samples. Before this, for comparison, we first performed the decay curve measurement of the optical excitation in the non-focused condition to ensure that there is no formation of multiple excitons. At the same time, the non-focusing situation is similar to X-rays irradiation (non-focused as well) regarding the particle size distribution, that can be then ignored.

Figure 4.23 illustrates the comparison decay dynamics under X-rays and low power photoexcitation of 15nm, 25nm and 40nm SQWs. Both of the curves are measured without wavelength selection, including all the possible decay pathways for excited states. First, as we can see, the similar trend at relatively long time allows us to normalize the curves, we normalized the curves at 60ns, 100ns and 200ns respectively, and the results are analogous to the normalization under different power excitation. The good match at the tail fully shows that single exciton recombination is the final state of the whole recombination process. Second, similar to high power light excitation, the obvious extra fast components can be observed under X-rays excitation, and the multi-exponential curve reveals that there is not only one type of exciton. In addition, the fast component exhibits a strong size dependence in terms of decay time. As the particle size increases, the decay rate becomes significantly slower. For 15nm SQWs, the fast components

completely decay after 20ns, however in 40nm SQWs, until 150ns there are still a part of emitted photons that do not originate from single excitons.

Next, we try to fit the decay dynamics by multiexponential in order to extract the fraction of extra fast signal from X-rays excitation reflecting the multiexcitons generation. First, according to the fitting results we discussed above, by fixing the charged exciton and single exciton lifetime, the PL decay curves are well fitted, we also extracted an additional long-lived component, delayed emission. Afterwards, by fixing single exciton lifetime or subtracting the contribution of single exciton from the decay curve measured for X-rays, we are allowed to extract dynamics of the fast components. The fitting curves are shown in the Figure 4.23(red curves). The specific fitted parameters are given in Table 4.3. Here, we need to point out that the fastest parameter reaches the response function of the instrument. For 15nm sample, the fast components dynamics of RL decay curve are characterized by the 0.6ns, 2.6ns and 8.5ns lifetimes. These time constants are close to lifetime signatures extracted under intense pulsed laser excitation in Table 4.2 with a slight decrease. As we mentioned above, the extracted multiexcitons lifetimes gradually decrease with the increasing power, so this can be the interpretation for the slight discrepancy. Based on our analysis, we are able to assign the time constants in the Table 4.3, in where τ_1 and τ_2 are single and charged exciton, and then τ_3, τ_4 are the lifetimes of multiexcitons: biexciton and higher order.

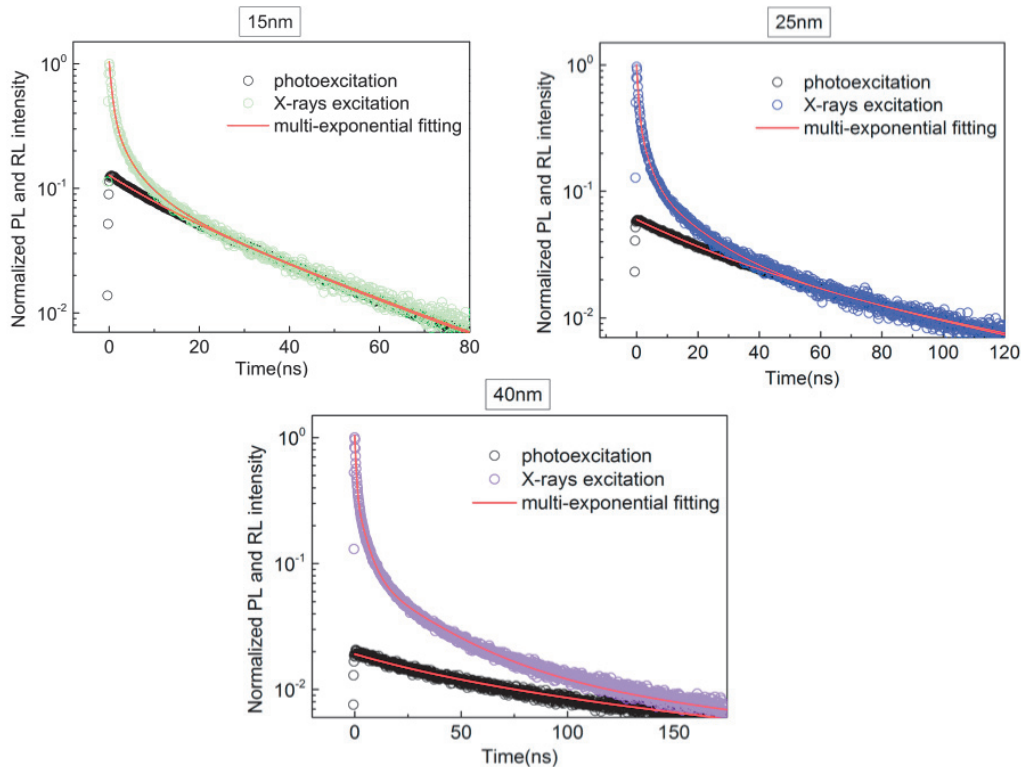


Figure 4.23 Comparison of the decay dynamics under X-rays and photoexcitation of 15nm, 25nm and 40nm SQWs(defocusing). Red curves are the multiexponential fitting.

Table 4.3 Summary of the fitting parameters for decay dynamics under X-rays excitation of 15nm, 25nm and 40nm SQWs.

	$\tau_1(\text{ns})$	$\tau_2(\text{ns})$	$\tau_3(\text{ns})$	$\tau_4(\text{ns})$
15nm	29	8.5	2.6	0.6
25nm	75	18.3	3.6	0.6
40nm	180	35	4.8	0.7

Finally, we discuss the ratio of excited states in different sized samples under X-rays excitation. In order to compare with the theoretical simulation, here we will focus on analyzing the ratio of each excitation species to single exciton, $A_i\tau_i/A_X\tau_X$, where the A_i represents the amplitude of the excitonic species, τ_i is the lifetime. Considering that there are delayed emission photons in the emission spectrum, especially for large particles, which is ignored in the model, here we replace the single exciton with the sum of the single exciton and the delayed emission photon. Because the delayed emission mainly comes from the trapping and detrapping process of carriers, and the carriers trapping before the occurrence of carrier multiplication can result in a decrease in the number of multiexcitons. Therefore, we estimate that the ratio of multiexcitons we obtained should be smaller than the simulation.

Table 4.4 The ratio of different excitation species to single exciton for different sized SQWs, the data extracted from the fitting of RL decay curves in Figure 4.23.

	15nm	25nm	40nm
X*/X	0.29	0.50	0.55
BX/X	0.22	0.30	0.33
MX/X	0.13	0.13	0.11

Table 4.4 shows the specific fraction of different excitonic species to single exciton in varying sized SQWs. First, compared with the simulated values in Table 4.1, there is a quite significant difference in the ratio of charged exciton, which becomes dominant in comparison with multiexcitons. The simulation does not take the particle charging due to defects into account. However, the actual synthesized NCs always present a certain number of defects on the surface or within the particles, which is unavoidable. Moreover, due to the more defect states in the large-sized particles, this discrepancy is more significant, which is consistent with the large amount of delayed emission in the 40nm

SQWs. For biexciton, with the increase in particle size, the ratio increases slightly, but not obviously, which shows the conformity with the simulation results. We believe that the absence of size dependence is due to the fact that the average deposited energy of each particle is quite high after X-rays excitation, resulting in very little influence caused by size, and that Auger quenching becomes the dominant process. Since the lifetime of the higher order excitons is limited by the response function of the instrument, we will not discuss it in detail in this thesis.

4.6 Conclusion

In this chapter, the scintillation response of SQWs under X-rays excitation is analyzed using steady-state spectroscopy and time resolved technique. We mainly achieved the identification and quantitation of the excited states under X-rays excitation by comparing temporally and spectrally the recombination produced following high intense photoexcitation with X-rays ionizing radiation.

First, according to the unique temporal and spectral characteristics of different excited states, we realized the assignment of the excitonic species for intense optical excitation. Based on the extracted characteristic lifetime of each excited state, we calculated the quantum yield of biexciton up to 40%, indicating that SQWs have excellent performance in suppressing Auger recombination. The remarkable spectral similarity between PL and RL enables us to analyze the distribution of the RL spectrum. Combined with the analogous decay dynamics, we demonstrated that under X-rays excitation, all observable emission can be attributed to recombination between states within the quantum-confined NCs, including single exciton, charged exciton and multiexcitons. This conclusion reveals that carrier recombination plays an important role in the relaxation process. Secondly, we simulated the evolutions in the proportion of each excited state with respect to the size of the particles under X-rays radiation. The comparison between the experimental and theoretical value consistently shows that under the excitation of high-energy rays, the proportion of excited states has no obvious size dependence, as observed in the decay time analysis and time resolved emission spectra, which may be the result of the large amount of energy deposited per NC on average. We suggest that Auger quenching is dominating when high order multiexcitons are produced in the confined structure which are in principle favored for larger sizes.

Chapter 5

Scintillation properties of hererostructural II-VI nanoplatelets under X-rays excitation

With their appealing properties, colloidal nanoplatelets have become highly promising for many applications. Their ultrafast exciton recombination rate caused by the giant oscillator strength transition received a lot of attention on the radiation detection field[10,78], together with large absorption cross section and suppressed Auger recombination of heterostructures make 2D NPLs potential scintillating materials.

Similar to SQWs, in this chapter we aim to describe the scintillation properties of NPLs under X-rays excitation *via* steady state spectroscopy and time resolved technique. We also compare the behaviors of excited states under intense laser excitation spectrally and dynamically to analyze the scintillation performance of different heterostructural NPLs as a function of the morphologic aspects, including core/crown, core/shell and core/crown/shell.

5.1 Sample preparation and stability

The first step is to obtain efficient luminescence in NPLs by optimizing the quantum yield. The extended lateral area increases the interaction between NPLs as they form into a film, resulting in the stronger Forster resonance energy transfer (FRET) compared to the conventional QDs[148]. Assisted by FRET, the possibility of charged carrier trapped by the defects considerably enhances, leading to rapid non-radiative recombination and significant decrease in photoluminescence quantum yield. In order to obtain bright film samples, we thus need to minimize the influence of the FRET on the optical properties. Owing to FRET distance sensitivity, to increase the spatial separation of the NPLs core should be the efficient method to avoid the FRET. Here, we take the core/shell NPLs as an example and prepare a NPLs-in-polymer sample. Specifically, the 5 mL NPLs was precipitated and redispersed in 1mL toluene which is beneficial to the dissolution of PMAO (poly maleic anhydride-alt-octadecene), 50 mg PMAO powder was added to keep the volume fraction of NPLs less than 2% in the polymer matrix[148]. Then the solution was placed on a silicon substrate via the drop-casting method. To exclude the self-reabsorption effect, only one drop(12 μ L) was used to form an around one square centimeter film.

For comparison, we also prepared a core/shell NPLs film with the same quantity of particles but without the mixing of the polymer. The PL spectra of two film samples were acquired in the same condition: illuminated by 405 nm low intensity diode and accumulated for 10 s. As illustrated in Figure 5.1(a), we observed more than 50% PL intensity decrease for the pure core/shell NPLs compared to the one embedded in polymer. Furthermore, a slight red shift (around 1nm) can be seen in the pure core/shell NPLs spectrum, which is similar with the FRET signature of conventional QDs[149]. It can be interpreted by the inhomogeneous size broadening, favoring the energy transfer toward the particles with smaller band gap. Since the inhomogeneous broadening is induced by the shell growth for NPLs, the FRET of core NPLs with near-perfect monodispersity is usually not accompanied by red shift of PL spectrum[150].

We also compared the time resolved decay curves of two film samples, as shown in Figure 5.1(b). In order to avoid the generation of multiexcitons, this measurement was performed under a very low power pulsed laser with 405nm excitation wavelength. We fixed the detected wavelength at maximum of PL spectrum. We observed that with the addition of the polymer, the recombination rate became slower, suggesting the fraction of the rapid non-radiative recombination decreased. Therefore, along with the enhancement of the PL intensity, we concluded the presence of polymer spatially separates the NPLs particles, and then effectively impedes the FRET between them.

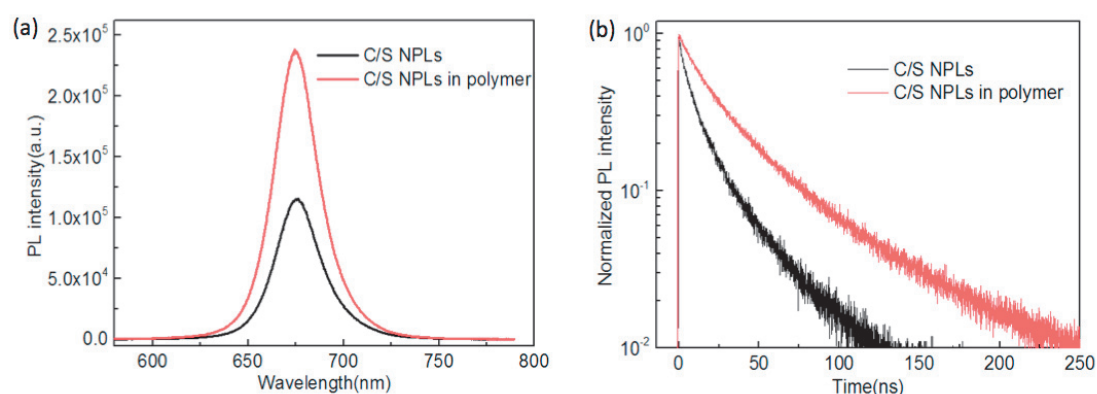


Figure 5.1 Comparison of the optical properties between core/shell NPLs film(black line) and core/shell NPLs in polymer film(red line). (a) PL spectra recorded under low intensity optical excitation. (b) PL decay curves of the peak wavelength excited by low intensity pulsed laser to avoid the formation of multiexcitons.

Similar to SQWs, we also tested the stability of NPLs under X-rays excitation (35 kV, 35 mA, sample at 5 cm). Here, we continuously illuminated the core/shell NPLs (thickness ~4 nm) for around 2 hours and recorded the RL spectra at different times, 15 min, 30 min and 100 min, as presented in Figure 5.2. Under long-term ionizing radiation, unlike SQWs, NPLs exhibits a certain degree of instability. We observed a gradual decrease in the RL intensity, wherein only 9% reduction can be seen for 30 min radiation, up to around 19% reduction for 100 min radiation. In this chapter, for the steady state

measurements, we set the accumulation time as 400s which is much shorter than 30 min, thus the influence of RL spectra degradation should be very small. For time resolved RL measurements, the X-rays intensity is generated by 30 kV voltage and 0.3 μ A current, which is around 10^5 times lower than that in steady state measurement. The acquisition time is usually set as one day which corresponds to ~ 9 s in the case of 35 mA current. Therefore, we also don't need to consider the degradation of luminescence intensity in time-resolved RL test.

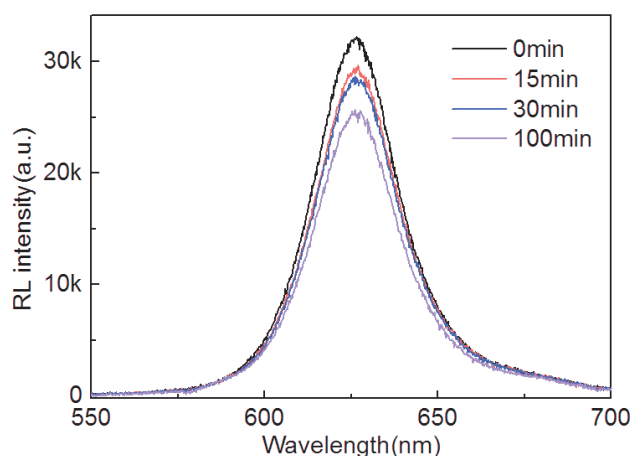


Figure 5.2 Radioluminescence spectra of C/S NPLs for different illuminated time. Excitation source: X-rays generated by 35kV voltage and 35mA current.

5.2 Core/crown CdSe/CdS nanoplatelets

5.2.1 Steady state radioluminescence

As they are promising fast time response radiation detection material, we will first discuss the scintillation behavior of core/crown NPLs. First, the PL spectrum was measured with 405nm diode (unfocusing, $\sim 3.8\mu$ W). Owing to the only lateral direction crown coating, the PL line shape should be highly homogeneous, we thus fit the PL spectrum with Lorentzian function, as shown in Figure 5.3(a). However, the spectrum is not well fitted, indicating the presence of a slight size distribution. Then for comparison, Figure 5.3(b) plots the fitting curve with Gaussian function, which is always related to spectrum consisting of an inhomogeneous broadening. As we can see, due to the broadening induced by polydispersity is weak, the Gaussian function cannot be the best option for the fitting. Hence, in the following section, the spectra are fitted by the sum of the Lorentzian and Gaussian line shapes.

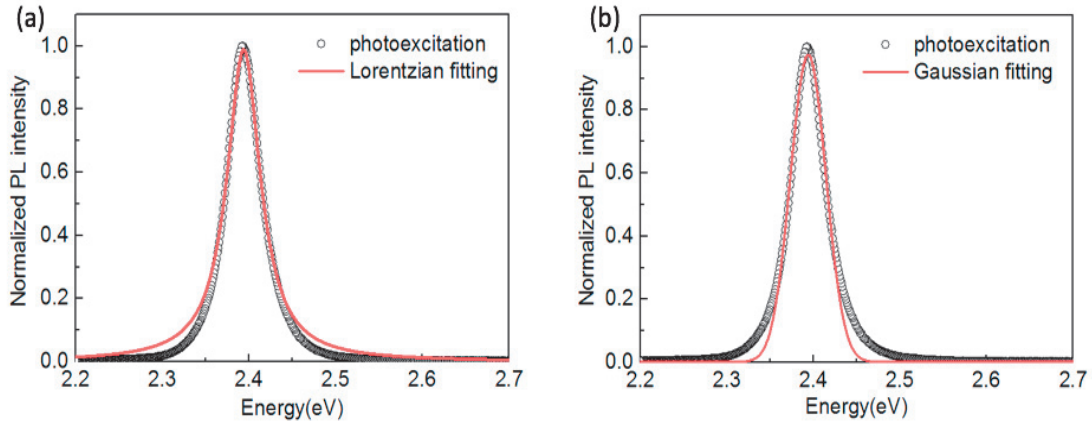


Figure 5.3 The photoluminescence spectrum is fitted by two different functions. (a) Lorentzian fitting, (b) Gaussian fitting.

Comparison between PL and RL spectra is shown in Figure 5.4(a, b). The profile in the left panel shows a spectrally symmetric photoluminescence at low optical excitation, which arises from the single exciton emission, and a broadening on the red edge with respect to the PL spectrum can be observed under 35 kV X-rays excitation (right panel). The red shift has been previously reported under intense optical excitation, which is referred to the emission of biexciton[151].

Here, to identify the excitation species with the red shift, we fit the PL and RL spectra using a pseudo-Voigt function, as depicted in following function,

$$y = y_0 + A \left[m_u \frac{2}{\pi} \frac{w_L}{4(x - x_c)^2 + w_L^2} + (1 - m_u) \frac{\sqrt{4 \ln 2}}{\sqrt{\pi} w_G} e^{-\frac{4 \ln 2}{w_G^2} (x - x_c)^2} \right] \quad (5-1)$$

Where the second term is the sum of Lorentzian and Gaussian line shapes with relative contributions m_u and $1 - m_u$ and widths w_L and w_G respectively. A is the amplitude.

As shown in 5.4(a), the PL spectrum at low power is well fitted by the single pseudo-Voigt function V_1 , the energy of symmetric peak is around 2.39eV with 47meV line width. In the Figure 5.4(b), we needed a sum of two pseudo-Voigt functions $y = A_1 V_1 + A_2 V_2$ to fit the RL spectrum. The parameters obtained from above V_1 fitting are held constant for RL spectrum fitting, and V_2 which represents the second emission peak is fixed as the same line shape with V_1 . And then the second peak energy is obtained at 2.36eV, as shown in the green line of Figure 5.4(b). The difference between two peaks energy is the result of exciton-exciton Coulomb interaction, about 30meV binding energy. For 2D nanocrystals, the ratio of the binding energy of the heavy hole biexciton to that of the heavy hole exciton is found to be 0.2, and nearly independent of well width[152]. The exciton binding energy for 4ML NPLs is demonstrated to be approximately

210 meV[153]. Therefore, theoretical prediction of the biexciton binding energy of our sample should be around 42 meV. Here, we can conclude that a biexciton emission under X-rays excitation is present. Furthermore, the slightly smaller red shift (~10meV) compared to the prediction indicates the occurrence of other types of multiexcitons emission. Because the Stokes shift of C/C NPLs is very small, it will lead to strong self-absorption. The red-shifted multiexcitons band is beneficial to reduce the influence of self-absorption and conduce to practical application.

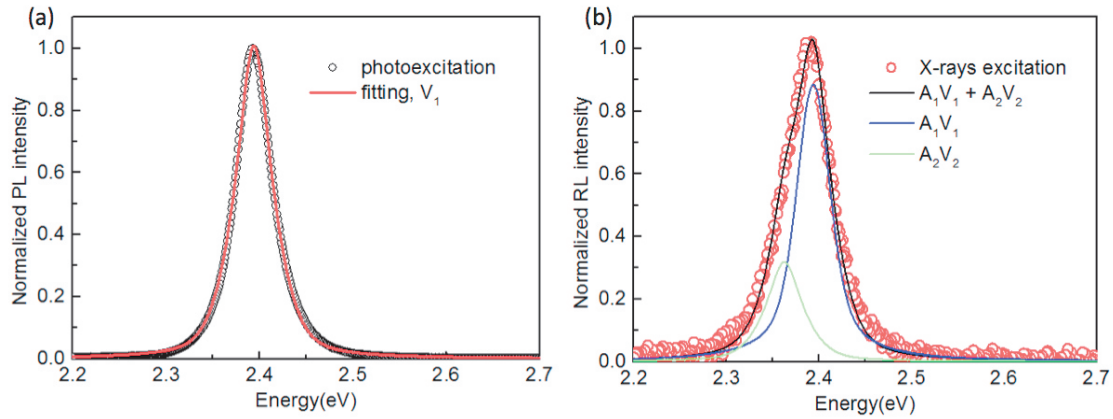


Figure 5.4 The comparison between PL and RL spectra and their fitting line shape with pseudo-Voigt function. PL was measured at low power to avoid the multiexcitons generation. (a) PL spectrum shows a single symmetric peak. And the RL spectrum is fitted by the sum of two components, $y=A_1V_1+A_2V_2$, the corresponding fitting of V_1 (blue line) and V_2 (green line) are also shown in the Figure(b).

5.2.2 Time-resolved measurements

Figure 5.5 shows the normalized time-resolved RL spectra using different time intervals, early time (0–0.8 ns) and later time (4–6 ns) after the excitation pulse. The pulsed laser emits at 405 nm with 500kHz repetition rate, and the X-rays illumination at a voltage of 30 kV voltage leading to a 0.3 μ A current. Since the low signal for X-rays excitation, spectrum was taken with a 1mm spectrometer entrance slit to improve light collection, which leads to a broader spectrum compared to the steady state one shown in Figure 5.4(b). The accumulation time is around one day, corresponding to 400s/point. Although there is a lot of noise in the spectral line, from the figure we can clearly see that at late time, the emission peak of this time interval is obtained at ~2.39eV, which is well in correspondence with the single exciton of low power photoexcitation. The early time gate(0-0.8s) is emitted at 2.37eV, a red shift of 20meV compared to the late time emission, which is consistent with signatures of multiexcitons emission observed in steady states RL. And the multiexcitons have already decayed at 4ns.

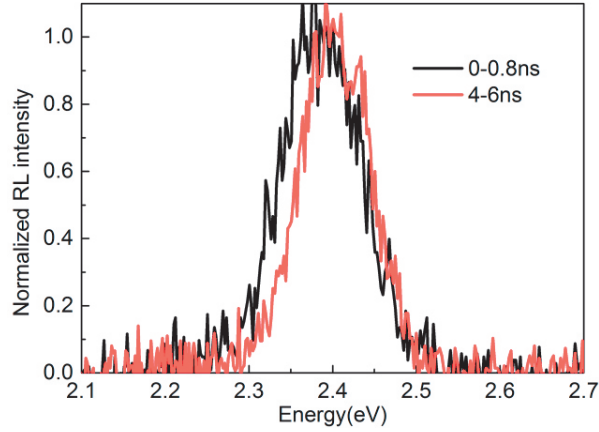


Figure 5.5 Normalized time resolved RL spectra of different time intervals, early time (0–0.8 ns) and later time (4–6 ns) spectra reveals a red-shifted spectrum at early times, pointing toward multiexcitons generation under X-rays excitation. X-rays illumination at a voltage of 30 kV voltage and 0.3 μ A current.

Using time resolved technique, we performed the decay dynamic measurement for core/crown NPLs under X-rays and low-intensity laser excitation, as depicted in Figure 5.6. The excitation source is the same as above. Here, the decay under photoexcitation was measured at unfocusing position (23 μ W/cm²) in order to facilitate comparison with X-rays. First, tri-exponentials function is applied to fit the curve of photoexcitation. The multiexponential behavior has normally been observed in ensemble and individual NPLs at room temperature[89,154]. This shows that the several possible recombination pathways might exist in the NPLs. The amplitude-averaged lifetime is often calculated as $\tau_{avg} = (\sum A_i \times \tau_i) / \sum A_i$, where τ_i is the lifetime and A_i is the corresponding amplitude. The τ_{avg} under photoexcitation is around 1.56ns. The specific fitting parameters are given in the Table 5.1. For X-rays excitation, we observed a similar trend on the long tail of the decay curve. Through fixing the longest lifetime parameter, we also fit the curve with tri-exponentials, and the τ_{avg} is calculated as 0.75ns. The faster decay is attributed to the formation of multiexcitons. The lifetime we obtained is longer than that in the literature [10], which should be the result of the trap related emission in our NPLs.

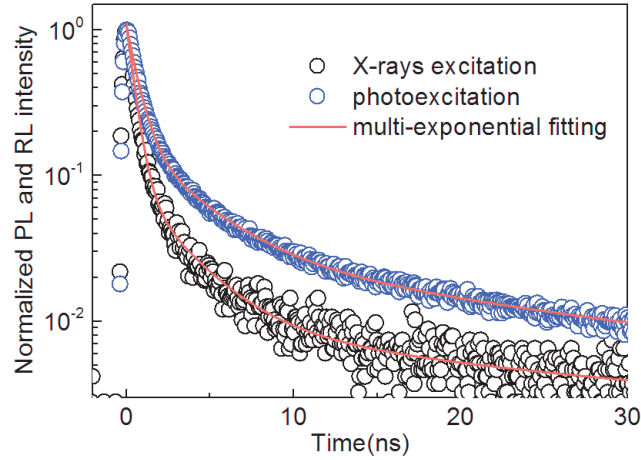


Figure 5.6 Normalized time-resolved fluorescence decay curves of CdSe/CdS core/crown NPLs under photoexcitation ($23\mu\text{W}/\text{cm}^2$) (black circle) and X-rays excitation (blue circle), red line is the tri-exponential fitting curve. Photoexcitation is measured by defocusing of 405nm pulsed laser (repetition: 500kHz) to avoid the multiexcitons.

Table 5.1. Summary of the fitting parameters for tri-exponential decay, lifetimes with corresponding amplitudes for core/crown NPLs under laser and X-rays excitation. The average lifetimes: $\tau_{\text{avg}} = (\sum A_i \times \tau_i) / \sum A_i$, were calculated by using the respective amplitudes of each component.

	$\tau_1(\text{ns})$	A_1	$\tau_2(\text{ns})$	A_2	$\tau_3(\text{ns})$	A_3	$\tau_{\text{avg}}(\text{ns})$
photoexcitation	0.63	0.89	3.37	0.15	20.86	0.03	1.56
X-rays	0.44	0.99	2.79	0.08	20.8	0.01	0.75

5.3 Core/shell CdSe/CdZnS nanoplatelets

5.3.1 Steady state radioluminescence

Due to the effective protection from the surrounding environment through the coating of the shell, the core/shell NPLs has demonstrated the improvement of chemical stability and quantum yield [130,155]. On the other hand, although part of the quantum confinement is relaxed due to vertical growth, compared with spherical QDs, it exhibits a faster characteristic lifetime. At present, there are few analyses on the scintillation properties of the core/shell NPLs structures. A full understanding of different types of NPLs is helpful to provide more selectivity for practical applications. Therefore, here we study the core/shell CdSe/CdZnS NPLs with different shell thicknesses. The samples are prepared by dropcasting the mixture of NPLs and polymers on the silicon substrate, the effect of the polymers is to reduce energy transfer among the particles. At the same time,

the quantity of particles dropped is required to be low to avoid the influence of self-absorption on the spectral lines.

We first performed the steady-state PL and RL spectra measurements, as shown in Figure 5.7. We compared the normalized spectra of the three samples with different shell thickness named as core/shell_s, core/shell_m and core/shell_l for 4ML, 5ML and 12ML shell, respectively. The power of the photoexcitation is always kept very low and unfocused to ensure that the resulting spectrum corresponds to the spectral profile of single excitons. As we can see, the three samples emit at 2.01eV, 1.96eV and 1.84eV, respectively. The red curves in the figure are the RL spectra, measured at an accelerating voltage of 35kV. Under X-rays excitation, the emission spectrum of core/shell NPLs shows the similar profiles with single exciton emission spectrum of PL. However, as the thickness of the shell increases, we observed an emission band on the blue side. It behaves on the opposite to the red multiexcitonic emission band of core/crown NPLs. It shows that the interactions between the excitons of core/shell NPLs are different from that of core/crown configuration. In addition, this band shows a size dependent behavior, that is, the feature becomes distinct as the shell grows. In order to analyze the origin of this emission band, we have conducted time-resolved research on the samples, presented in the next section.

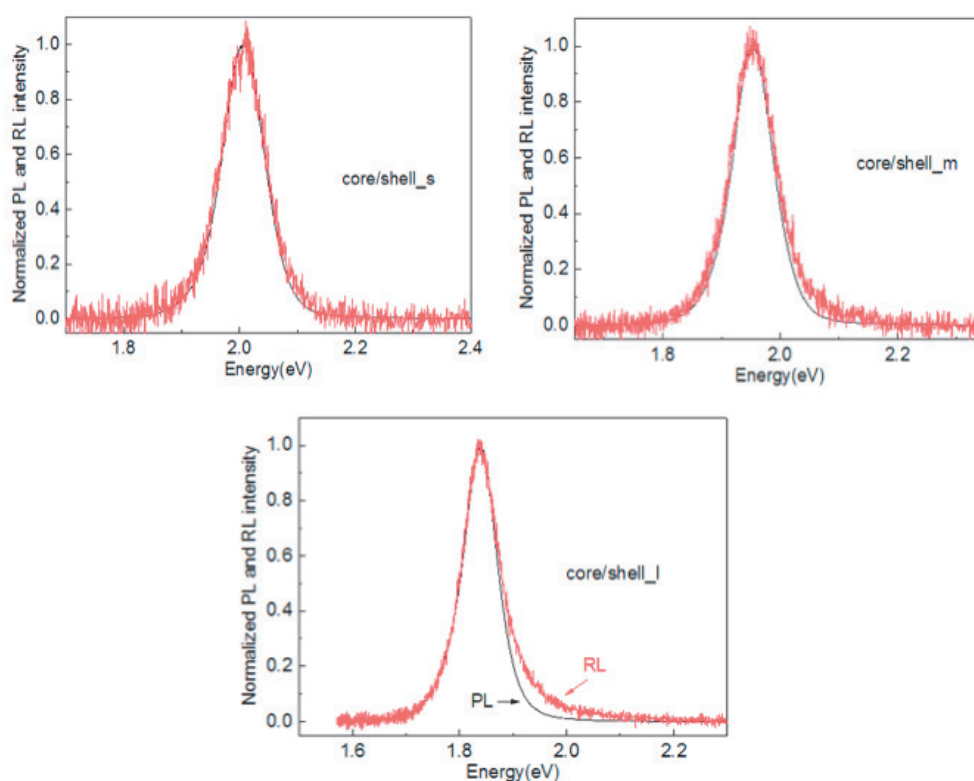


Figure 5.7 Normalized steady state PL and RL spectra comparison of core/shell CdSe/CdZnS NPLs with varying shell thickness.

5.3.2 Time-resolved measurements

Using time-resolved technique, we first focused on the characteristic lifetime of the three samples with different shell thicknesses. The same as the above experimental conditions, low-intensity photoexcitation and the sample is in a defocused position, therefore, the influence of multiexcitons is excluded. As shown in Figure 5.8, first, the decay curves of the samples are all multi-exponential, which is common in NPLs as mentioned above. Multiple complex channels of excitons, including single exciton radiative recombination, trap recombination and non-radiative recombination are considered as the origin of this multiexponential behavior[156,157]. The core/shell structure sample we used has a reported quantum yield close to unity[130], which contradicts the existence of a large number of non-radiative recombination pathways. Here, we think the reason is that we are studying the thin film sample, in which the reduced distance between particles promotes the energy transfer between them, and the probability of charged carriers being trapped by defects is greatly increased, which leads to non-radiative recombination. Although the addition of polymers can reduce the energy transfer effect to a certain extent, it cannot achieve 100% elimination.

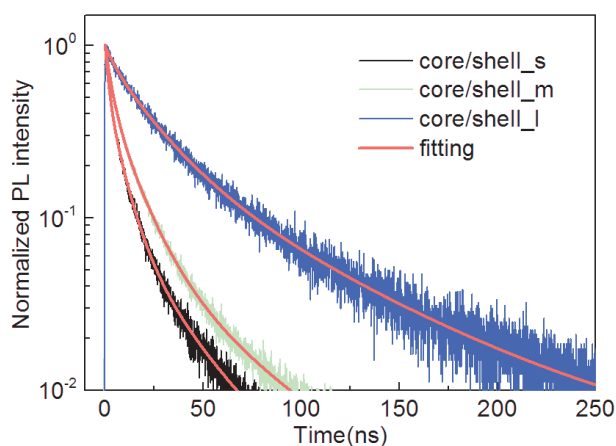


Figure 5.8 Normalized fluorescence decay curves of CdSe/CdZnS core/shell NPLs with different shell thickness in polymer under low intensity photoexcitation (defocusing), red lines are the tri-exponential fitting curves.

Secondly, based on the multiexponential fitting, we calculated the amplitude average lifetime, which are around 7.6 ns, 10 ns to 33 ns, respectively. We can observe that the lifetime gradually increases with the growth of the shell thickness, which reflects that the relaxation of the quantum confinement as the shell increases makes the reduction of the wave functions overlap of electrons and holes. Besides, the fraction of long-lived component $A_3\tau_3$ is large in core/shell_l, suggesting the presence of an increase in trap-involved delayed emission, and the traps usually arise from the lattice misfit defects in thick shell nanocrystals. The specific fitting parameters are shown in Table 5.2.

Table 5.2 Summary of the fitting parameters for tri-exponential decay, lifetimes with corresponding amplitudes for core/shell NPLs with different shell thickness under low intensity photoexcitation and the calculated average lifetimes.

	$\tau_1(\text{ns})$	A_1	$\tau_2(\text{ns})$	A_2	$\tau_3(\text{ns})$	A_3	$\tau_{\text{avg}}(\text{ns})$
core/shell_s	2.57	0.56	10.56	0.41	52.88	0.04	7.63
core/shell_m	3.44	0.53	13.4	0.44	60.01	0.04	10.34
core/shell_l	12.24	0.38	33.74	0.48	103.05	0.1	32.55

To provide further insight into the emission kinetics of various sized core/shell NPLs, we also measured the power dependence of the decay dynamics using time-resolved spectroscopy. This allows us to analyze the multiexcitons dynamical process in the core/shell structure. Here, we mainly focused on the decay curves near the maximum of emission peak, which are 2 eV, 1.94 eV and 1.82 eV respectively. The excitation laser source is 405 nm with 100kHz repetition, the power range is measured from 0.07 μW to 33 μW , and the size of the laser spot is approximately 4 μm in diameter. Figures 5.9(a-c) summarize the power dependence curves of three samples. The traces of PL decay under varying power are normalized for a long time (~ 20 ns) to highlight the fast component. We can clearly see that all the decay curves are well matched in the long tail, which indicates that the recombination of same excited state species takes place at this time. Similar with the fitting results in defocusing case, three different time constants are needed to fit the curves at low power excitation, and the observed slight deviation is caused by the size distribution of particles.

In addition, under high-power excitation, we can clearly observe the emergence of fast components, which decay rapidly. The fast components obtained by multi-exponential fitting are around 0.7ns, 0.9ns and 1.8ns. The obtained fast component lifetime is slightly higher than the typical Auger recombination lifetime(hundreds of ps), suggesting the reduction of Auger effect owing to the alloyed shell[158]. Additionally, with the power increases, the lifetime of the fast component decreases gradually, as summarized in Figure 5.9(d). In 2D nanocrystals, different with QDs, the exciton is delocalized in the particles instead of being confined. and the rate of Auger non-radiative pathways highly depends on the initial density of the excitons generated after laser excitation or the inter-exciton distance. For intermediate power, spatially separated excitons have to diffuse before encountering and recombination. The increasing power induces the increase in the density of excitons, leading to the decrease in the inter-exciton distance. The decrease in the diffusion time is responsible for the acceleration of the recombination rate. When we consider high power excitation, the excitons can recombine before diffusion, thus the recombination is usually on the order of ten ps[31]. However,

time resolved technique is not able to analyze such a fast lifetime. We do not discuss it here. The specific fitting parameters are shown in Table 5.3-5.5.

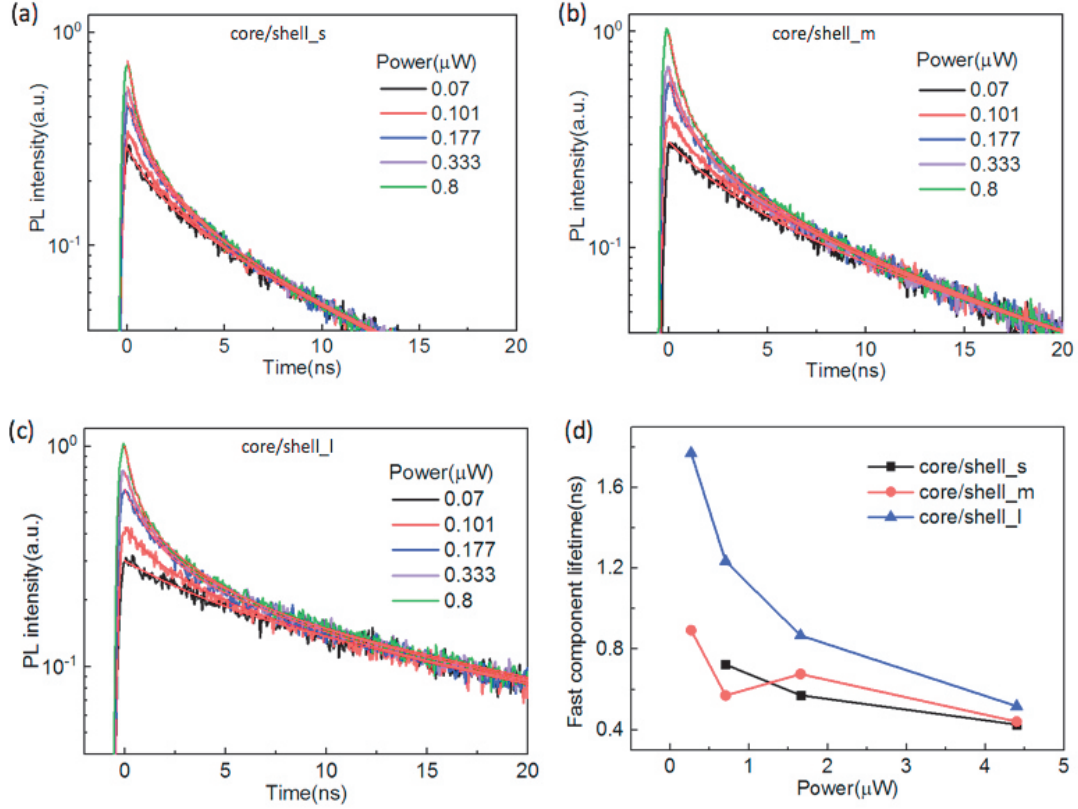


Figure 5.9 (a-c) Power dependent PL decay trace of core/shell NPLs with varying shell thickness, the traces are normalized at long tail to match the single exciton, highlighting the fast components arising at intense optical excitation. (d) The fitting lifetimes of the fast component as a function of power.

Table 5.3 The fitting parameters for tri-exponential decay for core/shell_s NPLs under varying power excitation.

Power(μ W)	τ_1 (ns)	A ₁	τ_2 (ns)	A ₂	τ_3 (ns)	A ₃	τ_4 (ns)	A ₄
0.07	33.2	0.02	7.89	0.14	1.61	0.12		
0.101	33	0.02	7.16	0.16	1.19	0.16		
0.177	33	0.01	9.42	0.11	3.11	0.15	0.72	0.2
0.333	33	0.01	8.82	0.12	2.46	0.17	0.57	0.25
0.8	33	0.02	8.12	0.14	1.96	0.21	0.43	0.37

Table 5.4 The fitting parameters for tri-exponential decay for core/shell_m NPLs under varying power excitation.

Power(μW)	τ_1(ns)	A₁	τ_2(ns)	A₂	τ_3(ns)	A₃	τ_4(ns)	A₄
0.07	39.87	0.02	11.24	0.16	2.63	0.13		
0.101	40	0.02	12.56	0.14	3.93	0.15	0.89	0.1
0.177	40	0.02	11.14	0.16	2.77	0.21	0.56	0.18
0.333	40	0.02	11.43	0.15	3.06	0.2	0.68	0.28
0.8	40	0.03	10.08	0.19	2.2	0.29	0.44	0.46

Table 5.5 The fitting parameters for tri-exponential decay for core/shell_1NPLs under varying power excitation.

Power(μW)	τ_1(ns)	A₁	τ_2(ns)	A₂	τ_3(ns)	A₃	τ_4(ns)	A₄
0.07	94.83	0.02	22.83	0.16	4.49	0.12		
0.101	94	0.02	25.44	0.13	7.88	0.12	1.77	0.15
0.177	94	0.01	25.58	0.14	6.31	0.18	1.23	0.3
0.333	94	0.02	23.96	0.16	4.94	0.22	0.87	0.36
0.8	94	0.02	20.86	0.19	3.21	0.3	0.52	0.48

In order to further verify the origin of the fast component, taking core/shell_1 as an example, we plotted the relationship between the PL intensity of the slow and fast components with the excitation power, the slow component is extracted from the decay curve Figure 5.10(a) at 60 ns, where the fast component is fully decayed. And the fast component is isolated by subtracting the contribution of the single exciton from PL intensity at 0 ns, as shown in Figure 5.10(b). We can see that the slope of the slow component as a function of power is about 0.7, which is less than the expected 1. Here we think that the reason is the intense laser has caused the degradation of the sample. Although the presence of polymer can alleviate a part of the degradation, it still induces an inevitable negative influence on the emission intensity. In addition, the fast component increases nonlinearly with the increase in power, which is the signature of multiexcitons emission. However, the obtained slope value is only 1.3, greater than 1 but less than 2,

which is the characteristic of biexcitons with power. The reason of the smaller slope might be the degradation.

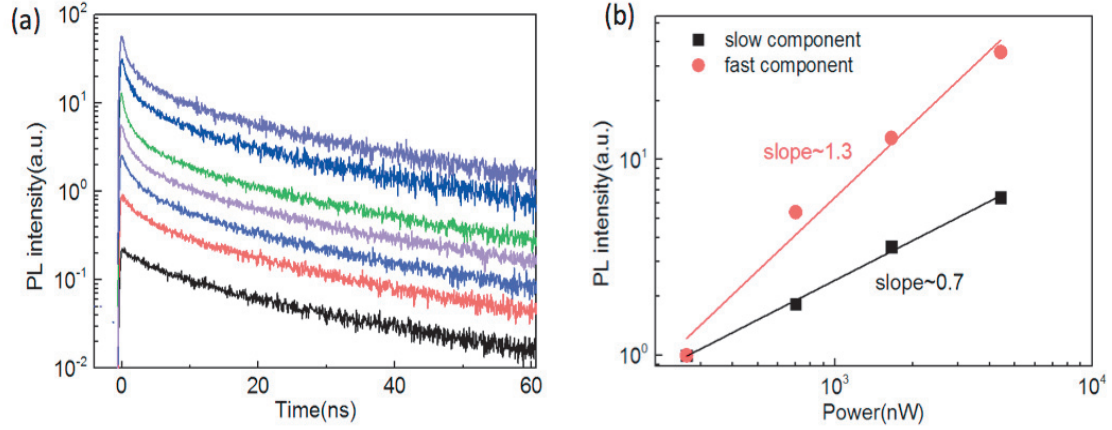


Figure 5.10 (a) Decay dynamics at main peak of core/shell_1 NPLs for varying power intensity. (b) The evolution of PL intensity as a function of power: slow component is extracted from (a) at 60ns and fast component is the PL intensity at 0ns after subtracting the contribution of single exciton.

In order to investigate the types of excited states under X-rays radiation, we then compared the decay kinetic curves under photoexcitation and X-rays excitation. The curves are measured without wavelengths selection. The decay under photoexcitation is obtained in the case of defocusing (the same with Figure 5.8), and the laser power is kept very low to avoid the formation of multiexcitons. As presented in Figure 5.11, we normalized the two decay curves at the long time: 20 ns, 25 ns and 40 ns respectively. As a result, all the decay curves under X-rays excitation can well match the photoexcitation traces at the long tail, which indicates that these two different excitations produced the same type of long-lived excited state. In addition, the curves under X-rays excitation has an additional fast decay component, which is similar to the decay dynamics under intense light excitation. Based on the similarity, we speculate that the fast component is caused by the formation of multiexcitons.

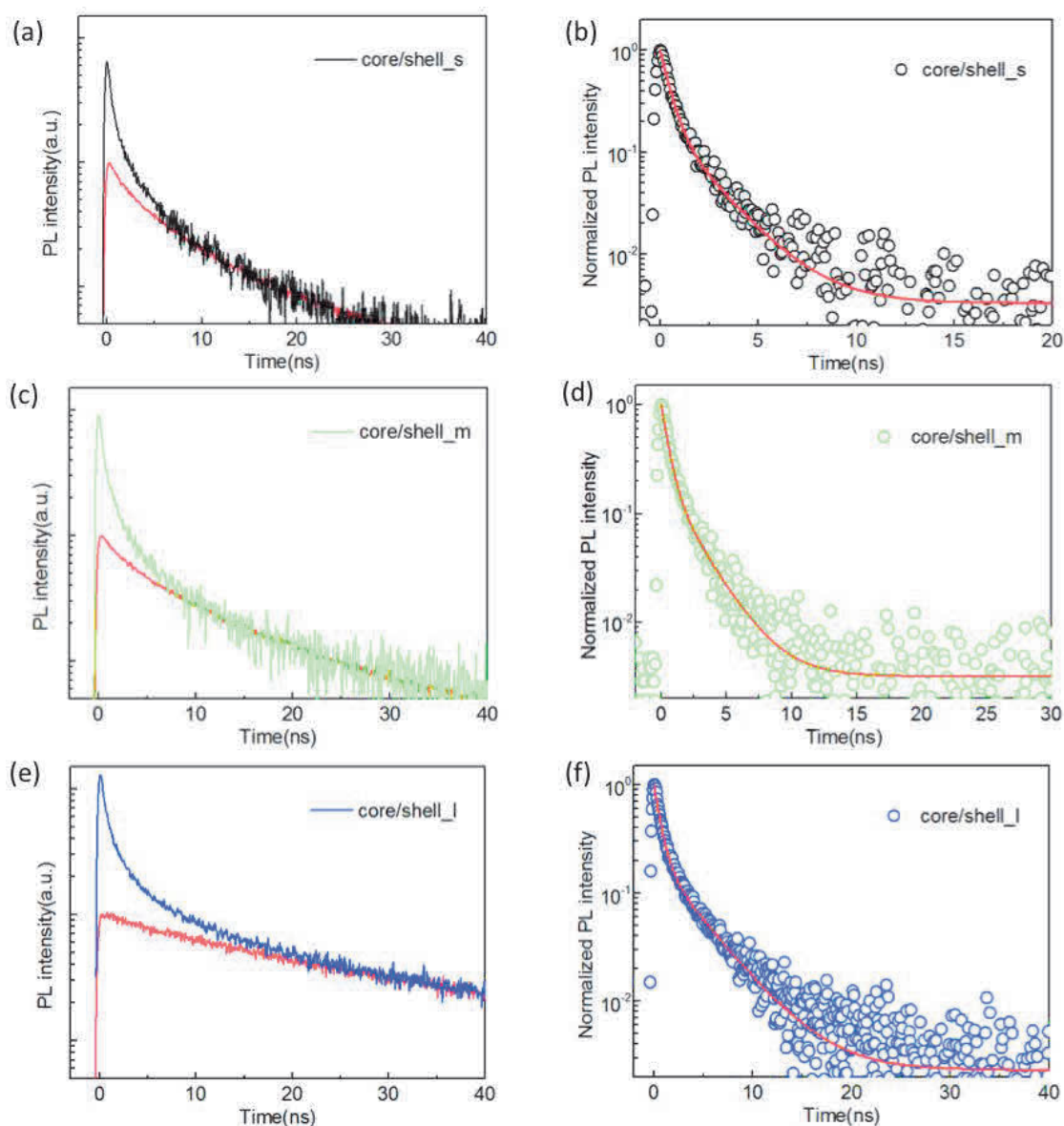


Figure 5.11 RL and PL decay curves of core/shell NPLs with varying shell thickness. (a,c,e) normalized at long time, highlighting the multiexcitons component. (b,d,f) The fast components of different sized core/shell NPLs for X-rays excitation, obtained by subtracting the single-exciton decay. The red curve in (b,d,f) shows biexponential fitting.

In order to quantitatively analyze the fast component under X-rays excitation, we subtracted the light excitation curves from the decay curves under X-rays excitation to obtain a pure fast component. Through fitting, we obtain that the fast components are characterized as 0.51ns, 0.54ns and 0.64ns respectively, and this time constant has reached the response function of the instrument. The specific fitting parameters are shown in Table 5.6, and the obtained time constants all correspond to the fitting time under intense light excitation in Table 5.3-5.5. The slight deviation in the data is due to

the size distribution of the samples. This consistent decay kinetic curve further demonstrates temporally that the similar types of excited state are generated under X-rays irradiation, namely, multiexcitons through the carrier multiplication process. We can see that compared to core/crown NPLs, the average decay time is larger.

We calculate the fraction of the fast component using $A_1\tau_1/(\sum A_i \times \tau_i)$, 24%, 26%, 13% for core/shell_s, core/shell_m and core/shell_l, respectively. Different with steady state spectra, no obvious size dependence of multiexcitons can be observed, especially for the core/shell_l. We think the decrease in the fraction might be attributed to the capture of carriers by the defects in larger particles. For steady state measurement, the defects can keep being filled by the continuous illumination of X-rays, the filling states result in the reduction of the carriers trapping and the long-lived components. Therefore, the possibility of the formation of multiexcitons is enhanced. However, in the case of pulsed X-rays, the long-lived emission is 30% of the total emission photons in the core/shell_l NPLs and almost negligible for core/shell_s and core/shell_m, so part of the carriers can be captured before the occurrence of the carrier multiplication, leading to a loss of the multiexcitons in core/shell_l.

Table 5.6 Summary of the fitting parameters for tri-exponential decay, lifetimes with corresponding amplitudes for core/shell NPLs with different shell thickness under X-rays excitation and the calculated average lifetimes.

	$\tau_1(\text{ns})$	A_1	$\tau_2(\text{ns})$	A_2	$\tau_3(\text{ns})$	A_3	$\tau_4(\text{ns})$	A_4	$\tau_{\text{avg}}(\text{ns})$
core/shell_s	0.51	6.28	2.84	1.74	12.95	0.4	52	<0.01	1.59
core/shell_m	0.54	8.3	2.87	2.16	14.4	0.45	60	<0.01	1.57
core/shell_l	0.64	9.81	3.56	2.71	23.1	0.83	100	0.13	3.58

As compared to low power optical excitation, we observe an acceleration of the decay under X-rays while the emission spectra do not change in small shell samples. We employed thus the time-resolved RL spectrum to investigate the multiexcitons spectra under X-rays excitation. Here we need to point out that in order to obtain high-quality spectra, the sample used for X-rays testing is increased in concentration in order to collect sufficient signals. According to our discussion above, such processing will have an impact on the spectrum of X-rays excitation, and self-absorption may cause a certain red shift in the spectrum. This is consistent with what we observed in the experimental results, as shown in Figure 5.12. We compared the corresponding spectra of 0-2ns and long-lived. Although the existence of self-absorption will affect the spectral lines, we can still clearly observe the evolution of spectral lines over time under X-rays excitation.

First of all, the right side of Figure 5.12 are the time gated spectrum corresponding to intense light excitation(33 μ W) for three core/shell NPLs. Contrary to previous reports

regarding core/shell NPLs[130,159], the fast component we observed, that is, the feature of multiexcitons, appears at the blue edge relative to the long-lived spectrum. We observed the fast component spectral lines in 0-2 ns shows a blue shift, about 10 meV for all samples, not a red shift. This indicates the energy band alignment in our NPLs might behave like quasi type-II, and the blue shift arises from the repulsive interaction between the excitons (see Section 2.3.4).

Secondly, in addition to the blue shift of the spectral line, in core/shell_m, we can also observe a weak emission band at ~ 2.04 eV, which is 60 meV blue-shifted relative to the main peak. Similarly, in core/shell_l, we can also distinguish at the position of 60 meV blue shift (~ 1.92 eV), there is an emission band. In addition, at 2.02 eV, another emission band is also observable. Compared to the main emission peak, this emission band has a blue shift of about 160 meV. Since the shift of the biexciton is usually around 10meV, the two emission bands may arise from higher-order multiexcitons emission. NPLs with thick shells exhibit a larger absorption cross section, which might be the reason for the formation of higher-order multiple excitons. Owing to the limitation of the experimental equipment, we cannot extract the corresponding characteristic lifetimes through time-resolved technique.

Figure 5.12 also plots the spectra of three samples under X-rays excitation. In order to facilitate comparison, we have selected the same time interval as that of intense light excitation. We found that all spectra for X-rays are broader compared to the spectra for photoexcitation, this is because they were taken with a 1mm spectrometer entrance slit to improve light collection, while 0.25 mm was used for optical excitation measurement. First of all, similar to photoexcitation, we observed the emission shoulder of the 0-2ns time gated spectrum appears at the blue edge as observed in steady state experiments, but we did not observe the change in the spectral line on the red side, which may be caused by the mentioned broadening in the spectrum. As time increases, this emission characteristic gradually disappears. In addition, interestingly, for core/shell_l (Figure 5.12f), at 1.915 eV a weak emission band can be observed. This is completely consistent with the spectral characteristics of intense light excitation. Therefore, by comparison, we obtained the similar emission spectra, which allows us to prove spectrally that the type of excited state generated under X-rays excitation is consistent with that under intense light excitation, that is, a recombination process of multiexcitons takes place during the energy relaxation of core/shell NPLs under X-rays excitation.

Through time-resolved decay curves and emission spectra comparison, we have realized the spectral and kinetic identification of excited states produced following X-rays excitation in core/shell NPLs. Combined with the steady-state spectroscopy, we highlight that under X-rays excitations, the energy relaxation process of high-energy electrons in the core/shell NPLs is also dominated by carrier multiplication. This leads to the formation and recombination of multiexcitons, accompanied by the appearance of shoulders on the blue side. And as the size increases, the fraction of multiexcitons emission gradually increases.

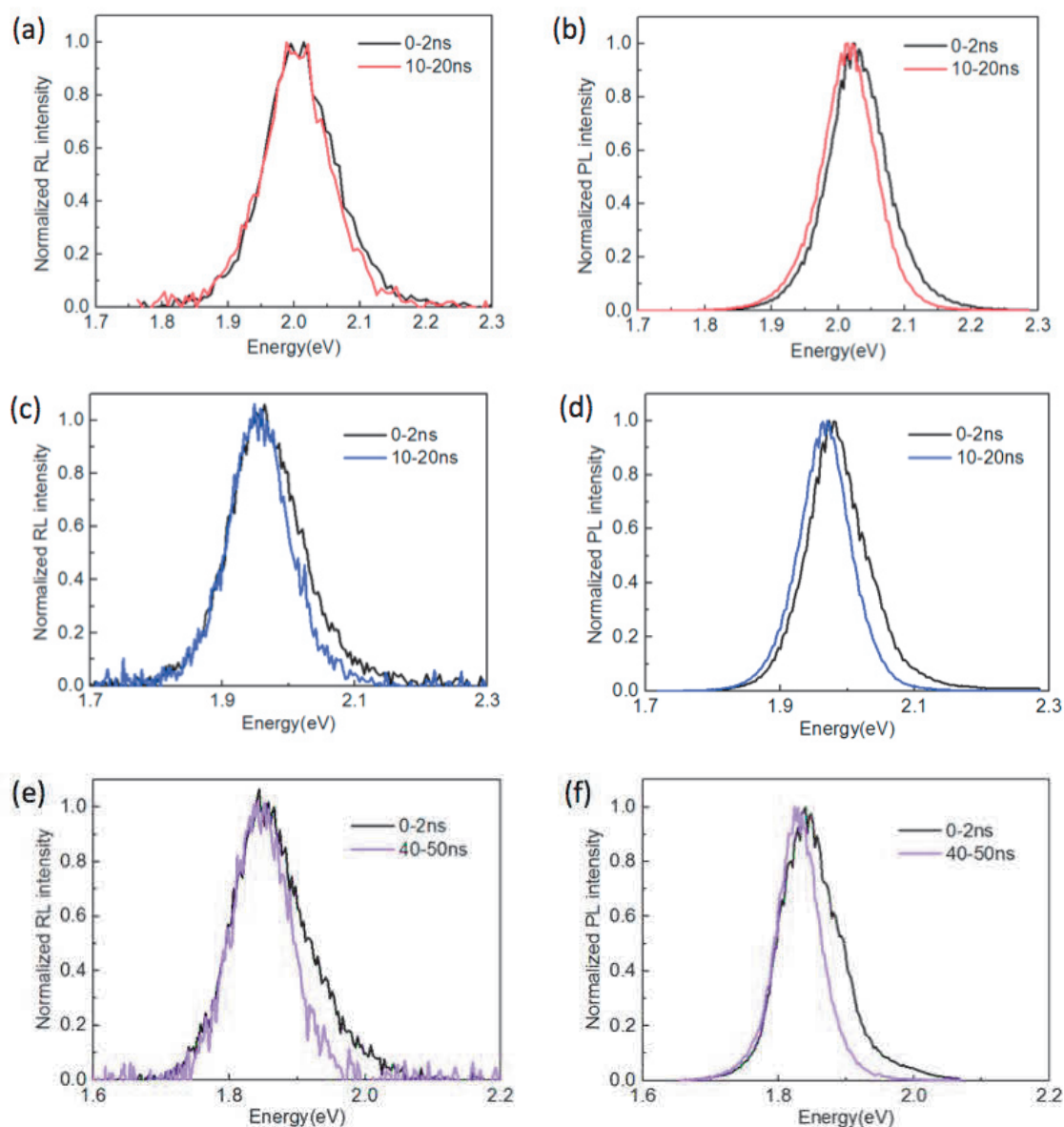


Figure 5.12 Normalized time gated RL(a,c,e) and PL (b,d,f) of different time intervals of core/shell CdSe/CdZnS NPLs with varying shell thickness. (a, b) core/shell_s, (c,d) core/shell_m, (e,f) core/shell_l. X-rays illumination at a voltage of 30 kV voltage and 0.3 μA current. The laser intensity is ~33 μW.

5.4 Core/crown/shell CdSe/CdS/CdZnS nanoplatelets

Core/crown/shell(C/C/S) NPLs is a novel two dimensional heterostructure [97,98,115], and so far there is little research to analyze its properties. Here we will briefly discuss the scintillator behavior of this structure.

5.4.1 Steady state radioluminescence

Similarly, we first compared the normalized steady-state spectra of PL and RL of core/crown/shell CdSe/CdS/CdZnS NPLs, as shown in Figure 5.13. Under low power photoexcitation, the particle emits at 1.92eV. While for X-rays excitation, we observed that the RL spectrum has a slight blue shift relative to the PL spectrum, around 5meV. Compared with core/crown NPLs, RL does not show a redshift, which indicates that the existence of the 2ML shell changes the Coulomb interaction between excitons in the particle, so its band alignment shows a transition from type I to type II or quasi-type II[115]. In addition, compared with the core/shell_s results, in which only the spectrum broaden toward the blue edge can be seen, the slight blue shift might reveal the increase in the repulsion between excitons or the different excited states are generated in core/crown/shell NPLs under X-rays excitation.

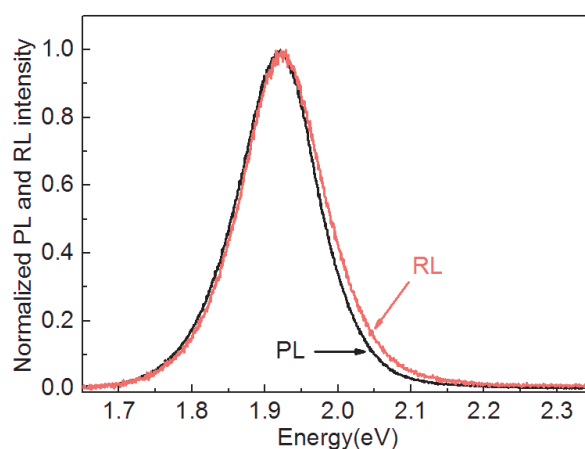


Figure 5.13 Normalized steady state PL and RL spectra for core/crown/shell CdSe/CdS/CdZnS NPLs. The power of photoexciton source is low with 405nm wavelength.

Next, we conducted the experiments on the power dependence of steady state spectroscopy using solution samples. Since the quartz cuvette will produce scintillation signal under X-rays radiation (even if the yield is weak, the fraction of X-rays photons in the quartz will be significantly higher), and meanwhile reduce the photons absorbed in the particles, the solution sample is not suitable for X-rays related research. Therefore, this experiment is only used as an auxiliary research. The specific experimental device optical parametric oscillation laser (OPO) and the preparation of the solution sample are described in Annex2. The particle-dispersed solution can eliminate the influence of energy transfer between particles on the spectrum, and the preparation of low-concentration samples can also reduce self-absorption. The normalized spectra are shown in Figure 5.14, as the excitation power continues to increase, the spectrum is broadened and accompanied by a slight blue shift, which is consistent with the performance of the RL spectrum. This directly indicates that similar radiative recombination may exist under two different excitations, and the effect of energy transfer between particles in the film sample on the spectrum is negligible. The relevant spectra of all other samples can be found in the Annex2.

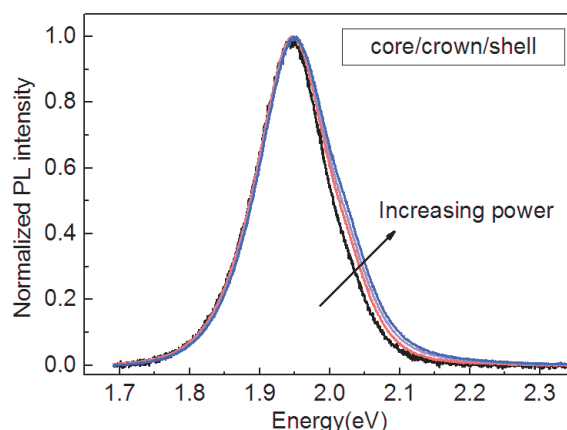


Figure 5.14 Normalized PL spectra with different power intensity for C/C/S NPLs solution sample. Excitation source: OPO with 405nm wavelength and 50Hz.

5.3.2 Time-resolved measurements

The PL spectrally resolved measurement was implemented at two powers, $33 \mu\text{W}$ and 4nW , as shown in Figure 5.15 for spectra at different time intervals. First of all, in the case of low power, the 0-2 ns and 50-60 ns spectra are similar, which means that there is no additional fast component generation, and Forster resonance energy transfer is weak. Otherwise, the small-sized sample will emit photons after absorbing the emitted photons from large sized particles and then emits a photon with a lower energy, which will cause a red shift in the spectrum over time, regardless of the excitation power. In Figure 5.15(a), we did not find a distinguishable spectral redshift, so FRET can be excluded, which is related to the good size distribution of the sample.

Next, we analyze the case of high-power excitation (Figure 5.15b, d). Here we divide the spectrum into 0-60 ns and after 60 ns and discuss separately. First, in the first 60 ns, we observed that the main emission peak at 0-2 ns is 34 meV blue shifted relative to that at 50-60 ns. This spectrally dependent emission band is in agreement with the characteristics of multiexcitons. The blue shift is 3 times larger than that in core/shell NPLs with the similar shell thickness. This may be because the CdS crown promotes the delocalization of electrons in the conduction band, thereby enhancing the local charge imbalance and generating stronger repulsion between excitons.

With the increase in time, the blue shift of the main peak gradually disappears, and the broadening of the spectrum also gradually decreases. For details, shown in Figure 5.15(c), which describes the shift of the main peak of the 0-500 ns spectra and the change of the spectral width. The delayed PL spectrum after 60 ns is shown in Figure 5.15(d). The shift of the main peak can no longer be observed, that is, it is similar to the emission of a single exciton, but it is characterized by a long lifetime. From this similarity, we can conclude that delayed emission is the result of emission from the recovered carriers at $1S_{3/2}1S_e$ exciton state[141]. In addition, in this time range, there is a

slight broadening of the spectrum at the red edge, which may be due to the direct radiative recombination from the carriers trapped.

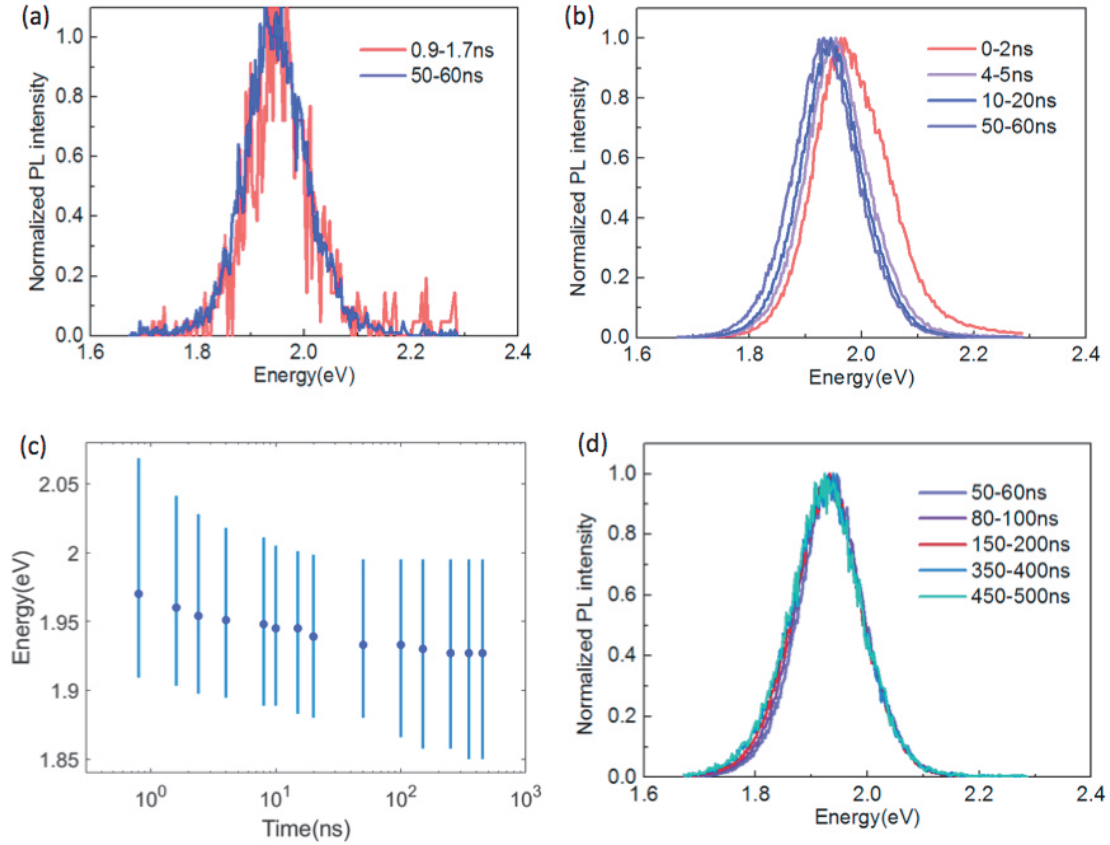


Figure 5.15 Normalized time gated PL for C/C/S NPLs in different time intervals as indicated in the figures under different power intensity. (a) Laser power is 4nW, (b) and (d) the slices for 0-60ns and after 60ns at laser power 33 μ W. (c) The position of the main peak and the change of the spectral width over time at laser power 33 μ W.

Figure 5.16 is the normalized time resolved RL spectra under X-rays excitation. Due to the low signal-to-noise ratio, the signal after 20ns is hidden in the background and cannot be extracted. So here we can only discuss the first 20ns of the spectrum. We can see from the figure that, unlike the RL spectrum of core/shell NPLs, the early spectrum has a blue shift relative to the 10-20ns spectrum, which is about 33meV. Although the 10-20ns spectrum may still consist of a certain fast component, it can be known from the photoexcitation spectrum that there is only a slight deviation from the 50-60ns spectrum. Therefore, we can conclude that at 0-2ns the RL and PL under intense light excitation exhibit a similar blue shift, and similar spectral broadening. This high consistency indicates that the recombination of fast components originates from similar exciton states with photoexcitation.

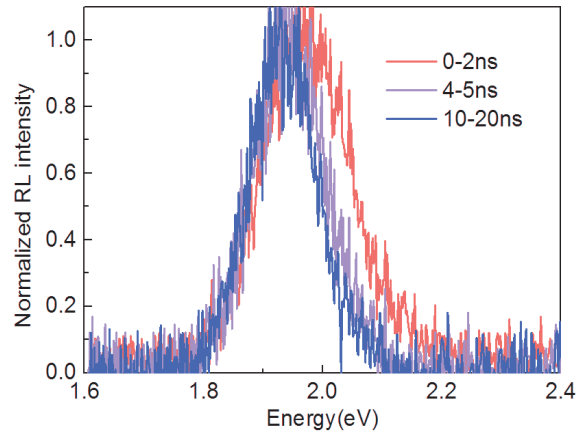


Figure 5.16 Normalized RL spectra for C/C/S NPLs in different time intervals as indicated in the figures under X-rays excitation with 30kV accelerating voltage.

We tested the decay dynamics curve at different powers, and the detection position is the maximum value of the spectrum, as shown in Figure 5.17(a). First of all, compared with other structures of NPLs, the C/C/S samples we synthesized have a longer decay time. As the power increases, an additional fast component appears in the decay curve. We analyzed the evolution of the fast component and the slow component as a function of the excitation laser power in Figure 5.17(b). The slow component is extracted at 75ns of the decay curve. The fast component is the 0ns PL intensity after subtracting the contribution of the single exciton. We can see that the slope of the slow component is close to unity, indicating that it changes linearly with the power. The slightly smaller slope may be caused by the degradation of the sample. For the fast component, the PL intensity exhibits a super-linear increase as the power increases. But similar with the result of core/shell NPLs, the slope is smaller than the simplest biexciton feature. The reason for this small slope is not clear, and sample degradation may be one of them. Nevertheless, this super-linear change represents that multiexcitons are formed in this process.

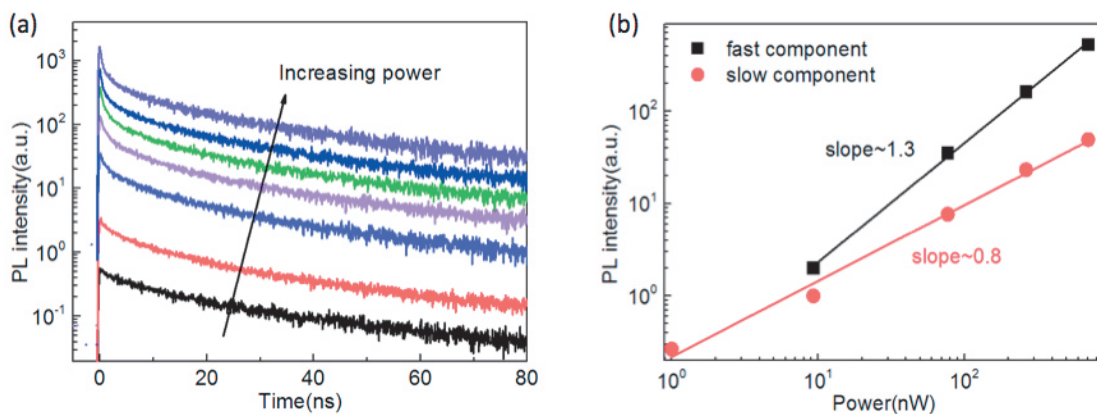


Figure 5.17 (a) Decay dynamics at main peak of C/C/S NPLs for varying power intensity. (b) The evolution of PL intensity as a function of power: slow component is extracted from (a) at 75ns and fast component is the PL intensity at 0ns after subtracting the contribution of single exciton.

Finally, we compared the decay kinetics curves under photoexcitation and X-rays excitation. Similarly, in order to facilitate the comparison, the photoexcitation curve is measured in the out-of-focus condition, this also ensures that no multiexcitons are generated. As shown in Figure 5.18(a), the two different excitation curves can be completely matched after 30ns, so we can subtract the light excitation curve from the X-ray decay curve to obtain the pure fast component. The result is shown in Figure 5.18 (b). Through biexponential fitting, we can extract the lifetime of the fast component about 0.5ns. The specific fitting parameters are shown in Table 5.7.

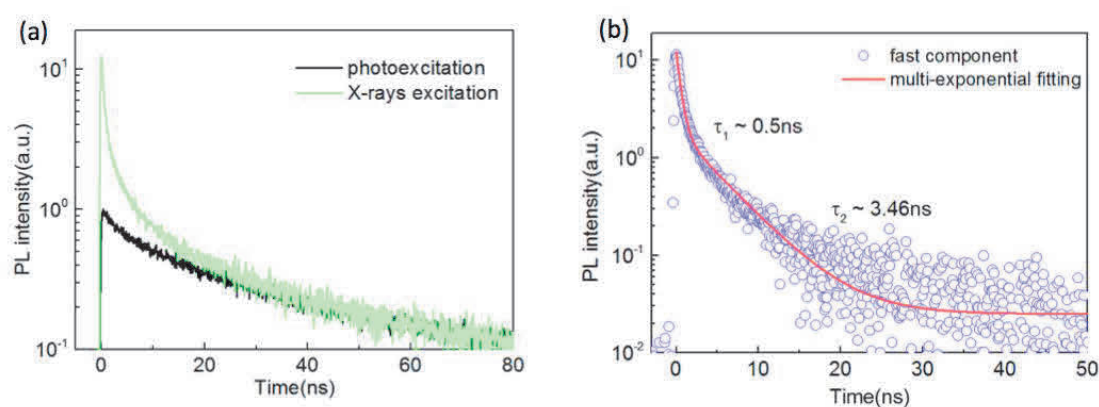


Figure 5.18 (a) RL and PL decay curves of core/crown/shell CdSe/CdS/CdZnS NPLs well normalized at long time, highlighting the multiexcitons component. (b) Biexciton fitting of fast component under X-rays excitation, obtained by subtracting the decay curve under photoexcitation from (a).

Table 5.7 Summary of the fitting parameters for multi-exponential decay, lifetimes with corresponding amplitudes for core/crown/shell NPLs under low intensity photoexcitation and X-rays excitation, and the calculated average lifetimes.

	$\tau_1(\text{ns})$	A_1	$\tau_2(\text{ns})$	A_2	$\tau_3(\text{ns})$	A_3	$\tau_4(\text{ns})$	A_4	$\tau_{\text{avg}}(\text{ns})$
photoexcitation			5.36	0.36	29.84	0.46	160	0.12	55.2
X-rays	0.5	12.01	3.46	3.23	25.61	0.9	160	0.12	3.65

From the similarity on the spectra and the dynamics, we proved the formation of the multiexcitons under X-rays excitation. However, similar with the core/shell_1, the C/C/S NPLs also suffer from the issue of delayed emission, and the fraction of the delayed emission is around 40%, which is consistence with the low quantum yield. The fast component fraction is calculated as 10%, which is 2 times lower than that in core/shell_s with the similar shell thickness. From this, we can know the defects strongly affect the

quantity of multiexcitons through trapping the carriers before the occurrence of the carrier multiplication.

5.5 Conclusion

In this chapter, we apply steady-state spectroscopy and time resolved technique to analyze the scintillating properties of three different heterostructural NPLs under X-rays radiation.

2D NPLs have ultra-fast decay time because of their giant oscillator strength. Since the crown only covered the lateral direction in core/crown structure, it does not release the quantum confinement effect, and thus has a small influence on the decay dynamics curve. We obtain an average lifetime less than 1ns under X-rays excitation. In addition, compared to the PL spectrum, the RL spectrum exhibits a red shift due to the generation of multiexcitons, which is beneficial to reduce self-absorption and practical applications.

We also proved that the formation of multiexcitons under the radiation of X-rays also occurs in core/shell and core/crown/shell NPLs based on the highly uniformity in spectra and kinetics compared to the intense optical excitation, indicating that the carrier multiplication phenomenon is effective in the 2D nanocrystals. But, unlike core/crown, the feature of multiexcitons appears on the blue edge. Meanwhile, due to the reduction of confinement and the delocalization of carriers, the decay time of the excited state in these two structures is longer, but it is still faster than most of QDs. Compared to the core/crown structure, they exhibit the better chemical and physical stabilities. For applications that do not require ultra-fast time response, they will have better performance. In addition, by analyzing steady state spectra of core/shell structures with different shell thicknesses, we found that in the particle size range we are studying (less than 10nm in the vertical direction), the scintillator properties of the core/shell structure show a size dependent behavior. As the thickness of the shell increases, the emission ratio of multiexcitons gradually increases. However, for the pulsed X-rays, the size dependence cannot be observed, the interpretation might be that the carriers are trapped by the defects before the occurrence of carrier multiplication in large particles, leading to the decrease in the formation of multiexcitons.

Chapter 6

Conclusion

This thesis mainly focuses on the investigation of the scintillator properties of II-VI group heterostructural nanocrystals under X-rays ionizing radiation. We have completed the colloidal synthesis and characterization of nanocrystals and analyzed spectrally and temporally the optical response under optical and ionizing radiation aiming to describe the energy relaxation mechanisms and the types of excited states generated under X-rays excitation.

In particular, we successfully synthesized spherical quantum wells (SQWs) CdS/CdSe/CdS with varying shell thicknesses, the diameter is from 15 nm up to 40 nm with a good size dispersion. The sandwich-like structure enables the synthesis of giant shells without the loss of optical quality due to less misfit defects, and the quantum yield here is up to 80% for smaller particles, and even for the larger particles the quantum yield is measured as 35% in thin film. In addition, different heterostructural nanoplatelets (NPLs), core/crown, core/shell and core/crown/shell NPLs are prepared by hot injection method. We achieved the formation of core/crown NPLs with regular shape, facilitating further overcoating and applications. And alloyed core/shell CdSe/CdZnS NPLs were fabricated in three varying shell thickness with narrow PL linewidths, homogeneous morphology and high quantum yield. We also for the first time successfully coated a CdZnS shell on the core/crown seeds via the hot precursor injection with 20% quantum yield in thin film, demonstrating the possibility to fabricate core/crown/shell NPLs through hot-injection method.

To investigate the scintillation properties of NCs, we mainly analyzed the spectral and dynamical behavior under X-rays excitation *via* the steady-state radioluminescence technique and time-resolved techniques. We performed the decay curves measurement under varying excitation powers, this power dependence enables the identification of the excited states. Together with time-resolved emission spectra, we successfully achieved the assignment of single exciton, biexciton, and S-level transition and P-level transition involving the multi-carriers (>4). The biexciton quantum yield was calculated up to 40%. Through comparative analysis between intense optical excitation and X-rays excitation, analogous emission features have been observed, which is an indication of the presence of similar excitonic species, proving that carrier multiplication plays an important role in the scintillation processes. Based on the analysis of decay dynamics, we studied the evolution of the ratio of each excitonic species in varying sized SQWs during the scintillation process. A simulation based on rate equations from Prof A.Vasil'ev (Moscow

state universality) modeled the distribution of the excitation species production in different sized NCs under 30keV photon excitation. The experimental results are consistent with the theoretical modeling, the fraction of the biexciton does not evolve significantly with the particle size in the range we used, suggesting the excitonic species formed under extremely energetic electron excitation is insensitive to the nanoparticle size. We suggest that Auger quenching is dominating when high order multiexcitons are produced in the confined structure which are in principle favored for larger sizes. For this part, considering that larger size increases the decay time of the single exciton, we do not have benefit to use large shells for fast timing applications.

Compared to the SQWs, NPLs displayed faster lifetime due to the strong oscillator strength. Therefore, NPLs is an outstanding fast-timing scintillation material. By comparing the temporally and spectrally radiative recombination produced following excitation under photoexciton and under X-rays excitation, we identify and quantify the distribution of excitonic species during the scintillation process of different Cd-based nanoplatelets. Different behaviors have been observed in core/crown, core/shell, and core/crown/shell NPLs under X-rays excitation. Red-shifted spectrum with respect to PL was observed in core/crown and is characterized with fast time constant of less than 1 ns. This red shift is beneficial for the reduction of self-absorption. Meanwhile in core/shell and core/crown/shell NPLs, the fast emissive features were found on the blue edge from the time resolved spectra. Based on the highly uniformity in spectra and kinetics compared to the intense optical excitation, we proved that the fast component origins from the multiexcitons under the radiation of X-rays, indicating that the carrier multiplication phenomenon is effective in the 2D nanocrystals. In addition, by analyzing steady state spectra of core/shell structures with different shell thicknesses, we found that in the particle size range we are studying (less than 10nm in thickness), the fraction of multiexcitons emission gradually increases as the thickness of the shell increases. However, for the pulsed X-rays excitation, the size dependent behavior cannot be observed, the interpretation might be that the carriers are trapped by the defects before the occurrence of carrier multiplication in large particles, leading to the decrease in the formation of multiexcitons.

In summary, we demonstrated that the excitonic species during the scintillation process under X-rays excitation are similar to that under intense optical excitation in II-VI nanoparticles, both for SQWs and 2D NPLs. All observable emission signals can be attributed to recombination of single, charged and multiexcitons. The multiexcitons are mostly produced by carrier multiplication of secondary electrons. And the size-dependent trend is observed for small sized NPLs, not the larger SQWs particles. These observations give direct insight into understanding of the energy deposition and relaxation process under X-rays radiation in nanoparticles.

Even though we have achieved the investigation on the scintillation properties of II-VI nanocrystals, there are still many challenges that need to be overcome for future research and applications. First, nanocrystals which can suppress the Auger effect without the prolong of lifetime, are needed for fast timing scintillators. Meanwhile, since the

defects usually introduce delayed emission, realization of defects free nanocrystals will also contribute to achieve this ultrafast decay. In addition, self-absorption limits the nanocrystals concentration, making the lower energy deposition in the scintillator, and also significantly affects the light collection emission of multiexcitons. Therefore, to reduce the self-absorption is also an important issue to address. Nevertheless, with the developing of the synthetic technique, the nanocrystals will be promising as a scintillating material in the future.

Annexe1: Estimation of absorption cross section of spherical quantum wells

We estimated the cross-section of the SQWs on the basis of ref.[85]. Specifically, the absorption cross-section of SQWs with size(1.3/0.6/5.3nm) at 3.1eV was measured as about $8.3 \times 10^{-14} \text{cm}^2$ by using the PL saturation method. We corrected the value with a factor of 1.03 to take into account the excitation wavelength of our setup (3.06eV). Since the similar size with our smallest particles, we are able to consider this value is the absorption cross-section of 15 nm SQWs, which is $8 \times 10^{-14} \text{cm}^2$. We are allowed to calculate the absorption cross-section of all the sized SQWs by assuming to the volume scaling[162], as depicted in Table A1.1. The absorption cross section of the largest SQWs is around three orders of magnitude larger than that of regular quantum dots.

It should be pointed out that since the absorption at the excitation wavelength is mainly caused by the CdS shell, and the shell thickness of our 15 nm samples(1.3/1.8/4.4nm) is a little smaller than the mentioned SQWs(1.3/0.6/5.3nm) with the similar volume. Therefore this estimated value may be a little overestimated.

Table A1.1 Absorption cross-section estimations for different sized SQWs

Diameter (nm)	15	20	25	30	35	40
$\sigma \text{ (cm}^2\text{)}$	8×10^{-14}	1.9×10^{-13}	3×10^{-13}	6.4×10^{-13}	1×10^{-12}	1.2×10^{-12}

To calculate the average number of exciton formed per nanocrystal per pulse($\langle N \rangle$), the following expression was used,

$$\langle N \rangle = j \sigma \quad (\text{A1-1})$$

where j and σ respectively represent the intensity of the excitation laser and the absorption cross section of the sample at the excitation wavelength. The excitation intensity of the laser can be obtained by,

$$j = \frac{P / (f \cdot A)}{hc / \lambda} \quad (\text{A1-2})$$

where the laser power P can be directly measured, f is the repetition frequency of the laser, A is the area of size spot, and, the λ , h , c are the excitation wavelength, Planck's

constant, and the speed of light, respectively. The diameter of laser spot is approximately 4 μ m. Table A1.2 shows the $\langle N \rangle$ for different sized SQWs.

Table A1.2 The average number of exciton formed per nanocrystal per pulse($\langle N \rangle$) for different sized SQWs

Power(nW)	1	9.3	29.5	77	264	702	1654	4399	12739	35789
15nm	0.003	0.024	0.074	0.19	0.67	1.78	4.18	11.1	32.2	90.5
25nm	0.009	0.09	0.28	0.71	2.51	6.68	15.7	41.6	120	339
40nm	0.04	0.36	1.11	2.85	10.1	26.7	62.7	166	483	1357

Annexe2: Solution sample under optical parametric oscillation laser

In order to obtain steady-state multiexcitons emission characteristics, we carried out the power dependent PL spectra measurement with an optical parametric oscillation laser(OPO). Since too high laser intensity is very easy to cause the film sample to be burnt out, thereby affecting the reliability of the experimental data, so for this measurement, the emission spectra have been performed in solution sample. All the solution was diluted in order to obtain an optical density below 0.1 to avoid self-absorption phenomena. The pulsed laser source is OPO from EKSPLA model NT230-50-SH, the excitation wavelength is 405nm with a repetition rate of 50Hz and a pulse width of 3ns. The emitted light was collected by an optical fiber placed at 90 degree angle from the excitation beam and fed to a monochromator from Jobin-Yvon (TRIA X 320) coupled to an EMCCD (Newton 920U from Andor). The sample is not placed at focus point. The laser spot diameter is measured as 2mm, and the power used here is from 0.1mW to 105mW.

A2.1 Spherical quantum wells solution sample

In FigureA2.1, we present the normalized PL spectra under varying power excitation for 15nm, 25nm and 40nm SQWs. With the power increases, we observed the emergence of blue shoulder for 15nm SQWs, which is consistent with the signature of multiexcitons in the time-resolved spectra, similarly, an emission feature can be seen at 2.4eV corresponding to the shell-related transition in the presence of a large number of excitons. In addition, different multiexcitons features are distinguishable on the blue shoulder in the larger particles compared to that in 15nm, which is the result of the larger absorption cross section, the emission band at 2.0eV and 2.15eV is consistence with the multicarriers(>4) involved S-level and P-level transition respectively..

However, when we plot the evolution of integrated PL intensity as a function of excitation fluence, as shown in Figure A2.1(b, d, f), the slope is around 0.5, the increase of the intensity is sublinear with $\langle N \rangle$ for the power range we used. The minimum of $\langle N \rangle$ here is ~ 15 exciton/pulse for 15nm SQWs, therefore plenty of multiexcitons formed in the SQWs, the sublinear indicated the existence of the non-radiative recombination, which is not completely suppressed. When the power continue to increase, the PL intensity continues to increase, suggesting that part of multiexcitons still recombined radiatively. This is the result of the high quantum yield of multiexcitons. For 40 nm

SQWs, at 20 mJ/cm², the curves start to saturate, this can be interpreted with the ultralarge absorption cross-section, leading to the formation of much higher order excitons, in which the Auger recombination become predominant.

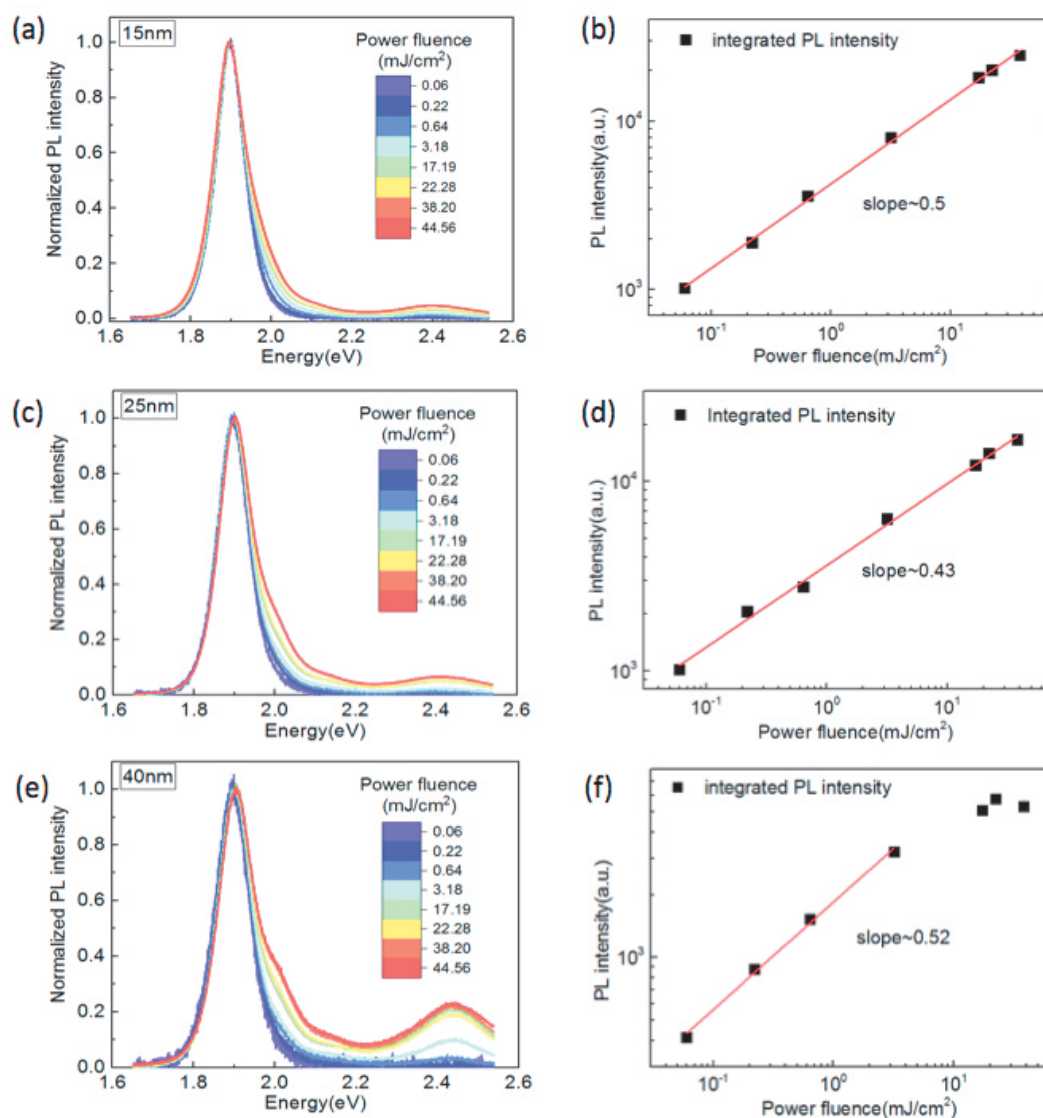
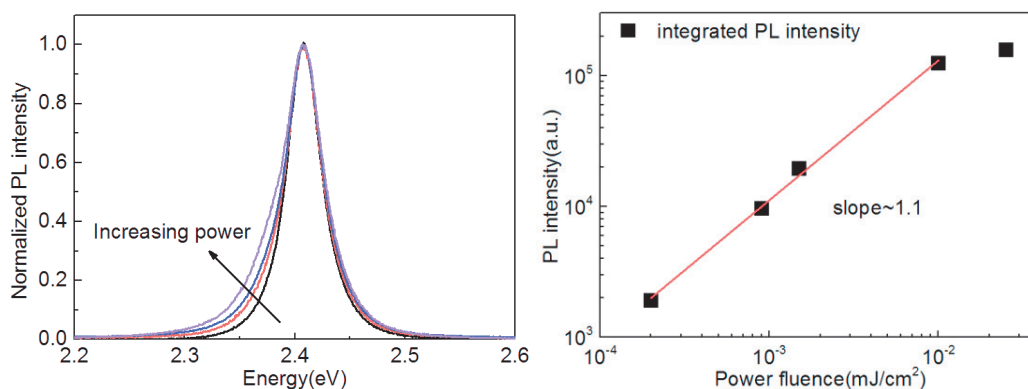


Figure A2.1 (a,c,e) Emission spectra of SQWs with varying shell thickness under varying laser power. (b,d,f) The evolution of integrated PL intensity as a function of excitation power.

A2.2 Heterostructural nanoplatelets solution sample

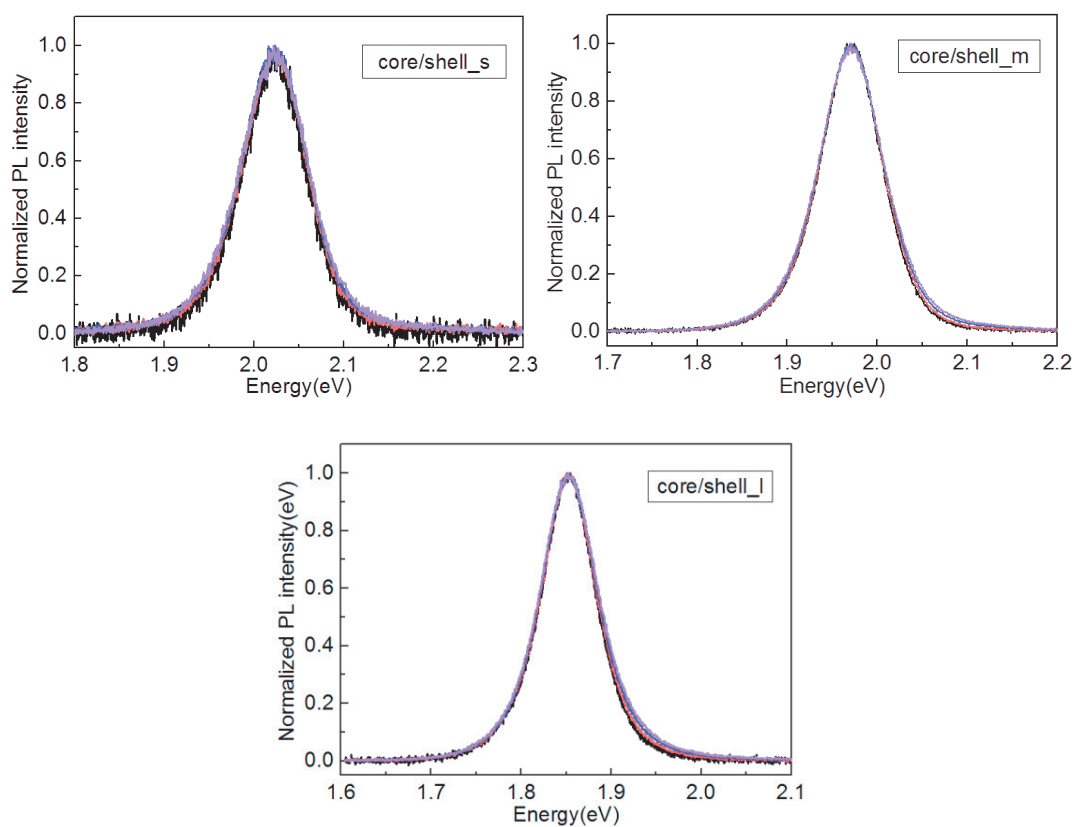
We performed the same measurement on NPLs as shown in Figure A2.2 and A2.3, we summarized the behavior of different heterostructural NPLs under OPO excitation.

A2.2.1 Core/crown CdSe/CdS



FigureA2.2 Emission spectra of CdSe/CdS nanoplatelets under varying laser power.(b) The evolution of integrated PL intensity as a function of excitation power.

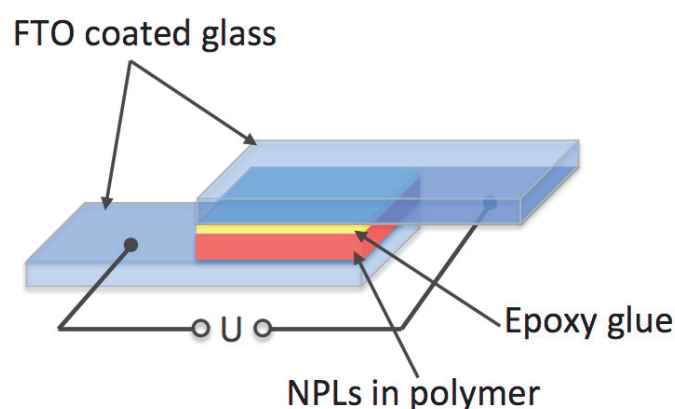
A2.2.2 Core/shell CdSe/CdZnS



FigureA2.3 Emission spectra of CdSe/CdZnS nanoplatelets with varying shell thickness under varying laser power.

Annexe3: The influence of the applied voltage on PL spectra in nanoplatelets

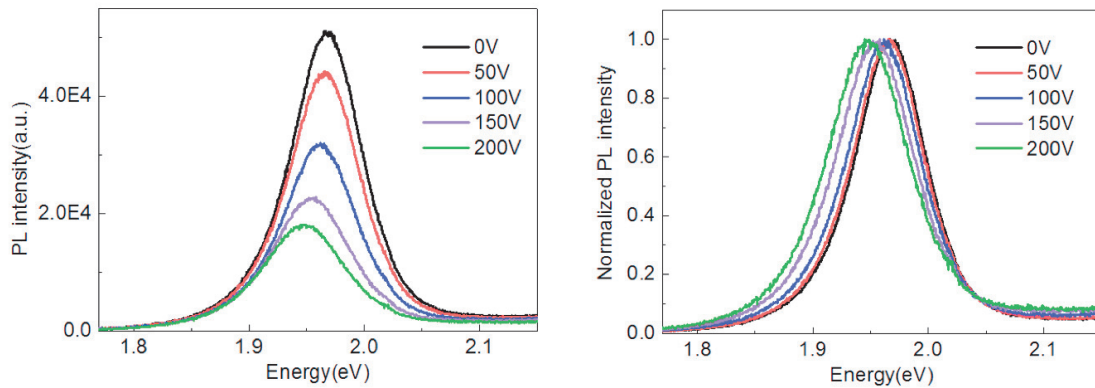
In order to investigate the influence of electric field on photoluminescence, we applied an external electric field to CdSe/CdZnS NPLs according to ref.[163]. We focus on the change of photoluminescence intensity and spectral profile by adjusting the applied voltage. The schematic diagram of the device is shown in Figure A3.1. We designed a sandwich-like structure, it consists of two electrodes, which are made of FTO coated glass, and a NPLs film was sandwiched between the electrodes. Specifically, 100 μ l NPLs in polymer solution (PMAO) was deposited on the FTO surface of glass by spin-coating (1500rpm for 40s). The second FTO electrode was attached to the NPLs containing polymeric film with epoxy glue, then dry for one night before applying the voltage. A DC voltage power supply is used to generate the external voltage. The experimental setup is based on the steady-state spectrum measurement setup mentioned previously.



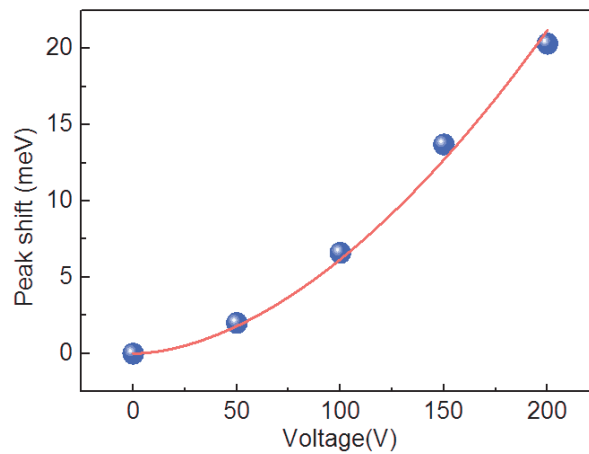
FigureA3.1 Schematic representation of the device for applying voltage on NPLs: CdSe/CdZnS NPLs in polymer is sandwiched between two FTO electrodes coated on glass, epoxy glue is used to attach the second electrode.

The applied voltage we used here is from 0V to 200V. The change of the integrated PL intensity and the spectra profile are presented in the Figure A3.2. The emission was effected strongly as the voltage increases. First, a great decrease of the emission intensity with increasing applied voltage is observed, which can be attributed to the charging effect of the NPLs[164].

We also observe a redshift of the peak position accompanied by a significant linewidth broadening. The spectral broadening as a function of applied voltage is related to the increased LO (longitudinal optical)-phonon coupling in the presence of an electric field, while the red shift in peak position has been demonstrated as a characteristic of the quantum confined Stark effect. In ensembles of NCs, the stark shift approximately exhibits a quadratic dependence to the applied voltage[164], which is consistent with our fitting in FigureA3.3.



FigureA3.2 (a) integrated PL spectra under applied voltage from 0V to 200V, (b) Normalized voltage-dependent PL spectra, to highlight to linewidth broadening and the red shift of the peak position as the increasing applied voltage.



FigureA3.3 The red shift of PL peak position over applied voltage with respect to PL peak at 0V extracted from the spectra shown in Figure A3.2(b), fitted approximately with a quadratic function(~ 1.8) of applied voltage (red line)

References

- [1] Murray C B, Norris D J and Bawendi M G 1993 Synthesis and characterization of nearly monodisperse CdE (E = sulfur, selenium, tellurium) semiconductor nanocrystallites *J. Am. Chem. Soc.* **115** 8706–15
- [2] Schaller R D and Klimov V I 2004 High Efficiency Carrier Multiplication in PbSe Nanocrystals: Implications for Solar Energy Conversion *Phys. Rev. Lett.* **92** 186601
- [3] García-Santamaría F, Chen Y, Vela J, Schaller R D, Hollingsworth J A and Klimov V I 2009 Suppressed Auger Recombination in “Giant” Nanocrystals Boosts Optical Gain Performance *Nano Lett.* **9** 3482–8
- [4] Lim J, Park Y-S and Klimov V I 2018 Optical gain in colloidal quantum dots achieved with direct-current electrical pumping *Nat. Mater.* **17** 42–9
- [5] Diroll B T, Talapin D V and Schaller R D 2017 Violet-to-Blue Gain and Lasing from Colloidal CdS Nanoplatelets: Low-Threshold Stimulated Emission Despite Low Photoluminescence Quantum Yield *ACS Photonics* **4** 576–83
- [6] Röntgen W C 1896 On a New Kind of Rays *Science* **3** 227–31
- [7] Dujardin C, Auffray E, Bourret-Courchesne E, Dorenbos P, Lecoq P, Nikl M, Vasil'ev A N, Yoshikawa A and Zhu R-Y 2018 Needs, Trends, and Advances in Inorganic Scintillators *IEEE Trans. Nucl. Sci.* **65** 1977–97
- [8] Létant S E and Wang T-F 2006 Semiconductor Quantum Dot Scintillation under γ -Ray Irradiation *Nano Lett.* **6** 2877–80
- [9] Hossu M, Liu Z, Yao M, Ma L and Chen W 2012 X-ray luminescence of CdTe quantum dots in LaF₃:Ce/CdTe nanocomposites *Appl. Phys. Lett.* **100** 013109
- [10] Turtos R M, Gundacker S, Omelkov S, Mahler B, Khan A H, Saaring J, Meng Z, Vasil'ev A, Dujardin C, Kirm M, Moreels I, Auffray E and Lecoq P 2019 On the use of CdSe scintillating nanoplatelets as time taggers for high-energy gamma detection *Npj 2D Mater. Appl.* **3** 37
- [11] Chen Q, Wu J, Ou X, Huang B, Almutlaq J, Zhumeckenov A A, Guan X, Han S, Liang L, Yi Z, Li J, Xie X, Wang Y, Li Y, Fan D, Teh D B L, All A H, Mohammed O F, Bakr O M, Wu T, Bettinelli M, Yang H, Huang W and Liu X 2018 All-inorganic perovskite nanocrystal scintillators *Nature* **561** 88–93

- [12] Hu J, Tang Y, Elmenoufy A H, Xu H, Cheng Z and Yang X 2015 Nanocomposite-Based Photodynamic Therapy Strategies for Deep Tumor Treatment *Small* **11** 5860–87
- [13] Kamkaew A, Chen F, Zhan Y, Majewski R L and Cai W 2016 Scintillating Nanoparticles as Energy Mediators for Enhanced Photodynamic Therapy *ACS Nano* **10** 3918–35
- [14] Padilha L A, Bae W K, Klimov V I, Pietryga J M and Schaller R D 2013 Response of Semiconductor Nanocrystals to Extremely Energetic Excitation *Nano Lett.* **13** 925–32
- [15] Ekimov A and Onushcheko A 1981 Quantum Size Effect in Three-Dimensional Microscopic Semiconductor Crystals *ZhETF Pis Ma Redaktsiiu* **34** 363
- [16] Klimov V I 2010 *Nanocrystal Quantum Dots, Second* (Vii)
- [17] Rabouw F T and de Mello Donega C 2016 Excited-State Dynamics in Colloidal Semiconductor Nanocrystals *Top. Curr. Chem.* **374**
- [18] Demir H V and Gaponenko S V 2018 *Applied nanophotonics* (Cambridge University Press)
- [19] Brus L 1986 Electronic wave functions in semiconductor clusters: experiment and theory *J. Phys. Chem.* **90** 2555–60
- [20] Efros A I L and Rosen M 2000 The Electronic Structure of Semiconductor Nanocrystals *Annu. Rev. Mater. Sci.* **30** 475–521
- [21] Edvinsson T 2018 Optical quantum confinement and photocatalytic properties in two-, one- and zero-dimensional nanostructures *R. Soc. Open Sci.* **5** 180387
- [22] Donegá C de M 2011 Synthesis and properties of colloidal heteronanocrystals *Chem Soc Rev* **40** 1512–46
- [23] Roduner E 2006 Size matters: why nanomaterials are different *Chem. Soc. Rev.* **35** 583
- [24] Munro A M, Jen-La Plante I, Ng M S and Ginger D S 2007 Quantitative Study of the Effects of Surface Ligand Concentration on CdSe Nanocrystal Photoluminescence *J. Phys. Chem. C* **111** 6220–7
- [25] Dabbousi B O, Rodriguez-Viejo J, Mikulec F V, Heine J R, Mattoussi H, Ober R, Jensen K F and Bawendi M G 1997 (CdSe)ZnS Core–Shell Quantum Dots: Synthesis and Characterization of a Size Series of Highly Luminescent Nanocrystallites *J. Phys. Chem. B* **101** 9463–75

- [26] Reiss P, Protière M and Li L 2009 Core/Shell Semiconductor Nanocrystals *Small* **5** 154–68
- [27] Hines M A and Guyot-Sionnest P 1996 Synthesis and Characterization of Strongly Luminescing ZnS-Capped CdSe Nanocrystals *J. Phys. Chem.* **100** 468–71
- [28] Mahler B, Spinicelli P, Buil S, Quelin X, Hermier J-P and Dubertret B 2008 Towards non-blinking colloidal quantum dots *Nat. Mater.* **7** 659–64
- [29] Reiss P, Carayon S, Bleuse J and Pron A 2003 Low polydispersity core/shell nanocrystals of CdSe/ZnSe and CdSe/ZnSe/ZnS type: preparation and optical studies *Synth. Met.* **139** 649–52
- [30] Toufanian R, Piryatinski A, Mahler A H, Iyer R, Hollingsworth J A and Dennis A M 2018 Bandgap Engineering of Indium Phosphide-Based Core/Shell Heterostructures Through Shell Composition and Thickness *Front. Chem.* **6** 567
- [31] Franco C V 2020 Etude par spectroscopies optiques résolue dans le temps des dynamiques ultrarapides dans les nanostructures colloïdales de pérovskite.
- [32] Peterson M D, Cass L C, Harris R D, Edme K, Sung K and Weiss E A 2014 The Role of Ligands in Determining the Exciton Relaxation Dynamics in Semiconductor Quantum Dots *Annu. Rev. Phys. Chem.* **65** 317–39
- [33] Nasilowski M 2015 *Synthesis and optical spectroscopy of thick-shell semiconductor nanoparticles: applications to biological imaging* PhD Thesis (Paris 6)
- [34] Klimov V I 2000 Quantization of Multiparticle Auger Rates in Semiconductor Quantum Dots *Science* **287** 1011–3
- [35] Li Q and Lian T Area and Thickness Dependent Bi-Exciton Auger Recombination in Colloidal CdSe Nanoplatelets: Breaking the “Universal Volume Scaling Law” *Nano Lett.* **19**
- [36] Efros A L and Nesbitt D J 2016 Origin and control of blinking in quantum dots *Nat. Nanotechnol.* **11** 661–71
- [37] Nasilowski M, Spinicelli P, Patriarche G and Dubertret B 2015 Gradient CdSe/CdS Quantum Dots with Room Temperature Biexciton Unity Quantum Yield *Nano Lett.* **15** 3953–8
- [38] Park Y-S, Bae W K, Padilha L A, Pietryga J M and Klimov V I 2014 Effect of the Core/Shell Interface on Auger Recombination Evaluated by Single-Quantum-Dot Spectroscopy *Nano Lett.* **14** 396–402
- [39] Klimov V I 2007 Spectral and Dynamical Properties of Multiexcitons in Semiconductor Nanocrystals *Annu. Rev. Phys. Chem.* **58** 635–73

- [40] Achermann M, Hollingsworth J A and Klimov V I 2003 Multiexcitons confined within a sub-excitonic volume: Spectroscopic and dynamical signatures of neutral and charged biexcitons in ultrasmall semiconductor nanocrystals *Phys. Rev. B* **68**
- [41] McGuire J A, Joo J, Pietryga J M, Schaller R D and Klimov V I 2008 New Aspects of Carrier Multiplication in Semiconductor Nanocrystals *Acc. Chem. Res.* **41** 1810–9
- [42] Narvaez G A, Bester G, Franceschetti A and Zunger A 2006 Excitonic exchange effects on the radiative decay time of monoexcitons and biexcitons in quantum dots *Phys. Rev. B* **74** 205422
- [43] Shulenberger K E, Bischof T S, Caram J R, Utzat H, Coropceanu I, Nienhaus L and Bawendi M G 2018 Multiexciton Lifetimes Reveal Triexciton Emission Pathway in CdSe Nanocrystals *Nano Lett.* **18** 5153–8
- [44] Park Y-S, Malko A V, Vela J, Chen Y, Ghosh Y, García-Santamaría F, Hollingsworth J A, Klimov V I and Htoon H 2011 Near-Unity Quantum Yields of Biexciton Emission from CdSe / CdS Nanocrystals Measured Using Single-Particle Spectroscopy *Phys. Rev. Lett.* **106**
- [45] Piryatinski A, Ivanov S A, Tretiak S and Klimov V I 2007 Effect of Quantum and Dielectric Confinement on the Exciton–Exciton Interaction Energy in Type II Core/Shell Semiconductor Nanocrystals *Nano Lett.* **7** 108–15
- [46] Caruge J-M, Chan Y, Sundar V, Eisler H J and Bawendi M G 2004 Transient photoluminescence and simultaneous amplified spontaneous emission from multiexciton states in CdSe quantum dots *Phys. Rev. B* **70** 085316
- [47] Htoon H, Malko A V, Bussian D, Vela J, Chen Y, Hollingsworth J A and Klimov V I 2010 Highly Emissive Multiexcitons in Steady-State Photoluminescence of Individual “Giant” CdSe/CdS Core/Shell Nanocrystals *Nano Lett.* **10** 2401–7
- [48] Cihan A F, Kelestemur Y, Guzel Turk B, Yerli O, Kurum U, Yaglioglu H G, Elmali A and Demir H V 2013 Attractive versus Repulsive Excitonic Interactions of Colloidal Quantum Dots Control Blue- to Red-Shifting (and Non-shifting) Amplified Spontaneous Emission *J. Phys. Chem. Lett.* **4** 4146–52
- [49] Gollner C, Ziegler J, Protesescu L, Dirin D N, Lechner R T, Fritz-Popovski G, Sytnyk M, Yakunin S, Rotter S, Yousefi Amin A A, Vidal C, Hrelescu C, Klar T A, Kovalenko M V and Heiss W 2015 Random Lasing with Systematic Threshold Behavior in Films of CdSe/CdS Core/Thick-Shell Colloidal Quantum Dots *ACS Nano* **9** 9792–801
- [50] Franceschetti A and Troparevsky 2007 Radiative Recombination of Triexcitons in CdSe Colloidal Quantum Dots *J. Phys. Chem. C* **111** 6154–7

- [51] Fisher B, Caruge J M, Zehnder D and Bawendi M 2005 Room-Temperature Ordered Photon Emission from Multiexciton States in Single CdSe Core-Shell Nanocrystals *Phys. Rev. Lett.* **94**
- [52] Fisher B, Caruge J-M, Chan Y-T, Halpert J and Bawendi M G 2005 Multiexciton fluorescence from semiconductor nanocrystals *Chem. Phys.* **318** 71–81
- [53] Vavilov V S 1959 On photo-ionization by fast electrons in germanium and silicon *J. Phys. Chem. Solids* **8** 223–6
- [54] Shockley W and Queisser H J 1961 Detailed balance limit of efficiency of p-n junction solar cells *J. Appl. Phys.* **32** 510–9
- [55] Klimov V I 2006 Detailed-balance power conversion limits of nanocrystal-quantum-dot solar cells in the presence of carrier multiplication *Appl. Phys. Lett.* **89** 123118
- [56] Hu F, Lv B, Yin C, Zhang C, Wang X, Lounis B and Xiao M 2016 Carrier Multiplication in a Single Semiconductor Nanocrystal *Phys. Rev. Lett.* **116**
- [57] de Weerd C, Gomez L, Capretti A, Lebrun D M, Matsubara E, Lin J, Ashida M, Spoor F C M, Siebbeles L D A, Houtepen A J, Suenaga K, Fujiwara Y and Gregorkiewicz T 2018 Efficient carrier multiplication in CsPbI₃ perovskite nanocrystals *Nat. Commun.* **9** 4199
- [58] Jung I D, Cho M K, Lee S M, Bae K M, Jung P G, Lee C H, Lee J M, Yun S, Kim H K, Kim S S and Ko J S 2009 Flexible Gd₂O₂S:Tb scintillators pixelated with polyethylene microstructures for digital x-ray image sensors *J. Micromechanics Microengineering* **19** 015014
- [59] Glodo J, Wang Y, Shawgo R, Brecher C, Hawrami R H, Tower J and Shah K S 2017 New Developments in Scintillators for Security Applications *Phys. Procedia* **90** 285–90
- [60] Hofstadter R 1948 Alkali Halide Scintillation Counters *Phys. Rev.* **74** 100–1
- [61] Van Sciver W and Hofstadter R 1951 Scintillations in Thallium-Activated CaI₂ and CsI *Phys. Rev.* **84** 1062–3
- [62] Weber M J and Monchamp R R 1973 Luminescence of Bi₄Ge₃O₁₂: Spectral and decay properties *J. Appl. Phys.* **44** 5495–9
- [63] van Loef E V D, Dorenbos P, van Eijk C W E, Krämer K and Güdel H U 2001 High-energy-resolution scintillator: Ce³⁺ activated LaBr₃ *Appl. Phys. Lett.* **79** 1573–5
- [64] Nikl M 2006 Scintillation detectors for x-rays *Meas. Sci. Technol.* **17** R37–54

- [65] Maddalena F, Tjahjana L, Xie A, Arramel, Zeng S, Wang H, Coquet P, Drozdowski W, Dujardin C, Dang C and Birowosuto M 2019 Inorganic, Organic, and Perovskite Halides with Nanotechnology for High-Light Yield X- and γ -ray Scintillators *Crystals* **9** 88
- [66] DUJARDIN C 2018 Inorganic scintillating materials 16
- [67] Létant S E and Wang T-F 2006 Study of porous glass doped with quantum dots or laser dyes under alpha irradiation *Appl. Phys. Lett.* **88** 103110
- [68] Yao M, Zhang X, Ma L, Chen W, Joly A G, Huang J and Wang Q 2010 Luminescence enhancement of CdTe nanostructures in LaF₃:Ce/CdTe nanocomposites *J. Appl. Phys.* **108** 103104
- [69] Lawrence W G, Thacker S, Palamakumbura S, Riley K J and Nagarkar V V 2012 Quantum Dot-Organic Polymer Composite Materials for Radiation Detection and Imaging *IEEE Trans. Nucl. Sci.* **59** 215–21
- [70] Tam A K, Boyraz O, Unangst J, Nazareta P, Schreuder M and Nilsson M 2018 Quantum-dot doped polymeric scintillation material for radiation detection *Radiat. Meas.* **111** 27–34
- [71] Hosseini M A, Feizi S, Mehdizadeh A, Ashtari P, Mojtahedzadeh M, Mosleh-Shirazi M A and Alipour A 2019 Dosimetric investigation of a new quantum dots/nanocomposite (CdTe QDs/PVK) sensor for real-time gamma radiation detection *Appl. Phys. A* **125** 868
- [72] Burke E R, DeHaven S L and Williams P A 2016 Scintillating quantum dots for imaging x-rays (SQDIX) for aircraft inspection 42ND ANNUAL REVIEW OF PROGRESS IN QUANTITATIVE NONDESTRUCTIVE EVALUATION: Incorporating the 6th European-American Workshop on Reliability of NDE (Minneapolis, Minnesota) p 110007
- [73] Guidelli E J, Lignos I, Yoo J J, Lusardi M, Bawendi M G, Baffa O and Jensen K F 2018 Mechanistic Insights and Controlled Synthesis of Radioluminescent ZnSe Quantum Dots Using a Microfluidic Reactor *Chem. Mater.* **30** 8562–70
- [74] Withers N J, Sankar K, Akins B A, Memon T A, Gu T, Gu J, Smolyakov G A, Greenberg M R, Boyle T J and Osiński M 2008 Rapid degradation of CdSe/ZnS colloidal quantum dots exposed to gamma irradiation *Appl. Phys. Lett.* **93** 173101
- [75] Gaur G, Koktysh D S, Fleetwood D M, Weller R A, Reed R A, Rogers B R and Weiss S M 2016 Influence of Ionizing Radiation and the Role of Thiol Ligands on the Reversible Photodarkening of CdTe/CdS Quantum Dots *ACS Appl. Mater. Interfaces* **8** 7869–76

- [76] Delage M-È, Lecavalier M-È, Cloutier É, Larivière D, Allen C Nì and Beaulieu L 2016 Robust shell passivation of CdSe colloidal quantum dots to stabilize radioluminescence emission *AIP Adv.* **6** 105011
- [77] Ithurria S and Dubertret B 2008 Quasi 2D Colloidal CdSe Platelets with Thicknesses Controlled at the Atomic Level *J. Am. Chem. Soc.* **130** 16504–5
- [78] Turtos R M, Gundacker S, Polovitsyn A, Christodoulou S, Salomoni M, Auffray E, Moreels I, Lecoq P and Grim J Q 2016 Ultrafast emission from colloidal nanocrystals under pulsed X-ray excitation *J. Instrum.* **11** P10015–P10015
- [79] Zhang Y, Sun R, Ou X, Fu K, Chen Q, Ding Y, Xu L-J, Liu L, Han Y, Malko A V, Liu X, Yang H, Bakr O M, Liu H and Mohammed O F 2019 Metal Halide Perovskite Nanosheet for X-ray High-Resolution Scintillation Imaging Screens *ACS Nano* **13** 2520–5
- [80] Bulin A-L, Vasil'ev A, Belsky A, Amans D, Ledoux G and Dujardin C Modelling energy deposition in nanoscintillators to predict the efficiency of the X-ray-induced photodynamic effect 9
- [81] Jeong B G, Park Y-S, Chang J H, Cho I, Kim J K, Kim H, Char K, Cho J, Klimov V I, Park P, Lee D C and Bae W K 2016 Colloidal Spherical Quantum Wells with Near-Unity Photoluminescence Quantum Yield and Suppressed Blinking *ACS Nano* **10** 9297–305
- [82] Battaglia D, Li J J, Wang Y and Peng X 2003 Colloidal Two-Dimensional Systems: CdSe Quantum Shells and Wells *Angew. Chem. Int. Ed.* **42** 5035–9
- [83] Xu J, Xiao M, Battaglia D and Peng X 2005 Exciton radiative recombination in spherical CdS/CdSe/CdS quantum-well nanostructures *Appl. Phys. Lett.* **87** 043107
- [84] Nagamine G, Jeong B G, Ferreira T A C, Chang J H, Park K, Lee D C, Bae W K and Padilha L A 2020 Efficient Optical Gain in Spherical Quantum Wells Enabled by Engineering Biexciton Interactions *ACS Photonics* **7** 2252–64
- [85] Kholmicheva N, Budkina D S, Cassidy J, Porotnikov D, Harankahage D, Boddy A, Galindo M, Khon D, Tarnovsky A N and Zamkov M 2019 Sustained Biexciton Populations in Nanoshell Quantum Dots *ACS Photonics* **6** 1041–50
- [86] Wang N, Koh S, Jeong B G, Lee D, Kim W D, Park K, Nam M K, Lee K, Kim Y, Lee B-H, Lee K, Bae W K and Lee D C 2017 Highly luminescent silica-coated CdS/CdSe/CdS nanoparticles with strong chemical robustness and excellent thermal stability *Nanotechnology* **28** 185603

- [87] Porotnikov D, Diroll B T, Harankahage D, Obloy L, Yang M, Cassidy J, Ellison C, Miller E, Rogers S, Tarnovsky A N, Schaller R D and Zamkov M 2020 Low-threshold laser medium utilizing semiconductor nanoshell quantum dots *Nanoscale* **12** 17426–36
- [88] Pedetti S, Nadal B, Lhuillier E, Mahler B, Bouet C, Abécassis B, Xu X and Dubertret B 2013 Optimized Synthesis of CdTe Nanoplatelets and Photoresponse of CdTe Nanoplatelets Films *Chem. Mater.* **25** 2455–62
- [89] Tessier M D, Javaux C, Maksimovic I, Loriette V and Dubertret B 2012 Spectroscopy of Single CdSe Nanoplatelets *ACS Nano* **6** 6751–8
- [90] Ithurria S, Tessier M D, Mahler B, Lobo R P S M, Dubertret B and Efros A I L 2011 Colloidal nanoplatelets with two-dimensional electronic structure *Nat. Mater.* **10** 936–41
- [91] Dede D SYNTHESIS AND CHARACTERIZATION OF COLLOIDAL QUANTUM WELLS: FROM SIMPLE SIZE-TUNED CORE TO COMPLEX MULTI-CROWN STRUCTURES 89
- [92] Tessier M D, Spinicelli P, Dupont D, Patriarche G, Ithurria S and Dubertret B 2014 Efficient Exciton Concentrators Built from Colloidal Core/Crown CdSe/CdS Semiconductor Nanoplatelets *Nano Lett.* **14** 207–13
- [93] Gao Y, Li M, Delikanli S, Zheng H, Liu B, Dang C, Sum T C and Demir H V 2018 Low-threshold lasing from colloidal CdSe/CdSeTe core/alloyed-crown type-II heteronanoplatelets *Nanoscale* **10** 9466–75
- [94] Kelestemur Y, Olutas M, Delikanli S, Guzelurk B, Akgul M Z and Demir H V 2015 Type-II Colloidal Quantum Wells: CdSe/CdTe Core/Crown Heteronanoplatelets *J. Phys. Chem. C* **119** 2177–85
- [95] Altintas Y, Quliyeva U, Gungor K, Erdem O, Kelestemur Y, Mutlugun E, Kovalenko M V and Demir H V 2019 Highly Stable, Near-Unity Efficiency Atomically Flat Semiconductor Nanocrystals of CdSe/ZnS Hetero-Nanoplatelets Enabled by ZnS-Shell Hot-Injection Growth *Small* **15** 1804854
- [96] Rossinelli A A, Rojo H, Mule A S, Aellen M, Cocina A, De Leo E, Schäublin R and Norris D J 2019 Compositional Grading for Efficient and Narrowband Emission in CdSe-Based Core/Shell Nanoplatelets *Chem. Mater.* **31** 9567–78
- [97] Kelestemur Y, Guzelurk B, Erdem O, Olutas M, Gungor K and Demir H V 2016 Platelet-in-Box Colloidal Quantum Wells: CdSe/CdS@CdS Core/Crown@Shell Heteronanoplatelets *Adv. Funct. Mater.* **26** 3570–9
- [98] Shendre S, Delikanli S, Li M, Dede D, Pan Z, Ha S T, Fu Y H, Hernández-Martínez P L, Yu J, Erdem O, Kuznetsov A I, Dang C, Sum T C and Demir H V 2019

- Ultrahigh-efficiency aqueous flat nanocrystals of CdSe/CdS@Cd_{1-x}Zn_xS colloidal core/crown@alloyed-shell quantum wells *Nanoscale* **11** 301–10
- [99] Riedinger A, Ott F D, Mule A, Mazzotti S, Knüsel P N, Kress S J P, Prins F, Erwin S C and Norris D J 2017 An intrinsic growth instability in isotropic materials leads to quasi-two-dimensional nanoplatelets *Nat. Mater.* **16** 743–8
- [100] Chen Y, Chen D, Li Z and Peng X 2017 Symmetry-Breaking for Formation of Rectangular CdSe Two-Dimensional Nanocrystals in Zinc-Blende Structure *J. Am. Chem. Soc.* **139** 10009–19
- [101] Park J, Joo J, Kwon S G, Jang Y and Hyeon T 2007 Synthesis of Monodisperse Spherical Nanocrystals *Angew. Chem. Int. Ed.* **46** 4630–60
- [102] Polte J 2015 Fundamental growth principles of colloidal metal nanoparticles – a new perspective *CrystEngComm* **17** 6809–30
- [103] LaMer V K and Dinegar R H 1950 Theory, Production and Mechanism of Formation of Monodispersed Hydrosols *J. Am. Chem. Soc.* **72** 4847–54
- [104] Girma W M, Fahmi M Z, Permadi A, Abate M A and Chang J-Y 2017 Synthetic strategies and biomedical applications of I–III–VI ternary quantum dots *J. Mater. Chem. B* **5** 6193–216
- [105] Murray C B, Kagan C R and Bawendi M G 2000 Synthesis and Characterization of Monodisperse Nanocrystals and Close-Packed Nanocrystal Assemblies *Annu. Rev. Mater. Sci.* **30** 545–610
- [106] Park J, An K, Hwang Y, Park J-G, Noh H-J, Kim J-Y, Park J-H, Hwang N-M and Hyeon T 2004 Ultra-large-scale syntheses of monodisperse nanocrystals *Nat. Mater.* **3** 891–5
- [107] Yang Y A, Wu H, Williams K R and Cao Y C 2005 Synthesis of CdSe and CdTe Nanocrystals without Precursor Injection *Angew. Chem. Int. Ed.* **44** 6712–5
- [108] Hines M A and Guyot-Sionnest P 1996 Synthesis and Characterization of Strongly Luminescing ZnS-Capped CdSe Nanocrystals *J. Phys. Chem.* **100** 468–71
- [109] Li J J, Wang Y A, Guo W, Keay J C, Mishima T D, Johnson M B and Peng X 2003 Large-Scale Synthesis of Nearly Monodisperse CdSe/CdS Core/Shell Nanocrystals Using Air-Stable Reagents via Successive Ion Layer Adsorption and Reaction *J. Am. Chem. Soc.* **125** 12567–75
- [110] Reiss P, Bleuse J and Pron A 2002 Highly Luminescent CdSe/ZnSe Core/Shell Nanocrystals of Low Size Dispersion *Nano Lett.* **2** 781–4

- [111] Yu W W, Qu L, Guo W and Peng X 2003 Experimental Determination of the Extinction Coefficient of CdTe, CdSe, and CdS Nanocrystals *Chem. Mater.* **15** 2854–60
- [112] Norris D J, Sacra A, Murray C B and Bawendi M G 1994 Measurement of the size dependent hole spectrum in CdSe quantum dots *Phys. Rev. Lett.* **72** 2612–5
- [113] Rogach A L 2008 *Semiconductor nanocrystal quantum dots: synthesis, assembly, spectroscopy, and applications* (Wien ; New York: Springer)
- [114] Tam A K, Boyraz O, Unangst J, Nazareta P, Schreuder M and Nilsson M 2018 Quantum-dot doped polymeric scintillation material for radiation detection *Radiat. Meas.* **111** 27–34
- [115] Taghipour N, Delikanli S, Shendre S, Sak M, Li M, Isik F, Tanriover I, Guzelurk B, Sum T C and Demir H V 2020 Sub-single exciton optical gain threshold in colloidal semiconductor quantum wells with gradient alloy shelling *Nat. Commun.* **11** 3305
- [116] Rurack K and Spieles M 2011 Fluorescence Quantum Yields of a Series of Red and Near-Infrared Dyes Emitting at 600–1000 nm *Anal. Chem.* **83** 1232–42
- [117] Yvon H J 2012 A guide to recording fluorescence quantum yields *HORIBA Jobin Yvon Inc Stanmore Middx. UK*
- [118] Laverdant J, Marcillac W D de, Barthou C, Chinh V D, Schwob C, Coolen L, Benalloul P, Nga P T and Maître A 2011 Experimental Determination of the Fluorescence Quantum Yield of Semiconductor Nanocrystals *Materials* **4** 1182–93
- [119] Würth C, Grabolle M, Pauli J, Spieles M and Resch-Genger U 2013 Relative and absolute determination of fluorescence quantum yields of transparent samples *Nat. Protoc.* **8** 1535–50
- [120] Leatherdale C A, Woo W-K, Mikulec F V and Bawendi M G 2002 On the Absorption Cross Section of CdSe Nanocrystal Quantum Dots *J. Phys. Chem. B* **106** 7619–22
- [121] Karel Čapek R, Moreels I, Lambert K, De Muynck D, Zhao Q, Van Tomme A, Vanhaecke F and Hens Z 2010 Optical Properties of Zincblende Cadmium Selenide Quantum Dots *J. Phys. Chem. C* **114** 6371–6
- [122] Maes J, Castro N, De Nolf K, Walravens W, Abécassis B and Hens Z 2018 Size and Concentration Determination of Colloidal Nanocrystals by Small-Angle X-ray Scattering *Chem. Mater.* **30** 3952–62
- [123] Li J, Chen J, Shen Y and Peng X 2018 Extinction coefficient per CdE (E = Se or S) unit for zinc-blende CdE nanocrystals *Nano Res.* **11** 3991–4004

- [124] Anon Continuous Transition from 3D to 1D Confinement Observed during the Formation of CdSe Nanoplatelets | Journal of the American Chemical Society
- [125] Schlosser A, Graf R T and Bigall N C 2020 CdS crown growth on CdSe nanoplatelets: core shape matters *Nanoscale Adv.* **2** 4604–14
- [126] Leemans J, Singh S, Li C, Ten Brinck S, Bals S, Infante I, Moreels I and Hens Z 2020 Near-Edge Ligand Stripping and Robust Radiative Exciton Recombination in CdSe/CdS Core/Crown Nanoplatelets *J. Phys. Chem. Lett.* **11** 3339–44
- [127] Kelestemur Y COLLOIDAL HETEROSTRUCTURES OF SEMICONDUCTOR QUANTUM WELLS: SYNTHESIS, CHARACTERIZATION AND APPLICATIONS 206
- [128] Ithurria S and Talapin D V 2012 Colloidal Atomic Layer Deposition (c-ALD) using Self-Limiting Reactions at Nanocrystal Surface Coupled to Phase Transfer between Polar and Nonpolar Media *J. Am. Chem. Soc.* **134** 18585–90
- [129] Rossinelli A A, Riedinger A, Marqués-Gallego P, Knüsel P N, Antolinez F V and Norris D J 2017 High-temperature growth of thick-shell CdSe/CdS core/shell nanoplatelets *Chem. Commun.* **53** 9938–41
- [130] Altintas Y, Gungor K, Gao Y, Sak M, Quliyeva U, Bappi G, Mutlugun E, Sargent E H and Demir H V 2019 Giant Alloyed Hot Injection Shells Enable Ultralow Optical Gain Threshold in Colloidal Quantum Wells *ACS Nano* **13** 10662–70
- [131] Cui J, Beyler A P, Coropceanu I, Cleary L, Avila T R, Chen Y, Cordero J M, Heathcote S L, Harris D K, Chen O, Cao J and Bawendi M G 2016 Evolution of the Single-Nanocrystal Photoluminescence Linewidth with Size and Shell: Implications for Exciton-Phonon Coupling and the Optimization of Spectral Linewidths *Nano Lett.* **16** 289–96
- [132] Castelli A, Dhanabalan B, Polovitsyn A, Caligiuri V, Di Stasio F, Scarpellini A, Brescia R, Palei M, Martín-García B, Prato M, Manna L, Moreels I, Krahne R and Arciniegas M P 2020 Core/Shell CdSe/CdS Bone-Shaped Nanocrystals with a Thick and Anisotropic Shell as Optical Emitters *Adv. Opt. Mater.* **8** 1901463
- [133] Klimov V I, Ivanov S A, Nanda J, Achermann M, Bezel I, McGuire J A and Piryatinski A 2007 Single-exciton optical gain in semiconductor nanocrystals *Nature* **447** 441–6
- [134] Shirasaki Y, Supran G J, Bawendi M G and Bulović V 2013 Emergence of colloidal quantum-dot light-emitting technologies *Nat. Photonics* **7** 13–23
- [135] Lim J, Jeong B G, Park M, Kim J K, Pietryga J M, Park Y-S, Klimov V I, Lee C, Lee D C and Bae W K 2014 Influence of Shell Thickness on the Performance of Light-

- Emitting Devices Based on CdSe/Zn_{1-x}Cd_xS Core/Shell Heterostructured Quantum Dots *Adv. Mater.* **26** 8034–40
- [136] Dujardin C, Amans D, Belsky A, Chaput F, Ledoux G and Pillonnet A 2010 Luminescence and Scintillation Properties at the Nanoscale *IEEE Trans. Nucl. Sci.* **57** 1348–54
- [137] Klimov V I 2014 Multicarrier Interactions in Semiconductor Nanocrystals in Relation to the Phenomena of Auger Recombination and Carrier Multiplication *Annu. Rev. Condens. Matter Phys.* **5** 285–316
- [138] Rodnyi P A 1997 *Physical processes in inorganic scintillators* vol 14 (CRC press)
- [139] Vasil'ev A N 2017 Microtheory of Scintillation in Crystalline Materials *Engineering of Scintillation Materials and Radiation Technologies* Springer Proceedings in Physics vol 200, ed M Korzhik and A Gektin (Cham: Springer International Publishing) pp 3–34
- [140] Nasilowski M 2015 *Synthesis and optical spectroscopy of thick-shell semiconductor nanoparticles: applications to biological imaging* PhD Thesis (Paris 6)
- [141] Rabouw F T, Kamp M, van Dijk-Moes R J A, Gamelin D R, Koenderink A F, Meijerink A and Vanmaekelbergh D 2015 Delayed Exciton Emission and Its Relation to Blinking in CdSe Quantum Dots *Nano Lett.* **15** 7718–25
- [142] Gaur G, Koktysh D, Fleetwood D M, Reed R A, Weller R A and Weiss S M 2013 Effects of x-ray and gamma-ray irradiation on the optical properties of quantum dots immobilized in porous silicon SPIE Defense, Security, and Sensing ed T George, M S Islam and A K Dutta (Baltimore, Maryland, USA) p 87252D
- [143] Bae W K, Padilha L A, Park Y-S, McDaniel H, Robel I, Pietryga J M and Klimov V I 2013 Controlled Alloying of the Core–Shell Interface in CdSe/CdS Quantum Dots for Suppression of Auger Recombination *ACS Nano* **7** 3411–9
- [144] García-Santamaría F, Chen Y, Vela J, Schaller R D, Hollingsworth J A and Klimov V I 2009 Suppressed Auger Recombination in “Giant” Nanocrystals Boosts Optical Gain Performance *Nano Lett.* **9** 3482–8
- [145] Vanmaekelbergh D, van Vugt L K, Bakker H E, Rabouw F T, de Nijs B, van Dijk-Moes R J A, van Huis M A, Baesjou P J and van Blaaderen A 2015 Shape-Dependent Multiexciton Emission and Whispering Gallery Modes in Supraparticles of CdSe/Multishell Quantum Dots *ACS Nano* **9** 3942–50
- [146] Cihan A F, Hernandez Martinez P L, Kelestemur Y, Mutlugun E and Demir H V 2013 Observation of Biexcitons in Nanocrystal Solids in the Presence of Photocharging *ACS Nano* **7** 4799–809

- [147] Pietryga J M, Padilha L A, Bae W K, Klimov V I and Schaller R D 2013 Probing the gamma-scintillation process in semiconductor nanomaterials using ultrafast transient cathodoluminescence SPIE Defense, Security, and Sensing ed A W Fountain (Baltimore, Maryland, USA) p 87101G
- [148] Guzelurk B, Erdem O, Olutas M, Kelestemur Y and Demir H V 2014 Stacking in Colloidal Nanoplatelets: Tuning Excitonic Properties *ACS Nano* **8** 12524–33
- [149] Crooker S A, Hollingsworth J A, Tretiak S and Klimov V I 2002 Spectrally Resolved Dynamics of Energy Transfer in Quantum-Dot Assemblies: Towards Engineered Energy Flows in Artificial Materials *Phys. Rev. Lett.* **89** 186802
- [150] Rowland C E, Fedin I, Zhang H, Gray S K, Govorov A O, Talapin D V and Schaller R D 2015 Picosecond energy transfer and multiexciton transfer outpaces Auger recombination in binary CdSe nanoplatelet solids *Nat. Mater.* **14** 484–9
- [151] Grim J Q, Christodoulou S, Di Stasio F, Krahn R, Cingolani R, Manna L and Moreels I 2014 Continuous-wave biexciton lasing at room temperature using solution-processed quantum wells *Nat. Nanotechnol.* **9** 891–5
- [152] Birkedal D, Singh J, Lyssenko V G, Erland J and Hvam J M 1996 Binding of Quasi-Two-Dimensional Biexcitons *Phys. Rev. Lett.* **76** 672–5
- [153] Zelewski S J, Nawrot K C, Zak A, Gladysiewicz M, Nyk M and Kudrawiec R 2019 Exciton Binding Energy of Two-Dimensional Highly Luminescent Colloidal Nanostructures Determined from Combined Optical and Photoacoustic Spectroscopies *J. Phys. Chem. Lett.* **10** 3459–64
- [154] Olutas M, Guzelurk B, Kelestemur Y, Yeltik A, Delikanli S and Demir H V 2015 Lateral Size-Dependent Spontaneous and Stimulated Emission Properties in Colloidal CdSe Nanoplatelets *ACS Nano* **9** 5041–50
- [155] Altintas Y, Quliyeva U, Gungor K, Erdem O, Kelestemur Y, Mutlugun E, Kovalenko M V and Demir H V 2019 Highly Stable, Near-Unity Efficiency Atomically Flat Semiconductor Nanocrystals of CdSe/ZnS Hetero-Nanoplatelets Enabled by ZnS-Shell Hot-Injection Growth *Small* **15** 1804854
- [156] Tessier M D, Mahler B, Nadal B, Heuclin H, Pedetti S and Dubertret B 2013 Spectroscopy of Colloidal Semiconductor Core/Shell Nanoplatelets with High Quantum Yield *Nano Lett.* **13** 3321–8
- [157] Kunneman L T, Schins J M, Pedetti S, Heuclin H, Grozema F C, Houtepen A J, Dubertret B and Siebbeles L D A 2014 Nature and Decay Pathways of Photoexcited States in CdSe and CdSe/CdS Nanoplatelets *Nano Lett.* **14** 7039–45

-
- [158] Bae W K, Padilha L A, Park Y-S, McDaniel H, Robel I, Pietryga J M and Klimov V I 2013 Controlled Alloying of the Core–Shell Interface in CdSe/CdS Quantum Dots for Suppression of Auger Recombination *ACS Nano* **7** 3411–9
- [159] Kelestemur Y, Shynkarenko Y, Anni M, Yakunin S, De Giorgi M L and Kovalenko M V 2019 Colloidal CdSe Quantum Wells with Graded Shell Composition for Low-Threshold Amplified Spontaneous Emission and Highly Efficient Electroluminescence *ACS Nano* **13** 13899–909
- [160] Klimov V I 2000 Optical Nonlinearities and Ultrafast Carrier Dynamics in Semiconductor Nanocrystals *J. Phys. Chem. B* **104** 6112–23
- [161] Scott R, Achtstein A W, Prudnikau A V, Antanovich A, Siebbeles L D A, Artemyev M and Woggon U 2016 Time-Resolved Stark Spectroscopy in CdSe Nanoplatelets: Exciton Binding Energy, Polarizability, and Field-Dependent Radiative Rates *Nano Lett.* **16** 6576–83
- [162] Wood V, Panzer M J, Caruge J-M, Halpert J E, Bawendi M G and Bulović V 2010 Air-Stable Operation of Transparent, Colloidal Quantum Dot Based LEDs with a Unipolar Device Architecture *Nano Lett.* **10** 24–9